Two b or not two b-jets

Measurements of inclusive and dijet b-jet differential cross-sections with the ATLAS detector

Stephen Paul Bieniek
Supervisor: Prof. Nikos Konstantinidis

University College London

Submitted to University College London in fulfilment of the requirements for the award of the degree of Doctor of Philosophy, 21st June 2013.

I, Stephen Bieniek confirm that the work presented in this thesis is my own. Where information has been derived from other sources, I confirm that this has been indicated in the thesis.

Acknowledgements

There are many people who I would like to thank for helping me get through my PhD and I don't have the space to list all of them. I would first like to thank my supervisor, Nikos Konstantinidis [1], for providing me the support, motivation and direction for this project. I would like to thank Eric Jansen [2] for being there to answer my questions, show me the ropes while I was learning everything and always being there for bouncing ideas off. I would like to thank Lynn Marx [3] who provided the competition I needed to motivate me to produce my best during my time at CERN and Sarah Baker [4] for keeping me company when working late. I'd like to thank my fellow PhD students Erin Walters [5] and Bobby Xinyue [6] who allowed me to keep things in perspective when the work was hard. I would also like to thank Daniel Lattimer [7] for helping me ease back into London life after my time away.

As a last note, I would like to dedicate this thesis to Francis Corry. He passed away days after I got accepted on to the program and has always been an inspiration to me.

Abstract

This thesis discusses the measurement of the inclusive b-jet cross-section using the 2010 ATLAS dataset and the measurement of di-b-jet cross-sections using the 2011 dataset. The inclusive b-jet analysis measured the p_{T} spectrum of b-jets in the range $20 < p_{\mathrm{T}} < 400\,\mathrm{GeV}$ in four rapidity ranges, $|y| < 0.3$, $0.3 < |y| < 0.8$, $0.8 < |y| < 1.2$ and $1.2 < |y| < 2.1$. Good agreement was observed between data and the next-to-leading order (NLO) theory predictions generated by the POWHEG and MC@NLO Monte Carlo generators. However, when the cross-section measurement was split into the $|y|$ regions, MC@NLO showed some shape differences with respect to data. The di-b-jet analysis using the 2011 ATLAS dataset measured the di-b-jet cross-section with respect to six different variables. This analysis investigates regions of phase space that are sensitive to different $b\bar{b}$ production mechanisms. It was found that Monte Carlo simulation predicts back-to-back b-jet topologies well. Situations where the b-jets are closer together are more challenging to model and both MC@NLO and POWHEG overpredict the rate of such events.

Preface

This thesis covers the measurement of the inclusive and dijet b-jet cross-sections measured in the 2010 data-taking period and the di-b-jet cross-sections measured in the 2011 data-taking period using the ATLAS detector. The 2010 analysis of the inclusive b-jet cross section was done by a team of five and is published in Ref. [8]. I investigated the jet energy scale and jet energy resolution systematic uncertainties; the unfolding of the inclusive b-jet cross-sections; and the comparison to theoretical predictions for all distributions. The 2011 analysis was performed by a team of three and is currently not published. I investigated the trigger efficiencies and decided the trigger strategy; the unfolding; the comparison to theoretical predictions; and was involved in planning and implementing all stages of the analysis.

In addition to the analysis work, a large portion of my time was spent doing 'service' work. To gain authorship accreditation on the ATLAS experiment, each member must complete the equivalent of 6 month full time work on tasks that help the experiment as a whole part are not connected to a physics analysis. To gain accreditation I worked on the ATLAS event display software, ATLANTIS. My role was primarily software development and presenting software tutorials. Later, I led a team to implement the POWHEG-BOX programme into the ATLAS common software framework. My service work is not discussed in this thesis.

Contents

List of Figures

List of Tables

Chapter 1.

Introduction

A b-jet is a cluster of particles that originate from a b-quark; b-jets are special because they behave in characteristic ways which allow them to be separated from other flavours of jets. The mass of the b-quark makes it an interesting problem from a theoretical perspective; the greater mass means many theoretical models have exotic particles that preferentially decay to these jets. Standard model particles, such as the top-quark or Higgs, also decay preferentially to b-quarks and thus can be found through making use of the b-jets identifiable signature.

Cross-sections for b-jet production in $p\bar{p}$ collisions have been measured at the Sp$\bar{\text{p}}$S [9, 10] and the Tevatron [11–14] colliders. The Tevatron measurements, at the time, showed disagreement with the Quantum Chromodynamics (QCD) predictions. This led to substantial improvements in the experimental methods and theoretical calculations. It is therefore of great interest to test the theoretical predictions at the higher centre-of-mass energy provided by the Large Hadron Collider (LHC). Measurements of b-jets in the forward region have been reported by LHCb [15] and in the central region by CMS [16, 17]. This thesis describes the b-jet cross-section measurements made with data collected by the ATLAS detector during 2010 [8] and 2011.

The theoretical underpinning for such measurements is covered in chapter 2 and a description of the ATLAS detector is given in chapter 3. Chapter 4 presents techniques, tools and concepts common to the 2010 and 2011 analyses, with the two measurements described in chapters 5 and 6 respectively.

Chapter 2.

Theory Section

2.1. The Standard Model

Modern particle physics is based upon the study and measurement of the Standard Model (SM) or searches for deviation from it. The SM describes the interactions and behaviour of the fundamental particles and forces in nature (except gravity) and was formalised, as it is known today, in the mid-1970s. The subsequent discovery of particles such as the weak bosons in the early 1980s and more recently the Higgs boson confirm the model's predictive power. In high-precision searches, such as those done at the LHC, little deviation from the SM is observed. However, it is known that the SM cannot be the description of all particle interactions. The existence of neutrino oscillation, and thus neutrino mass, as well the matter/anti-matter asymmetry in the universe show that there are still fundamental questions to be answered.

In the Standard Model, all of the fundamental interactions derive from a single principle, the requirement of local gauge invariance [18]. The particles that make up the SM can be split into two categories, the spin-$\frac{1}{2}$ fermions, known as quarks and leptons, and the integer spin bosons, known as the bosons, which act as the force carriers in the model. A primary distinction between quarks and leptons, is that quarks are colour-charged and so interact via the strong force. Each fermion in the standard model has an associated partner anti-particle. An anti-particle shares all the relevant quantities with its partner, but has an opposite charge.

The Standard Model is expressed in terms of quantum field theory. However, to aid calculations and visualise physical processes, Feynman diagrams can be used. If the appropriate rules are followed, a formula can be derived from a diagram that will predict the rates and characteristics of the process. Diagrams with the least number of vertices/interaction points represent the lowest order of the calculation in perturbation theory and are known as leading order (LO). This can be seen in Fig. 2.1, where (a) represents the the annihilation of the quark pair of flavour q, which then create the quark pair of flavour Q. Diagram (b) represents this same

process, but with an additional emission of a gluon from one of the incoming quarks. The extra interaction vertex in this diagram implies this is higher order effect in perturbation theory. As (b) is the leading order diagram with one additional vertex, it is known as a next-to-leading order (NLO) diagram.

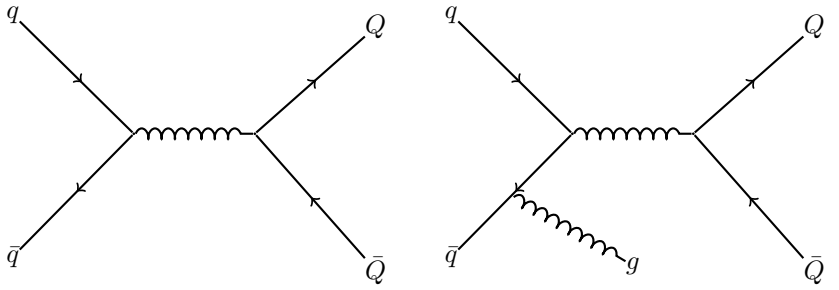

(a) Leading Order **(b)** Next-to-leading order diagram

Figure 2.1.: Examples of a leading order and next-to-leading order Feynman diagrams.

2.2. Quantum Chromodynamics

Quantum chromodynamics is the model that describes the strong nuclear force; the force responsible for holding the nucleus of an atom together. Mediating this force is a gauge boson known as the 'gluon'. A gluon is a spin-1, massless particle that couples to particles with colour charge. Colour charge exists in three colour states: red, blue and green. Quarks, the subatomic particles that make up hadrons such as protons and neutrons, have a single colour charge, such as blue or anti-blue, while gluons have pairs of colour charges. Collectively, quarks and gluons are known as partons. The additional degree of freedom means there are three variants of each quark flavour and eight gluons. In nature, individual quarks or coloured particles are never observed. Coloured particles are always observed in bound colourless states with other coloured particles. The reasons for this are explained later.

The Lagrangian of QCD is split into three parts, as expressed in equation 2.1:

$$\mathcal{L}_{\text{QCD}} = \mathcal{L}_{\text{classical}} + \mathcal{L}_{\text{gauge-fixing}} + \mathcal{L}_{\text{ghost}}, \tag{2.1}$$

where the expression for the classical Lagrangian density is given by:

$$\mathcal{L}_{\text{classical}} = -\frac{1}{4} F^A_{\alpha\beta} F_A^{\alpha\beta} + \sum_{Flavours} \bar{q}_a (i\gamma_\mu D^\mu - m)_{ab} q_b. \tag{2.2}$$

The first term in equation 2.2 describes the gluon field and the second term the interaction with quarks. The field strength tensor, $F^A_{\alpha\beta}$ is derived from the gluon

field $\mathcal{A}^A_\alpha$,

$$F^A_{\alpha\beta} = \left[\partial_\alpha \mathcal{A}^A_\beta - \partial_\beta \mathcal{A}^A_\alpha - g f^{ABC} \mathcal{A}^B_\alpha \mathcal{A}^C_\beta\right]. \tag{2.3}$$

The third term in equation 2.3 differentiates QCD from Quantum Electrodynamics (QED) and causes the gluon self interaction. However, the self interaction terms means that $\mathcal{L}_{\text{classical}}$ is not gauge invariant. By introducing $\mathcal{L}_{\text{gauge-fixing}}$, gauge invariance can be restored and QCD becomes calculable in perturbation theory. The $\mathcal{L}_{\text{ghost}}$ term is introduced to cancel unphysical terms in some choices of $\mathcal{L}_{\text{gauge-fixing}}$. The gluon propagator term depends on the choice of $\mathcal{L}_{\text{gauge-fixing}}$. The gluon self interaction isn't the only distinctive characteristic of QCD, the behaviour of the coupling strength as a function of energy of the interaction is of equal interest.

2.2.1. Running of the Coupling Constants

Consider some physical observable, R, and a single large energy scale, Q. It can be assumed that Q is large enough to be the only relevant scale. A naïve scaling would suggest that R should have constant value independent of Q. When calculating R in a perturbation series, at some point the theory will need to be renormalised due to ultraviolet divergences. However, R being independent of Q would mean our theory could not account for the divergences and is not a renormalisable quantum field theory. These ultraviolet divergences introduce another energy scale, μ. In general, R depends on the ratio of energy at which R takes place and the ultraviolet cut-off scale, Q^2/μ^2. As QCD, a renormalisable theory, requires this ultra-violet cut-off scale, it follows that α_S has a similar scale dependence. However, μ is not present in the QCD Lagrangian. Thus, even though a choice of μ is required to define the theory at a quantum level, μ can be considered an arbitrary parameter. Because of this, our physical observable should not depend on the choice made for μ. It can only depend on the ratio Q^2/μ^2 and the renormalised coupling α_S. The independence of R to μ can be expressed in equation 2.4:

$$\mu^2 \frac{d}{d\mu^2} R(Q^2/\mu^2, \alpha_S) \equiv \left[\mu^2 \frac{\partial}{\partial \mu^2} + \mu^2 \frac{\partial \alpha_S}{\partial \mu^2} \frac{\partial}{\partial \alpha_S}\right] R = 0. \tag{2.4}$$

By defining two new parameters,

$$t = ln\left(\frac{Q^2}{\mu^2}\right), \quad \beta(\alpha_S) = \mu^2 \frac{\partial \alpha_S}{\partial \mu^2}, \tag{2.5}$$

equation 2.4 can be rewritten as:

$$\left[-\frac{\partial}{\partial t} + \beta(\alpha_S) \frac{\partial}{\partial \alpha_S}\right] R(e^t, \alpha_S) = 0. \tag{2.6}$$

Equation 2.6 can be solved by implicitly defining a new function, α_S (Q^2), known as 'the running coupling'. Here, the value of α_S is seen to be dependent on the scale, Q, of the process. With a bit more algebra, which is explained fully in [19], the leading order approximation of α_S is found to be:

$$\alpha_S(Q^2) = \frac{\alpha_S(\mu^2)}{1 + \alpha_S(\mu^2) b_0 t}, \tag{2.7}$$

where b_0 is the first term in $\beta(\alpha_S)$ when expanded in a perturbative series. As t is proportional to the logarithm of Q, $\alpha_S(Q^2)$ decreases as Q increases. This means for very large values of Q the strong coupling goes to 0. To put it in more practical terms, for large values of Q, QCD is perturbative and the leading order approximation will give a reasonable representation of nature. The change in the strength of α_S is the starting point for a concept known as 'asymptotic freedom'.

2.2.2. Asymptotic Freedom

Asymptotic freedom means that the strong coupling gets weaker at high energies (small distances). This is opposed to QED, where the coupling strength increases with energy. The explanation for the smaller charge of the electron at large distances is quite intuitive, the screening by vacuum polarisation reduces the observed charge. For QCD it is less so. Two analogies with other physics phenomena can be made, the description of the effect in terms of dielectrics or paramagnetics. The simpler to explain is dielectrics, where the emission of virtual gluons from a static charge causes their colour charge to leak out. Other colour charges outside this leakage see the full strength of the static charge. As one moves closer, within the bounds of the leakage, the overall charge appears weaker. On the other hand, the notion that the strong force increases as energy decreases, or equivalently as distance increases lead to the idea of confinement. Confinement is the phenomenon that describes why coloured particles are forced to form colourless bound states. However, this close range force, by definition, is outside the bounds of perturbative Quantum Chromodynamics (pQCD). A robust proof that QCD produces this effect still isn't available, despite the strong indications for it.

2.2.3. Heavy Quark Production

The lowest order production mechanisms of a pair of b-quarks can be seen in Fig. 2.2. Diagram (a), known as flavour creation (FCR), is the typical Drell-Yan-like production which is associated with most quark-pair production. Diagram (b) shows the t-channel flavour creation process. Diagrams (c) and (d) show a higher order correction to b-quark production and play an important role. This is especially true in the event kinematics of the di-b-quark system. Gluons decaying to a pair

of b-quarks before or after the hard scatter make up a considerable fraction of the total $b\bar{b}$ cross-section. When the $b\bar{b}$-pair is created in the initial state it is known as flavour excitation (FEX) and when it happens in the final state it is known as gluon splitting (GSP). Such diagrams have specific kinematics that at LO cannot be recreated from flavour creation production. As the energy of the decaying gluon that produces the pair of b-quarks in FEX or GSP production is often much less then the hard scatter, the b-quarks tend to be end up close together following the original path of the gluon. FCR production tends to produce events where the b-jets have are back-to-back and are the hardest jets in the event. GSP tend to produce a pair of close-by jets recoiling off a hard jet going the opposite direction. As one b-jet comes from the hard interaction, FEX production events tend to produce b-jets with asymmetric momentum which often end up close together. It is important to note that differentiating production mechanisms, as described here, is not theoretically well defined. These distinctions are useful tools to understand the production in computer simulations done at LO or NLO accuracy; however, when a full perturbative expansion is considered, the distinctions cease to exist.

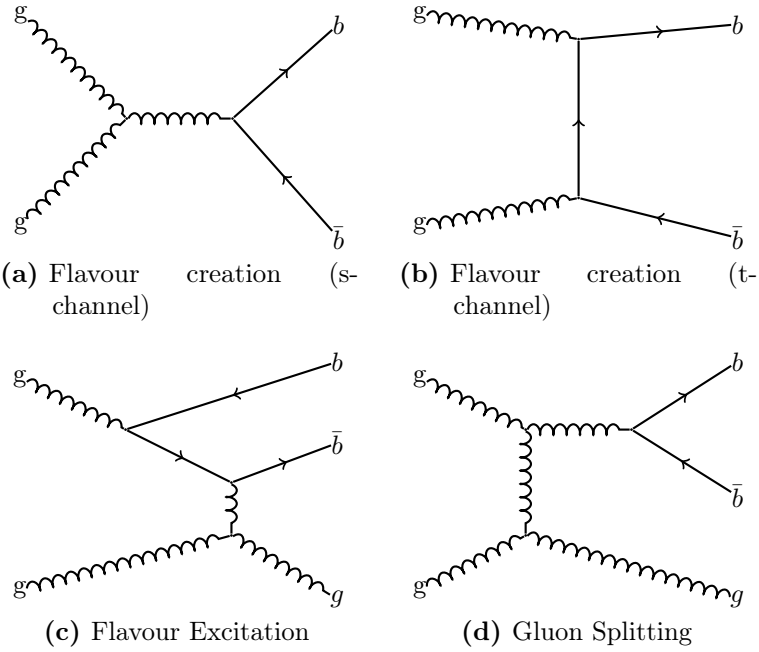

(a) Flavour creation (s-channel)

(b) Flavour creation (t-channel)

(c) Flavour Excitation

(d) Gluon Splitting

Figure 2.2.: Lowest order $b\bar{b}$ Production Mechanisms.

Compared to lighter hadrons, those formed from b-quarks have two characteristics that allow them to be differentiated from other flavour of hadrons. Ground state b-hadrons can only decay via the weak interaction to lighter hadrons, as the $b \to c$ decay is suppressed this means the b-hadron's life time is even longer. When considering the high energies that the b-hadron are created at, this life time translates to traveling a few mm in the detector before decaying. By looking for this secondary vertex,

b-hadron decay can be identified. The hadron may also undergo a semi-leptonic decay, where the produced W boson decays to a lepton and neutrino. Due to the high mass of a b-quark, leptons produced from a b-hadron semileptonic decay will be produced with more energy. Thus, when compared with other flavours of hadron, they have a larger transverse momentum with respect to the hadron flight path.

2.3. QCD for the LHC

All processes happening at the LHC will involve QCD in one form or another. Thus, the experimental and theoretical understanding of this area is very important. QCD measurements have two primary roles at the LHC:

- precision testing of QCD itself, and
- to understand QCD processes as the backgrounds to new physics.

2.3.1. Factorisation Theorem

Using the factorization theorem [19–21] the calculation for a given process can be split into the perturbative hard process and the non-perturbative bound-state effects of partons within the proton, as expressed in equation 2.8:

$$\begin{aligned}\sigma(p_a, p_b; Q, \{...\}) = &\sum_{a,b} \int dx_a dx_b f_{a/A}(x_a, \mu_F^2) f_{b/B}(x_b, \mu_F^2) \\ &\cdot \hat{\sigma}_{ab}(x_a p_a, x_b p_b; Q, ...; \mu_R, \mu_F; \alpha_S(\mu_R)) + \mathcal{O}((\Lambda_{\mathrm{QCD}}/Q)^p).\end{aligned} \tag{2.8}$$

The $\{...\}$ term stands for the kinematic variable of interest, p_a and p_b are the 4-momenta of incoming partons a and b. $f_{a/A}(f_{b/B})$ is the parton distribution of parton $a(b)$ within hadron $A(B)$, $x_a(x_b)$ is the fraction of momentum parton $a(b)$ has with respect to hadron $A(B)$. The parton distribution functions (PDFs) are discussed in depth in Sect. 2.3.2.

Q is the energy scale of the interaction. Related to this value are the renormalisation scale, μ_R, and the factorisation scale, μ_F. The renormalisation scale is the scale at which α_S is evaluated at and the factorisation scale is the energy scale separating the high-energy hard process from the low-energy PDFs. The cross-section $\hat{\sigma}_{ab}$ is the perturbative cross-section for the given process. If $\hat{\sigma}_{ab}$ could be evaluated at all orders, the dependence on μ_R and μ_F would drop out.

The $\mathcal{O}((\Lambda_{\mathrm{QCD}}/Q)^p)$ term represents non-perturbative effects such as fragmentation and hadronisation, where Λ_{QCD} is the constant that relates the value of α_S and Q. In

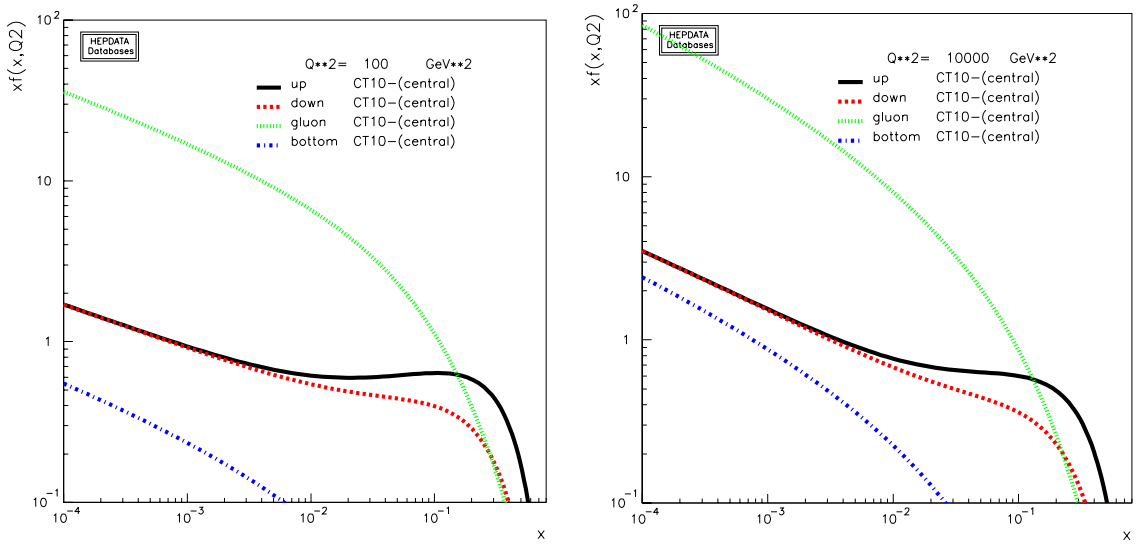

(a) $Q^2 = 100\,\mathrm{GeV}^2$ **(b)** $Q^2 = 10\,\mathrm{TeV}^2$

Figure 2.3.: Parton distribution function for the CT10 fit of the gluon and up-, down- and bottom-quark [23].

the leading order approximation, equation 2.7 can be be expressed as equation 2.9,

$$\alpha_S(Q) = \frac{1}{b_0 \ln(Q^2/\Lambda^2_{\mathrm{QCD}})}, \tag{2.9}$$

where the relation between α_S and Q can be seen explicitly.

2.3.2. Parton Distribution Functions

A fundamental issue when predicting collisions at a hadron collider is the make-up of the colliding hadrons. Theoretical predictions are based upon two incoming partons, thus the rate and range of energies at which these partons exist within a proton, of energy Q, is very important. For a proton with energy Q, the PDFs describe the momentum fraction, x, which different partons have of the overall energy. Examples of this can be seen in Fig. 2.3, where these are the PDFs for the CT10 fit [22] at a $Q^2 = 100$ and 10000 GeV^2.

Accurate PDFs are vital; in some cases the uncertainty associated with the PDFs is the largest theoretical uncertainty. For analyses covered by this thesis, PDFs from the MSTW [24], CTEQ [25] and NNPDF [26] PDF fitting groups were used. They were chosen because they make use of all available data in their fits, other groups only make use of selected samples.

Results from experiments at different energies can be related to each other and used in a single global fit by making use of the DGLAP evolution equations [27–30]. The DGLAP equations describe the evolution of PDFs from one value of Q^2 to another, and are given in equations 2.10 and 2.11 [31]:

$$\frac{\partial q_i(x,\mu^2)}{\partial \log \mu^2} = \frac{\alpha_S}{2\pi}\int_x^1 \frac{\mathrm{d}z}{z}\Big\{P_{q_iq_j}(z,\alpha_S)q_j(\frac{x}{z},\mu^2) + P_{q_ig}(z,\alpha_S)g(\frac{x}{z},\mu^2)\Big\}, \tag{2.10}$$

$$\frac{\partial g(x,\mu^2)}{\partial \log \mu^2} = \frac{\alpha_S}{2\pi}\int_x^1 \frac{\mathrm{d}z}{z}\Big\{P_{gq_j}(z,\alpha_S)q_j(\frac{x}{z},\mu^2) + P_{gg}(z,\alpha_S)g(\frac{x}{z},\mu^2)\Big\}, \tag{2.11}$$

where P_{ab} are the splitting functions describing the decay/radiation of quarks and gluons. Equations 2.10 and 2.11 determine the Q^2 dependence. The x dependence needs to be derived from data.

The accuracy to which a parton distribution is determined for a given x and Q^2 'feed-down' to lower values of x at higher values of Q^2. These extrapolated values depend on the accuracy of the original measurement. Deriving this uncertainty error band in terms of one standard deviation of a Gaussian distribution is difficult. The data used in the global fit have complicated correlations between a particular PDF at different x values and between PDF flavours. For example, as the total available energy for the creation of gluons is constrained, the low x gluon values are correlated to the high x values [21]. The determination of α_S and the gluon PDF are also strongly linked. The two can either be determined together by a PDF fit to available data, or α_S can be determined from experiment, e.g. e^-e^+ interactions, and used as an input parameter to a fit for the gluon PDF. The method used differs between the PDF fitting groups. The CTEQ group use the latter approach, taking the world average value for $\alpha_S(M_Z)$, 0.118–0.119. When taking this approach, either the value of $\alpha_S(M_Z)$ or Λ_{QCD} is quoted. Another issue is the uncertainties quoted on the input data and fitting procedures are not simple to understand in a probabilistic sense. Thus, propagating these errors through an analysis in a consistent way presents challenges.

Global fits can also be performed using LO matrix elements, resulting in leading-order PDFs. Such PDFs are preferred when using LO Monte Carlo like Pythia 6 and Herwig 6. There is currently some debate on whether LO or NLO PDFs should be used in leading order Monte Carlo. While the NLO PDFs can contain much of the higher order physics, the inconsistent approach can cause issues. As a compromise, there are now sets of PDFs containing NLO information but fitted using a LO matrix element.

Chapter 3.

The LHC and the ATLAS Detector

3.1. The Large Hadron Collider

The LHC is a proton-proton collider located on the border of France and Switzerland. Housed in a circular tunnel, 27 km in circumference, the collider is buried 50 to 175 m underground. It was designed to collide bunches of about 10^{11} particles 40 million times per second. At the design centre-of-mass energy of 14 TeV, it delivers a luminosity of $10^{34}\,\mathrm{cm}^{-2}\mathrm{s}^{-1}$. For the analyses discussed in this thesis, the collider was run at half the design energy, providing a centre-of-mass energy of 7 TeV. The 2010 run was predominantly a calibration run. However, the low number of simultaneous proton collisions made it very useful for certain areas of physics. A total integrated luminosity of $\sim 50\,\mathrm{pb}^{-1}$ was delivered in 2010. In 2011 the luminosity delivered increased to $\sim 5\,\mathrm{fb}^{-1}$. There are four main experiments which record the LHC collisions. Two special purpose detectors, ALICE [32] and LHCb [33], and two multipurpose detectors, ATLAS [34] and CMS [35].

3.2. The ATLAS Detector

The ATLAS (A Toroidal LHC ApparatuS) detector, shown in Fig. 3.1, is made up of three primary detecting systems: the inner detector, calorimetry and muon system. ATLAS was designed around a set of benchmark physics processes, primarily the decay of the Higgs boson. Thus, the minimum detector criteria were based around the ability to identify the associated physics objects. Key features are good pattern recognition and momentum resolution of charged particles. To achieve this a powerful magnetic field is required. One of the primary physical constraints on the systems was fitting them around these large magnets. There are two sets of magnets: the solenoid which immerses the inner detector in a 2 T magnetic field, and three toroids which provide up to a 1 T magnetic field for the muon system.

The ATLAS detector defines its own co-ordinate system with origin at the nominal beam interaction point. All the detector and physics processes are defined by this geometry. ATLAS uses a right-handed co-ordinate system with the z-axis defined along the beam pipe, the positive x-axis pointing towards the centre of the LHC ring and the positive y-axis defined to be up. The two halves of the detector are labelled side A and side C, with the positive z-axis pointing towards side A. The angular co-ordinate ϕ is defined around the beam axis and θ is defined as the angle from the beam axis. The more commonly used co-ordinates are the rapidity, y, and pseudo-rapidity, η, which are defined in equation 3.1 and 3.2 respectively,

$$\eta = -\ln\left[\tan\left(\frac{\theta}{2}\right)\right], \tag{3.1}$$

$$y = \frac{1}{2}\ln\left(\frac{E + p_z}{E - p_z}\right). \tag{3.2}$$

In the massless limit, y tends to η. These co-ordinates are used because the rate of particle production is approximately flat with η. For physics analyses, the transverse momentum (p_{T}) and ΔR, defined in eq. 3.3, are used. The transverse plane is defined to be in the $x - y$ plane.

$$\Delta R = \sqrt{\Delta\phi^2 + \Delta\eta^2} \tag{3.3}$$

3.2.1. The Inner Detector

The inner detector is designed to give excellent pattern recognition, particle momentum resolution and identification of both primary and secondary vertices. To do this, it is made up of three sections, the pixel detector, silicon microstrip detector (SCT), and transition radiation tracker (TRT). Each technology is designed to record the path taken as a charged particle passes through it. These paths, once reconstructed from there interactions with the detector, are known as tracks. By immersing the inner detector in a magnetic field, the charge and momentum can be calculated from the curvature of the track. The precision tracking detectors, the pixel and SCT, extend out to $|\eta| < 2.5$, while the TRT only covers up to $|\eta| < 2.0$. In the barrel region the precision tracking detectors are made up of concentric cylinders around the beam axis. In the end cap the sensors are located on disks which are perpendicular to the beam axis. This can be seen in Fig. 3.2. The combination of the different tracking systems allow tracks down to 400 MeV to be measured accurately. For a central track with $p_{\mathrm{T}} = 5\,\mathrm{GeV}$, the p_{T} resolution is around 75 MeV [36].

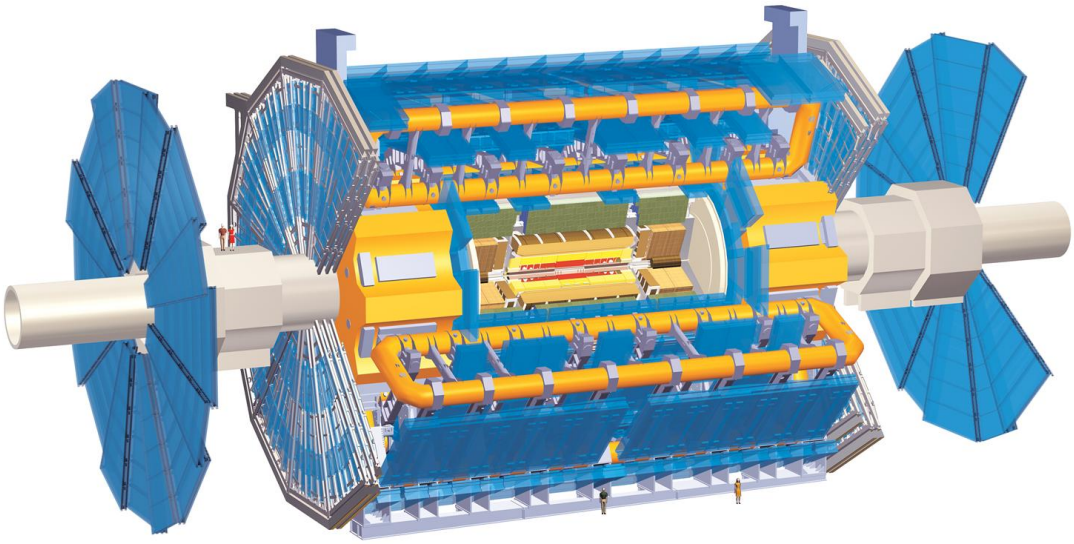

Figure 3.1.: The ATLAS detector, with people shown for scale.

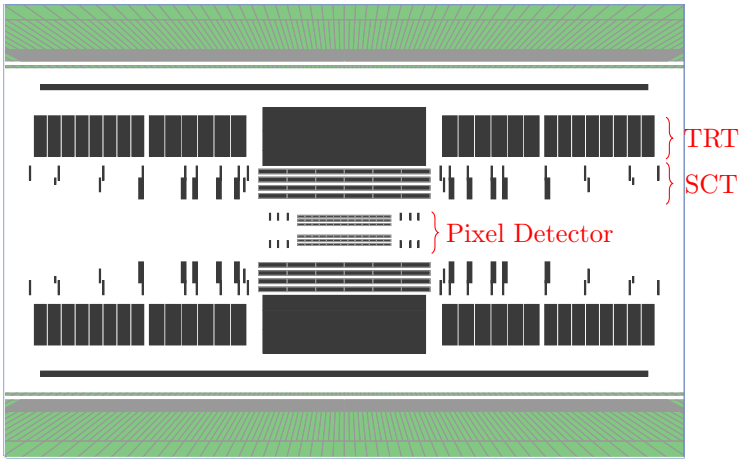

Figure 3.2.: The inner detector as shown in the $\rho - z$ view of the Atlantis event display [2]. Moving radially out from the centre, this image shows: the pixel detector, SCT and TRT in black.

The Pixel Detector

The pixel detector is the closest detector to the beam line. It is a solid-state detector, made up of individual silicon semi-conducting sensors. Each having a nominal size in $R-\phi$ of $50\times400\,\mu\text{m}^2$. The sensors are arranged into three barrel layers and three disks for the end-caps. The inner-most layer, at a radius with respect to the beam line $(R) = 5\,\text{cm}$, is important for b-physics and identifying secondary vertices. On average all three layers are hit by each track. The intrinsic accuracies in the barrel are $10\,\mu\text{m}$ (R-ϕ) and $115\,\mu m(z)$. In the disks the R-ϕ resolution is the same, but the $115\,\mu m$ is with respect to R.

The Silicon Microstrip Detector

The silicon microstrip detector uses a similar technology to the pixel detector. However, instead of individual pixels the silicon is arranged in strips. These strips are arranged into four coaxial cylindrical layers in the barrel region and two end-caps which each contain nine disks. In the barrel region, one set of strips in each layer is parallel to the beam direction the other is offset at a small-angle, 40 mrad. This allows the measurement of both co- ordinates in $\eta-\phi$ space. The small angle between the strips was chosen to reduce the problem of distinguishing between multiple hits on the same strip. On average eight strip layers are crossed by each track, providing four space points. However, the actual number of layers crossed within the SCT can vary up and down significantly. Due to large overlaps between neighbouring modules it is quite common for the the number of hits to reach as high as 12. The intrinsic accuracies per module in the barrel are $17\,\mu\text{m}$ (R-ϕ) and $580\,\mu\text{m}(z)$ and $17\,\mu\text{m}$ (R-ϕ) and $580\,\mu\text{m}(R)$ in the disks.

The Transition Radiation Tracker

The transition radiation tracker is made up of 76 layers of straw tubes interleaved with fibres in the barrel and 160 straw planes interleaved with foils in the end-cap. Each straw tube is a wire drift tube made up of a cathode wall and an anode wire running down the middle. The gas mixture the tubes are designed to work with is 70% Xe, 27% CO_2 and 3% O_2, although during test periods other mixtures have been used. On average, each track will pass through 36 straws, providing a spatial resolution in R-ϕ space of $130\,\mu\text{m}$. The extra measurements made radially further out in the detector increase the lever arm allowing a better measurement of track p_{T}. As a charged particle makes the transition from the fibre/foil around the tube wall into the gas it emits radiation, giving the detector its name. This transition radiation can be used to help identify electrons, which give off much larger amounts of radiation compared to pions.

3.2.2. The Calorimeter

The calorimeter is designed to measure the energy of particles, providing information for a multitude of physics objects. It provides coverage over almost the entire solid angle, up to $|\eta| \approx 4.9$. The central region of the calorimeter, $|\eta| < 2.5$, has a much higher granularity in order to aid with precision measurements. The rest of the calorimeter is designed to provide good measurements of jets and electrons. As well as measuring the deposition of energy in the detector, the extensive coverage allows the detection and measurement of the absence of energy due to particles not interacting with the detector, missing transverse energy (E_{T}^{miss}).

The total depth of the electromagnetic calorimeter (ECAL) is greater than 22 radiation lengths (X_0) in the barrel and greater than $24\,\mathrm{X}_0$ in the end-caps. The entire active calorimeter region is about 9.7 interactions lengths (λ) in the barrel and about $10\,\lambda$ in the end-caps. This is enough to provide good resolution of the jet energy. Including the $1.3\,\lambda$ of structural support, the calorimetry is thick enough to stop the majority of hadronic activity from reaching the muon systems. Hadronic activity reaching the muon system, known as punch through, could cause fake muon signals. The rate of punch through has been reduced to levels below the irreducible backgrounds from muons not coming from the hard-process.

The calorimeters closest to the beam line are housed in three cryostats: the barrel and two end-cap cryostats. The barrel cryostat contains the barrel ECAL, the end-cap cryostats contain the end-cap ECALs, hadronic end-cap calorimeter (HEC) and forward calorimeter (FCAL). The layout of the calorimeters is shown in Fig. 3.3.

Liquid Argon Electromagnetic Calorimeter

The ATLAS ECAL uses liquid argon (LAr) as the active material, arranged with accordion-shaped electrodes and lead absorber plates over the full coverage. The active detecting medium for the calorimeter was chosen to be LAr because of its intrinsic linear energy response, stability over time and radiation hardness. The accordion-shaped geometry provides a complete ϕ coverage without azimuthal cracks. As well as this, the layout allows the calorimeters to have several active layers in its depth.

The ECAL is divided into a barrel section, $|\eta| < 1.475$, and two end-cap components, $1.375 < |\eta| < 3.2$. Over the high precision region, $|\eta| < 2.5$, the ECAL is segmented into three sections in depth. The end-cap inner wheel, $2.5 < |\eta| < 3.2$, has two sections in depth. In the region of $|\eta| < 1.8$, a pre-sampling detector is used to correct for unmeasured energy loss by electrons and photons in the calorimetry. The pre-sampler consists of an active LAr layer, with a thickness of 1.1 cm in the barrel region and 0.5 cm in the end-cap. The pre-sampling detector allows measurements

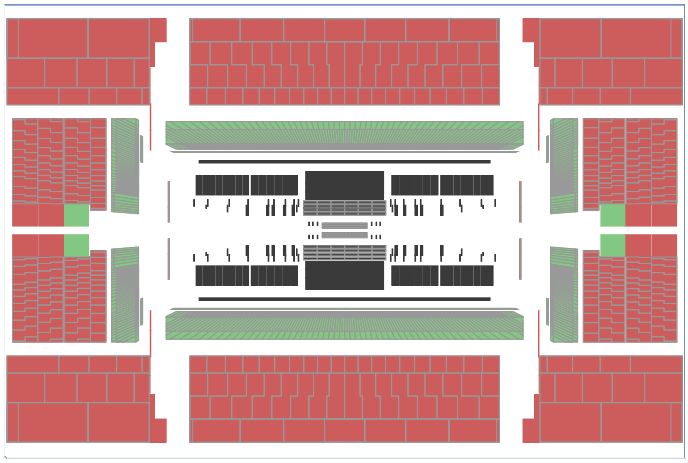

Figure 3.3.: The calorimeter as shown in the $\rho - z$ view of the Atlantis event display. The LAr calorimeters are shown in green and the tile calorimeters are in red. The grey lines show calorimeter segmentation

to be made before energy is lost in the absorber material of the calorimeter and is important for distinguishing between electrons and photons within the calorimeter.

During the testing and construction of the ATLAS detector, the different parts were placed in particle test-beams of known energy and composition. This allows the energy response and resolution to be measured in a relatively clean environment. The information on the LAr calorimeter test-beam studies can be found here: [37–39]. The measurements were fitted, after noise subtraction, to equation 3.4:

$$\frac{\sigma(\mathrm{E})}{\mathrm{E}} = \frac{a}{\sqrt{\mathrm{E[GeV]}}} \oplus b, \tag{3.4}$$

where a is a stochastic term and b a constant representing local non-uniformity in the response of the calorimeter. An electron beam, at $\eta = 0.687$, was used to measure the energy resolution and linearity of response in an energy range from 10 to 245 GeV. The stochastic term was found to be $10\% \cdot \sqrt{\mathrm{GeV}}$ and the constant term to be 0.17%. The linearity was measured between 15 and 180 GeV giving a reconstructed energy response that was linear within $\pm 0.1\%$.

Hadronic End-cap Calorimeter

The HEC is made up of two independent wheels per end-cap, located directly behind the end-cap ECAL. The HEC uses LAr as its active material and copper as the absorber plates. It covers the region $1.5 < |\eta| < 3.2$, overlapping the tile calorimeter in the region $1.5 < |\eta| < 1.7$.

The HEC was tested in an electron and a pion test beam [40]. The electron beam resulted in a stochastic term of $(21.4\pm0.1)\% \cdot \sqrt{\text{GeV}}$ for the fractional energy resolution and a constant term consistent with 0. However, it is the pion beam which is most interesting as it provides data on the calorimeters response to hadrons. Here, the a term was found to be $(70.6\pm1.5)\% \cdot \sqrt{\text{GeV}}$ and b to be $(5.8\pm0.2)\%$.

Tile Calorimeter

The tile calorimeter is a sampling calorimeter that uses steel as the absorber and scintillating tiles as the active material. This provides the most cost effective way to increase radial calorimeter depth, while still meeting the detector criteria. The tile calorimeter is placed directly outside the ECAL envelope. It is split into a barrel region, $|\eta| < 1.0$, and two extended barrels in the range $0.8 < |\eta| < 1.7$. It is segmented in depth in three layers, approximately 1.5, 4.1 and 1.8 λ, respectively, in the barrel region and 1.5, 2.6 and 3.3 λ for the extended barrel.

Standalone measurements were made in hadron test beams with energies ranging from 20 to 180 GeV and a few additional runs at 350 GeV [41]. These were made with respect to different beam angles and energies. Parametrisation of the measurements yielded a stochastic term of $(56.4\pm0.4)\% \cdot \sqrt{\text{GeV}}$ and a constant term of $(5.5\pm0.1)\%$. The fractional energy resolution was found to be very dependent on the beam angle. This is expected because the amount of calorimeter the beam passes through changes. To give a flavour of the variation, for $\eta = 0.25$, $\sigma_{\text{E}}/\text{E} = (14.2\pm0.1)\%$ at 20 GeV and $(6.6\pm0.1)\%$ at 350 GeV, while at $\eta = 0.55$, $\sigma_{\text{E}}/\text{E} = (13.0\pm0.1)\%$ at 20 GeV and $(5.9\pm0.1)\%$ at 350 GeV.

Combined detector test-beams with the LAr and tile calorimeters were done using pion beams with an energy dependent contamination from protons [42]. The calorimeters were arranged to recreate, as much as possible, run-time conditions within the ATLAS detector. The beam was at an angle of 12° to the calorimeter assembly and had an energy range between 10 to 300 GeV. The measurements found a stochastic term of $(52.1\pm1.0)\% \cdot \sqrt{\text{GeV}}$ and a constant term of $(3.0\pm0.1)\%$. The electronic noise term was found to be $1.6\,\text{GeV}\pm0.1\%$.

3.2.3. The Muon System

The muon spectrometer is a series of detectors outside the calorimeter. The depth of the calorimetry ensures the majority of charged particles reaching the muon systems will be muons. The charged particles can be detected within a range of $|\eta| < 2.7$, and triggered on within a range of $|\eta| < 2.4$. The performance goal was to be able to measure a 1 TeV track with a momentum resolution of 10% and charged particles down to a few GeV using just the muon spectrometers.

The muon system relies on the magnetic deflection of the muon tracks in the large superconducting air-core toroid magnets. In the region $|\eta| < 1.4$, the magnetic bending is provided by the large barrel toroid. For $1.6 < |\eta| < 2.7$, muon tracks are bent by two smaller end-cap magnets inserted into both ends of the barrel toroid. Muons going between these two regions are affected by a combination of the two systems. The air-core magnet design minimises the amount of material traversed by the muons after the calorimeter. This is an important feature, as material interaction dominates the momentum resolution between 30 and 200 GeV.

The muon chambers in the barrel are arranged in three concentric cylindrical shells around the beam at radii of approximately 5 m, 7.5 m and 10 m. In the end cap regions, the muon chambers form large wheels perpendicular to the z-axis. These are located at a distance of $|z| = 7.4$ m, 10.8 m, 14 m and 21.5 m respectively. In the centre of the detector, $|\eta| \sim 0$, there is a gap in the coverage to allow access for servicing of the solenoid magnets, calorimeter and inner detector. The layout of the muon system can be seen in Fig. 3.4. The muon system is made up of multiple detector technologies, which are grouped into two primary uses, precision-tracking chambers and trigger chambers.

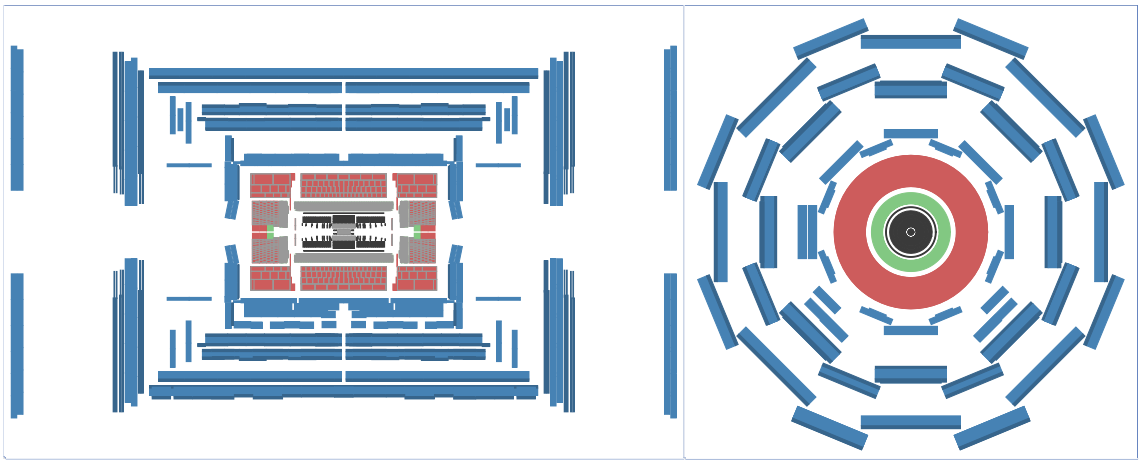

(a) $\rho - z$ **(b)** $x - y$

Figure 3.4.: The muon system, in blue, as shown in the Atlantis event display.

Precision-Tracking Chambers

The precision-tracking chambers make use of two technologies, monitored drift tubes (MDT) and cathode-strip chambers (CSC).

The MDT chambers perform the precision momentum measurements of the tracks passing though the muon system for the majority of the η-range. This system covers

the range $|\eta| < 2.7$, except in the inner most end-cap layer where their coverage is limited to $|\eta| < 2.0$. The layout of the MDT is projective, each layer's dimensions increase in proportion to their distance from the interaction point. MDT were chosen because they combine high measurement accuracy, predictability of mechanical deformations and simplicity of construction. The MDT chambers consist of 3 to 8 layers of drift tubes, which operate at a pressure of 3 bar. Each tube achieves an average resolution of 80 μm in the bending plane and each chamber a resolution of 35 μm.

The CSC cover the forward region, $2 < |\eta| < 2.7$, of the inner-most muon wheel. CSCs are used instead of MDTs here because of the large particle flux, thus the higher rate capability and time resolution of the CSC is needed. The resolution of the CSC is about 40 μm in the bending planes and about 5 mm in the non-bending plane. Both co-ordinates of a track are measured simultaneously, in four consecutive planes. The CSCs are multiwire proportional chambers, arranged into two disks with eight chambers. Each chamber has 4 CSC planes.

When working at the maximum design rate, 1 kHz/cm^2, the CSC resolution degrades from 45 μm to 65 μm. At these high rates, the single layer inefficiency to measure a track increases from 4% to 10%. This is considered acceptable as the chance for all four layers in the CSC plane to miss the track is small. To achieve the stated resolutions, the locations of the MDT wires and CSC strips must be known to an accuracy better than 30 μm. This is done by using a high-precision optical alignment system, which monitors the positions of the precision-tracking chambers and internal deformations of the MDT chambers. The optical system is also complemented by a track-based alignment.

Trigger Chambers

In the barrel region, $|\eta| < 1.05$, resistive plate chambers (RPC) are used to trigger muon events. In the end cap, $1.05 < |\eta| < 2.4$, thin gap chambers (TGC) are used. Both technologies deliver signals within a spread of 15–25 ns, thus providing the ability to tag the associated bunch crossings.

The RPC is arranged in three concentric cylindrical layers around the beam axis, providing good spatial and time resolution as well as adequate rate capability. The large lever arm between the inner and outer chambers permit the triggering of the tracks in the 9–35 GeV range. Low p_{T}, 6–9 GeV, muons are triggered with the inner two chambers. RPCs are made of two parallel electrode plates, filled with a gas mixture of $C_2H_2F_4/SoC_4H_{10}/SF_6$. The wireless design simplifies their construction and makes them less sensitive to small deviations from planarity.

The TGCs primary role is to trigger on muons within in the range $1.05 < |\eta| < 2.4$. However, they also provide additional information about the azimuthal co-ordinate

to complement the measurement done in the MDT. TGCs operate on the same principle as multiwire proportional chambers, providing good time resolution and high rate capability.

3.2.4. The Trigger and Data Acquisition

The LHC provides ATLAS around 10^9 collisions per second at design luminosity. It is impossible to record all these collisions, so ATLAS uses specialised hardware and computer algorithms to keep only the interesting events. These algorithms, known as the triggers, are separated into three layers: Level 1 (L1), Level 2 (L2) and the event filter (EF). The L2 and EF stages are collectively known as the high-level trigger (HLT). The design rate after all levels of triggering is about 200 Hz which can stretch up to about 1 kHz for short periods of time. During actual running in 2012, the event rate was about 400 Hz.

There are cases when a physics signature is of interest, but it occurs at a far higher rate then can be recorded. These type of events are dealt with using 'prescales'. A prescale allows some events to be accepted but rejects the rest. Each trigger level can have different prescales, for instance a signature can be heavily prescaled at L1, but L2 and EF will accept all events of that type that reach them. This is of use when an exclusive signature trigger is seeded from an inclusive one. All events that pass a trigger prescale are assigned a weight to account for itself and all the events that failed to pass the prescale. When these prescale weights are applied to the accepted events, an unbiased distribution can still be created.

Level 1 Trigger

The L1 trigger reduces the event rate to 75 kHz and has on average $\sim$2.5 μs to make a decision per event. In order to process events fast enough, L1 is implemented using custom-made electronics. The L1 trigger looks for inclusive signatures to minimise the risk of excluding any interesting, but unknown, physics. This is done by searching for single physics objects, such as jets, leptons or missing transverse energy (E_{T}). Once the trigger has identified an interesting physics object, it passes the location up the chain as a Region of Interest (RoI). This RoI seeds L2. The L1 trigger is based on information from the calorimeter and muon trigger systems. The L1 calorimeter trigger system (L1Calo) uses information from all the calorimeters and aims to identify high E_{T} physics objects or large E_{T}^{miss}. The trigger decision is based on the multiplicity of hits for 4 to 16 programable E_{T} thresholds per object type. For the majority of η, the L1Calo has a granularity of 0.1×0.1 in $\Delta\eta \times \Delta\phi$. For higher $|\eta|$ the granularity decreases.

The L1Calo system identifies jets using a 'sliding window' which scans over $\eta - \phi$ space to identify energy deposits. The basic window size is 0.2×0.2, but increases for higher energy jets. To avoid double counting, the local energy maximum in the window must be in the centre for it to be considered. Once a jet candidate has been identified, the measured energy is compared to pre-defined thresholds. The central jet triggers extend out to $|\eta| < 3.2$ [43].

Level 2 Trigger

On receiving the RoI from L1, the L2 trigger has about 40 ms to process the event. This reduces the event rate down to 3–5 kHz. To save time, the L2 trigger only looks at the region of the detector identified by the RoI. As with the L1, the L2 triggers on inclusive signatures. The event selection is done with specialised software located on a computing farm near the detector. The system is designed to reduce the rate by about a factor of 30. In most cases the L2 decision is made using only information within the RoIs.

Event Filter

The EF makes its decision based on the entire event. Using 'offline-like' algorithms, it makes the final selection of events that will be used in later analyses. This is unlike the L2 trigger, which needs to use specialised algorithms that are optimised for speed. The EF does the final rate reduction, bringing the rate down to around 400 Hz. As the event filter has the full event information, it can select more exclusive signatures. The L2 and EF infrastructure is located entirely outside of the detector in a processing farm. From there, each event is classified and fed into a specific physics stream.

Data Acquisition

The data acquisition (DAQ) provides the configuration, control and monitoring of the ATLAS detector during data-taking. In addition to this, the DAQ system receives and buffers event data from the detector. During the L1 trigger decision, events are buffered in the front-end electronics. If the L1 trigger system accepts the event, then the full event information is passed onto the HLT/DAQ system and the relevant parts of the event information are passed to the L2 trigger. The full event building is done only on events that pass L2. Information from an event that passes L2 is then sent to single computing node (SFI). These nodes turn the information into an event-data structure usable by the event filter. There are many SFIs, each handling events concurrently with the other SFIs in the system. A central system is in control of the allocating of event to ensure an even usage of the available SFIs. The L2

trigger will accept some events for calibration of the detector system, in these cases the SFI will only gather the event data from the relevant detector sub-systems. As well as acting as a final means of reducing the event rate, the event filter classifies the event with respect to different pre-defined streams. These streams mostly represent which physics area of interest the event likely belongs to. Events that pass the EF stage are classified into a stream and are then moved to permanent storage. Between the time an event is being handled by the DAQ/HLT and written to disk, the event is stored on the event-filter output nodes. The main reason for these nodes is to provide storage during times when the link to CERN's central data-recording service is down. If such a situation occurs, the output nodes can store up to 24 hours worth of events from the ATLAS detector.

Chapter 4.

Technical Tools

This chapter discusses the common tools, physics objects, and methods that are used by analyses described later in this thesis.

4.1. Jets

When a quark or gluon is produced in the hard process, it quickly radiates and hadronises into a shower of particles. While there is plenty of interesting physics in these additional particles, for most physics areas of interest at the LHC, the particles from the hard process are the focus. Clustering algorithms are used to get back from the spray of particles to their source. These create a proxy for the hard process parton, known as a 'jet'.

The jet clustering algorithms can be broadly grouped into two categories: cone algorithms and sequential recombination algorithms. Cone algorithms are computationally much simpler, they create a cone of fixed radius in $\eta - \phi$ space around a particle/energy deposit. The highest energy object seeds the majority of cone algorithms, i.e. the centre of the cone is this object. All objects within this cone are combined into a single jet, and then the jet is removed from the list of objects when looking for the next jet seed. This approach leads to inconsistency when trying to apply a cone algorithm on particles. Assume that the hardest particle in an event is a gluon; this will be the seed that the cone is built around. However, if the gluon emits a colinear gluon it may no longer be the hardest particle, and the jet will be seeded by a different particle. If the new seed leads to a different final set of jets, then theoretical divergences no longer cancel. A similar issue can occur with soft emissions at larger angles. These problems are known as infrared and collinear safety. Sequential recombination algorithms avoid this problem. These algorithms are generically described by equations 4.1 and 4.2 [44]:

$$d_{ij} = min(k_{ti}^{2p}, k_{tj}^{2p}) \frac{\Delta_{ij}^2}{R^2}, \tag{4.1}$$

$$d_{iB} = k_{ti}^{2p}, \tag{4.2}$$

where d_{ij} can be thought of as a distance parameter between two objects. The 'closest' objects are combined first. Δ_{ij} is the ΔR between the two objects, and the R^2 parameter is a distance cut off. The ratio imposes 'cone-like' qualities to sequential recombination algorithms by imposing $\eta - \phi$ distance considerations when combining objects. For the Cambridge-Aachen algorithm [45], where $p = 0$, the distance parameter is the angle between two objects. In this case, it can be seen that if there is a co-linear emission this will be recombined first, and soft large angle emissions shouldn't affect the overall kinematics of the jet. Thus, the final list of jets will be the same, regardless of soft or collinear emission.

Historically, hadron colliders have favoured cone algorithms and lepton colliders favoured sequential recombination algorithms. This is, primarily, because the complicated environment in hadron colliders made sequential recombination algorithms computationally too expensive. There are other practical considerations as well: the nature of cone algorithms makes them easier to deal with experimentally. The known jet area and radius makes calibration and corrections much easier, compared with the fluid boundaries of most recombination algorithms. However, developments in the field of jet algorithms have led to a new algorithm that combines the advantages from both algorithm types. The algorithm used in modern collider experiments is known as the anti-k_t algorithm [44], it is a sequential recombination algorithm with a p value of –1. This algorithm is both infra-red and collinear safe making it theoretically preferable, and in most cases it also forms perfect cones, with radius R, making it experimentally practical. Importantly, it is also computationally quick.

4.1.1. Jets in ATLAS

Jets are reconstructed in the 'A Toroidal LHC ApparatusS' (ATLAS) detector from energy deposits in the calorimeter. The analyses discussed in chapters 5 and 6 form jets from positive energy topological clusters (topo-clusters). A topological cluster is a group of neighbouring calorimeter cells designed to take advantage of the ATLAS calorimeter segmentation and follow the development of a hadronic shower. The topo-cluster formation algorithm starts from a seed cell whose signal, S, to noise, N, ratio is above the threshold S/N = 4. Neighbouring cells that have a S/N > 2 are added iteratively. The last step is to add all neighbouring cells to the formed topo-cluster. The energy of the topo-cluster is defined as the sum of the energy of all its cells, its mass is zero and its reconstructed direction is the energy weighted average of the pseudo-rapidities and azimuthal angles of the constituent cells. The weighting is done with respect to the absolute energy of the cell and its position relative to the nominal ATLAS coordinate system. In MC, particle or 'truth' jets can be made from particles in the event. The jets use all stable particles as input for

the jet algorithms, where a stable particle is defined as those with a lifetime greater than 10 ps.

4.1.2. Jet Calibration

In order to correct the measured energy of a jet to that of the energy of the particles entering the calorimeter, a series of calibrations are applied [46]. Due to the small datasets, comprehensive data-driven *in-situ* studies were not possible for early calibrations. As such, the majority of the initial studies were done primarily in MC computer simulation. It is possible to rely on MC for calibration due to extensive test-beam measurements to tune material interaction within the simulation. In addition to test-beam verification of the MC, in-depth systematic studies were done on the results given by the simulation. The quoted uncertainties on the jet measurement accuracies are considered to be conservative. The detector effects accounted for by the calibrations are listed below.

- **Calorimeter non-compensation**: energy from a hadronic shower is only partly measured.
- **Dead material**: energy losses in inactive regions of the detector.
- **Leakage**: energy loss from particles that are not fully contained within the calorimeters.
- **Out of calorimeter jet cone**: energy deposits from particles that are not reconstructed in the calorimeter jet, but were contained within the associated particle jet.
- **Noise threshold and particle reconstruction efficiency**: signal losses in the calorimeter clustering and jet reconstruction.

The energy measured in the calorimeter is recorded at the electromagnetic (EM) scale. This relates to the calibration used to measure the energy deposition in the calorimeter from EM showers. This differs to the hadronic scale. Where the energy of an EM shower can, in theory, be fully measured, the energy of an hadronic shower can not. Effects such as nuclear break-up caused by energetic hadrons and the creation of low energy neutrons mean part of the energy from the hadronic shower is invisible to the calorimeter. The EM-scale is calibrated originally from test-beam data, and later through *in-situ* methods such as $Z \rightarrow e^+e^-$ measurements.

The simplest calibration scheme applies corrections directly to the measurements made at the EM scale. This method allows straight-forward evaluation of the systematic uncertainty from single hadron test-beam measurements and MC variation. Most importantly, this can all be evaluated with small data sets and is thus suitable for early physics analyses. This scheme applies energy and η dependent corrections to

the jets energies measured at the EM scale. It is known as the EM+JES calibration scheme and is implemented in three steps:

1, multiple proton-proton collision correction,

2, vertex correction, and

3, jet energy and direction correction.

During normal running conditions at the LHC, there can be multiple proton-proton collisions per bunch crossing. This phenomenon, known as pile-up, will add energy to jets coming from the proton-proton collision of interest. The presence of pile-up can be modelled by having multiple inclusive collisions overlapping with each other, with the net effect of depositing energy uniformly around the detector. The additional energy can be calculated on an event-by-event basis, and subtracted from the energy measured for a jet. The correction is calculated with respect to the η of the jet, number of collision vertices reconstructed in the event, N_{PV}, and the bunch spacing, τ_{bunch}. This can be expressed in the mathematical form shown in equation 4.3:

$$E_T^{Corrected} = E_T^{Uncorrected} - O(\eta, N_{PV}, \tau_{bunch}), \tag{4.3}$$

where N_{PV} acts as a proxy for the number of proton collisions. The offset is proportional to the area of the jet, which is contained in the η information. It is worth noting that this correction is only effective over a large number of events and jets. The uncertainty related to the energy introduced to a jet from each pile-up collision means that at the level of an individual jet the reduction in uncertainty is small.

The initial measurement of a jet is done with respect to the nominal centre of the ATLAS detector. However, as the collision that created the jets of interest most likely did not happen there, this leads to a small mismeasurement in the jet p_{T} and direction. To account for this, the collision vertex that produced the jets is identified. The direction of the topo-clusters is then corrected to be with respect to the collision vertex, rather than the nominal centre. The collision, or primary, vertex is identified by the vertex with the largest value for equation 4.4. This correction improves the angular resolution of jets and has a small effect on the p_{T} ($< 1\%$).

$$p_{\mathrm{T}}^{vertex} = \sum_{i < n_{trk}} p_{\mathrm{T}}^{trk,i}, \tag{4.4}$$

where the tracks are those originating from the vertex.

The jet energy and direction corrections are applied using multiplicative factors derived from the MC simulation. The direction correction is implemented to correct for poorly instrumented regions of the detector. When a jet deposits energy over a well instrumented and a poorly instrumented region of the detector, the jet direction is biased towards the well instrumented region. In general this is a small effect, but

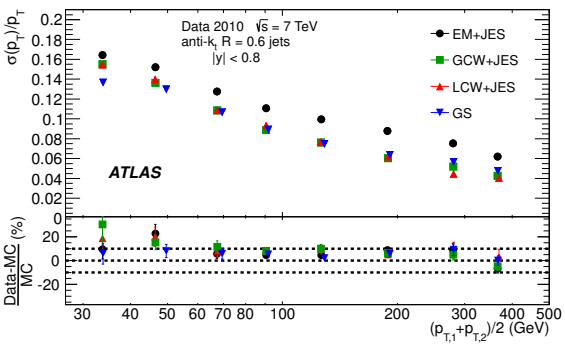

(a) Jet Energy Resolution [47]. Top Panel shows the jet energy resolution measured in data for different calibration schemes. The bottom panel compares the resolution in data to MC. No MC is shown in top panel

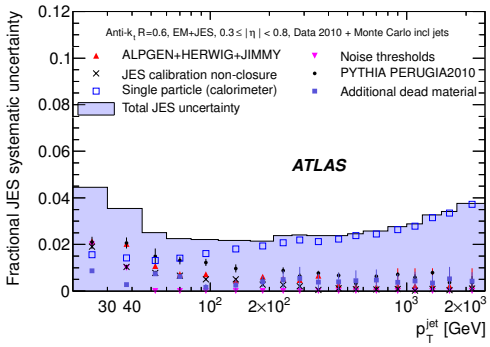

(b) Jet Energy Scale for the EM+JES calibration scheme [46]

Figure 4.1.: Jet energy resolution and scale used for 2010 analyses.

becomes larger at the transition regions. The energy correction is determined in bins of E^{jet}_{truth} and η_{det}. The choice of η_{det} over the corrected η is because this relates more closely to the detector design. The energy correction is found from the average jet energy response and average energy in the (E^{jet}_{truth}, η_{det})-bin. The energy response for a single jet, $\mathcal{R}^{jet}_{EM}$, is given in equation 4.5:

$$\mathcal{R}^{jet}_{EM} = \frac{E^{jet}_{EM}}{E^{jet}_{truth}}. \tag{4.5}$$

The average response for jets depends on their energy, for low energy jets this factor can be as large as 2 but drops down to around 1.2 as energy increases.

As more data is collected, better methods to calibrate and understand the detector become available. This allows a more accurate measurement of the jet energy scale (JES) and jet energy resolution (JER). The JES is the overall calibration of the jet energy, while the JER is the accuracy to which the energy can be measured. The difference between the 2010 and 2011 jet uncertainties can be seen in figures 4.1 and 4.2. The uncertainty on the JES has halved going from 2010 to 2011. This is primary due to the much larger data set allowing insitu measurements to be made, such and Z+jet and γ+jet measurements.

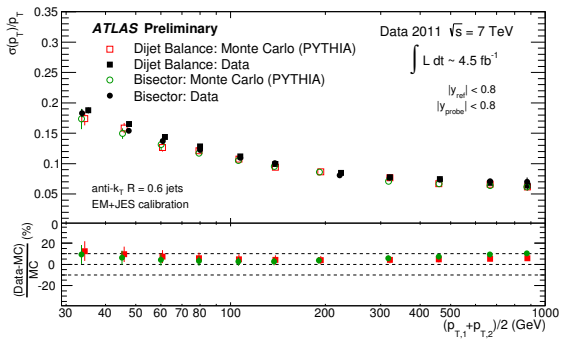

(a) Jet Energy Resolution [48]. Top panel shows the jet energy resolution in data and MC for different methods. Bottom panel shows the relative difference to data points and a fit done to the MC results from top panel.

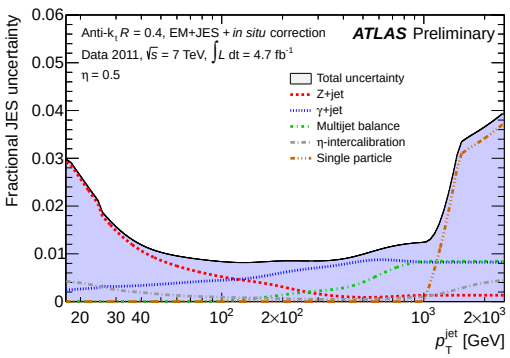

(b) Jet Energy Scale [49]

Figure 4.2.: Jet energy resolution and scale used for 2011 analyses.

4.2. *b*-tagging Algorithms

The identification of b-jets plays a large role in physics at the LHC, such as in the top-quark sector and searches for new physics. Is it especially important in the Higgs system, where H$\rightarrow b\bar{b}$ is the primary decay channel for a low mass Higgs. For the analyses covered in this thesis a jet's flavour is defined with respect to hadrons. If the jet contains a b-hadron with $p_{\mathrm{T}} > 5\,\mathrm{GeV}$ within $\Delta R < 0.3$ to the jet-axis then the jet is labelled a b-jet. The jet-axis is defined as the vector from the primary vertex to the centre of the jet. If the jet does not contain a b-hadron, but contains a c-hadron meeting the same criteria, it is labelled a c-jet. All other jets are defined to be 'light', i.e. originating from light quarks. In ATLAS, and throughout this thesis, a heavy flavour 'labelled' jet refers to its flavour being identified with respect to particle level information, while heavy flavour 'tagged' refers to a b-tagging algorithm's output. Generically, the value of a b-tagging algorithm's discriminating variable is known as its b-tagging weight. Algorithms used for b-tagging can be split into two categories, those that look for characteristics of a displaced vertex and those which look for the semi-leptonic decay of a b-hadron. The former are known as life-time based taggers, while the latter are known as muon-based taggers.

4.2.1. Track Requirements

For lifetime-based taggers, variables associated to tracks are the main input. The point at which a track is the closest to the primary vertex, the impact parameter, is used to discriminate tracks that originate from the primary vertex and those that do

	SV0	JetFitterCombNN
p_{T}	$> 0.5\,\mathrm{GeV}$	$> 1\,\mathrm{GeV}$
d_0^{PV}	$< 2\,\mathrm{mm}$	$< 1\,\mathrm{mm}$
$z_0^{PV}\ \sin\theta$	$< 2\,\mathrm{mm}$	$< 1.5\,\mathrm{mm}$
$\sigma(d_0^{PV})$	$< 1\,\mathrm{mm}$	N/A
$\sigma(z_0^{PV})$	$< 5\,\mathrm{mm}$	N/A
$\chi^2/ndof$	< 3	N/A
Number of Pixel hits	≥ 3	≥ 2
Number of SCT hits	≥ 4	N/A
Number of Pixel+SCT hits	≥ 7	≥ 7
b-layer hits	N/A	≥ 1

Table 4.1.: b-tagging track quality requirements.

not. This parameter is measured in the transverse plane, d_0, and the longitudinal direction, $|z_0|\sin\theta$. To give a higher weight to better-measured tracks, the impact parameter over its error is often used, i.e. $d_0/\sigma(d_0)$, this is known as the impact parameter significance. If the vector from the primary vertex to the point of closest approach of a track is defined as $\mathbf{c}$, then the projection of $\mathbf{c}$ onto the jet-axis, $\mathbf{j}$, provides additional discriminatory information. As the flight path of the b-hadron is within the jet, the tracks coming from the b-hadron decay should have a positive value for $\mathbf{c}\cdot\mathbf{j}$. If the jet is defined to be in front of the primary vertex, then the track's, from a b-hadron, point of closest approach will also be in front of the primary vertex. This is quantified by assigning a sign to the impact parameter, where the sign is the same as the sign of $\mathbf{c}\cdot\mathbf{j}$.

It is important that the tracks used in the algorithms are well measured. As such, certain track quality requirements are imposed. These are listed for the two algorithms used for this thesis in Table 4.1.

Sources of confusion for the b-taggers are other long-lived particles and material interactions. These lead to tracks with a high impact parameter in light jets. To reject such tracks, any two-track combinations that are consistent with a single source not compatible with the primary vertex and have a mass consistent with a K_S^0, Λ^0 or other hyperon are rejected. Any two tracks that have a vertex position consistent with a pixel layer are also rejected.

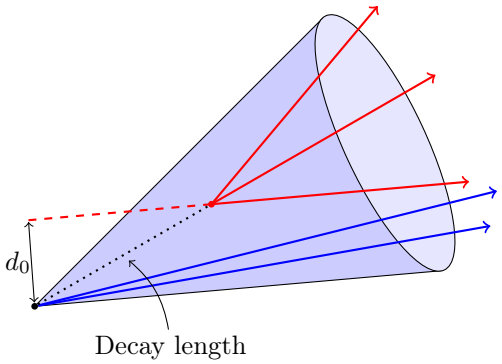

Figure 4.3.: Diagram illustrating variables of the SV0 tagging algorithm

4.2.2. SV0

The SV0 b-tagging algorithm [50] is a comparatively straightforward b-tagger, designed to be used with early data. It is used for the measurement described in Chapter 5, using the 2010 ATLAS data. The algorithm uses tracks within the jet to attempt to reconstruct a secondary vertex from the decay of a b-hadron in the jet. If the algorithm does reconstruct a secondary vertex, it uses the signed decay length significance, $L/\sigma(L)$, of the displaced vertex as the discriminating variable, where the decay length, L, is the distance from the primary to the secondary vertex, and the sign is decided by the position of the secondary vertex with respect to the jet-axis. This can be seen diagrammatically in Fig. 4.3. If the algorithm fails to reconstruct a secondary vertex, the jet is assumed to be a light jet.

Tracks are matched to a jet if they are within a $\Delta R < 0.4$ to the jet axis. If a track could be matched to multiple jets, it is assigned to the closest. To reconstruct a secondary vertex with the track associated to a jet, the SV0 algorithm starts by trying to reconstruct two-track vertices that are significantly displaced from the primary vertex. Tracks are considered for the secondary vertices if their $dca/\sigma(dca)$ is greater than 2.3, where $dca/\sigma(dca)$ is the 3D impact parameter significance. In addition to this, the sum of the two tracks $dca/\sigma(dca)$ must be greater than 6.6. The two tracks must be compatible with originating from a secondary vertex, which is quantified by $\chi^2 < 4.5$, and the secondary vertex must be incompatible with the primary vertex as quantified by $\chi^2 > 6.25$.

The tracks surviving in the two-track vertices are then combined into a single vertex. The algorithm then iteratively removes the tracks that are least likely to have come from the secondary vertex until the overall probability that the remaining tracks came from a common vertex is good. 'Good' is quantified as a fit probability greater than 0.001, the vertex mass is less than 6 GeV and the χ^2 contribution coming

from any one track is less than 7. Finally SV0 tries to re-incorporate the tracks that failed the two-track vertex selection into the vertex fit.

4.2.3. JetFitterCombNN

The JetFitterCombNN b-tagging algorithm is a combination of the IP3D and JetFitter b-tagging algorithms [36]. It is classified as a 'high-performance' algorithm because its light jet rejection ability is far greater than the SV0 algorithm, which means it can work at higher b-tagging efficiencies. It was used widely in ATLAS for the 2011 analyses, including the measurement presented in Chapter 6 of this thesis.

The IP3D b-tagging algorithm compares input variables from jets to pre-defined smoothed and normalised distributions for both the b- and light jet hypotheses. The distributions from data and MC are compared using a likelihood ratio technique. The input variables are the two-dimensional histograms of the signed transverse impact parameter significance and the signed longitudinal impact parameter significance. The input to the likelihood fit is the ratio of the jet's parameters and the reference distributions.

The JetFitter [51] algorithm makes use of the weak b- and c-hadron decay inside the jet. Unlike the SV0 algorithm, JetFitter takes into account the c-hadron lifetime and decay vertex. To explicitly reconstruct both vertices is challenging, thus this algorithm makes the assumption that all decays happen along the b-hadron flight axis, furthermore, that all tracks from the heavy quark decay come from this line. A Kalman fitter is used to find the common line on which the primary, b- and c-vertices lie, as well as their position on the line. With this approach, the b- and c-hadron are not necessarily merged, even if they have only one associated track each. The discrimination between jet types is done using a likelihood fit, using variables based on the number of track vertices and the characteristics of the vertices.

The IP3D and JetFitter algorithms are combined using an artificial neural network that is trained using MC simulation.

4.2.4. Scale Factors

Rather than a straight true/false output from b-tagging algorithms, they produce a continuous weight that is constructed by combining information that discriminates b-jets from light jets. Working points in this continuous spectrum are found using MC by balancing good b-tagging efficiency with a good light jet rejection rate. For the SV0 algorithm used in the analysis described in chapter 5, a 50% b-tagging efficiency working point was used. The analysis in chapter 6 used JetFitterCombNN with a working point of 70% b-tagging efficiency. The difference in the working

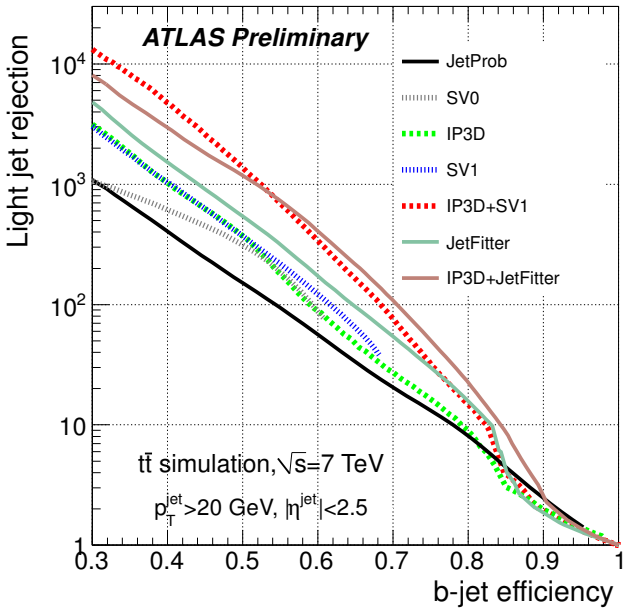

Figure 4.4.: Expected light jet rejection rate for different b-tagging algorithms [36]. JetFitterCombNN is labelled as IP3D+JetFitter in this plot.

points reflects the algorithms different ability to reject light jets. The working points for the SV0 and JetFitterCombNN algorithms accept about 0.5% and 1% of light jets, respectively. The expected light jet rejection rates for different b-tagging algorithms can be seen in Fig. 4.4. JetFitterCombNN (IP3D+JetFitter) has an order of magnitude better light-jet rejection for the same b-jet efficiency.

Using independent b-jet identification methods, the working points for the algorithms are calibrated in data. The calibrations [52] are published in the form of scale factors, $\kappa_{\epsilon_b}^{data/sim}$, which are defined as the ratio of the b-tagging efficiency found in data over the efficiency found in simulation:

$$\kappa_{\epsilon_b}^{data/sim} = \frac{\epsilon_b^{data}}{\epsilon_b^{sim}}. \tag{4.6}$$

The data efficiency, ϵ_b^{data}, is found for a given algorithm with respect to a sample of b-jets found using an independent method. The efficiency predicted for b-jets by the MC, ϵ_b^{sim}, is found with respect to b-labelled jets. These scale factors are derived with respect to the p_{T} of the b-jet and represent the difference in the performance of the algorithms in data and MC. The scale factors are applied as an event weight to the simulation when deriving quantities to do with b-tagging, such as calculating the b-tagging efficiency for a given distribution. Examples of the scale factors for the SV0 and JetFitterCombNN algorithms can be seen in figures 4.5 and 4.6.

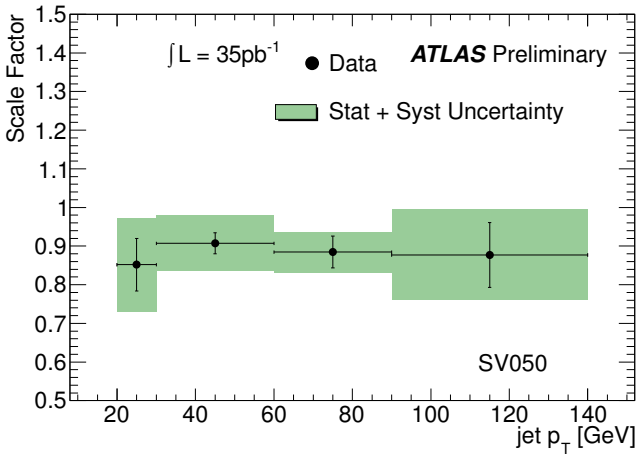

Figure 4.5.: SV0 scale factors for a 50% b-tagging efficiency [52].

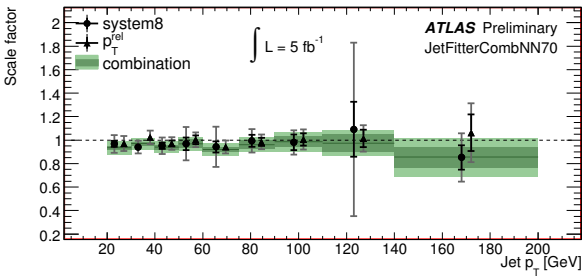

Figure 4.6.: JetFitterCombNN scale factors for a 70% b-tagging efficiency [53].

The uncertainty of the calibration of the algorithm is translated to a measurement uncertainty by rerunning the analysis with the scale factor weights shifted up and down by one standard deviation of their uncertainty. For the analysis discussed in chapter 5, the independent method for a data driven calibration was $p_{\mathrm{T}}^{\mathrm{rel}}$ [36, 52]. This method uses the relative transverse momentum of a muon, produced in a semi-leptonic decay, with respect to the jet axis to differentiate jet flavour. This method is limited in its ability to differentiate high p_{T} b-jets due to jets becoming more collimated. Thus, scale factors were only available to b-jets with a p_{T} below 140 GeV. Any jets with a p_{T} above this point used a scale factor for a 139 GeV jet, but with the value of the propagated uncertainty doubled. The greater dataset available in 2011 and additional methods for calibrating the JetFitterCombNN algorithm meant scale factors where available up to 200 GeV. For jets above 200 GeV, the 199 GeV scale factor was used with the uncertainty doubled. The process for calibrating the b-tagging efficiency values is the same for the light jet rejection rates, which has a similar way of propagating the associated uncertainties through a measurement.

4.3. Unfolding

While every effort is made to make the measurements from the ATLAS detector as accurate as possible, there will always be residual effects due to experimental resolution and other detector effects. To compare measurements to theoretical predictions, these effects need to be taken into account. This can be done in two ways: either the theoretical predictions can be 'folded' by applying detector effects to the results, or the detector measurements can be 'unfolded'. The unfolding step accounts for detector effects and removes them from the measurement. As the experimentalist generally has a much deeper understanding of their detector, it is customary for the experimental measurement to be unfolded.

4.4. Monto Carlo Generators

Monte Carlo generators have become an indispensable tool for doing physics at the LHC. They allow specific physics processes to be simulated, giving the user insight into the behaviour of the physics process of interest. Modern Monte Carlo generators provide a complete description of the physics involved in proton-proton collisions ranging from the hard scatter to the hadronisation. When combined with detector simulation, they provide individual events in the same format as data events. This allows the same analysis software to be run over both and provides key information into the composition and physics source of the data events.

Historically, two Monte Carlo programs have been dominantly used, those created by the Pythia and Herwig groups. Each uses different assumptions and models to describe the the physics of a proton collision. With the increase in computing resources, different approaches are being developed. This is leading to new Monte Carlo groups, such as the Sherpa and Alpgen groups, which bring new methods and models. Monte Carlo generators can be split into distinct steps, each dealing with a different aspect of the physics process requiring different models.

4.4.1. Matrix Element

The matrix element is the part of the calculation that is exact up to the stated order in perturbation theory. Currently most processes are available up to NLO, but using LO matrix elements is still a common choice. This step in the simulation process generates the hard incoming and outgoing partons. These partons will then be passed to the parton shower.

4.4.2. Parton Shower

In QED, accelerated charged particles radiate. This is also true in QCD. However, as gluons are also (colour) charged, this leads to a cascade of partons. As this behaviour isn't present in the LO approximation, the parton shower fills in the radiation and decay of the particles from the hard process. The parton shower simulates the physics from the energy scale of interaction down to the region where pQCD breaks down, around 1 GeV. Starting with the hard parton, the parton shower calculates the chance for a decay or emission to happen within a given region of phase space. Where the phase space the shower moves through is dependent on the 'ordering' of the parton shower. The default ordering for the Pythia parton shower is p_{T} ordered. The parton shower starts by calculating the chance for a large p_{T} emission, then the change for a slightly lower p_{T} emission, and works its way down. The Herwig parton shower uses an angular ordered parton shower. Here the partons with the largest angle, with respect to direction of travel of the emitting parton, are emitted first. The reasons for this are discussed later.

Methods for modern parton showers can be thought of as theoretically valid for angles close to the original parton. The higher angle at which a particle is emitted from the original parton, the more the model is stretched. Parton shower models are able to fill in one extra hard jet to an event with reasonable accuracy. This is achieved through the angular ordering of parton emissions. Emitted gluons are colour connected, leading to interference between different emissions. However, gluons only see the combined colour charge of partons at smaller angles from them, allowing the emission to be treated independently if the emissions are angular-ordered. The radiation spectrum from heavy quarks is related to the angle of the emission. For

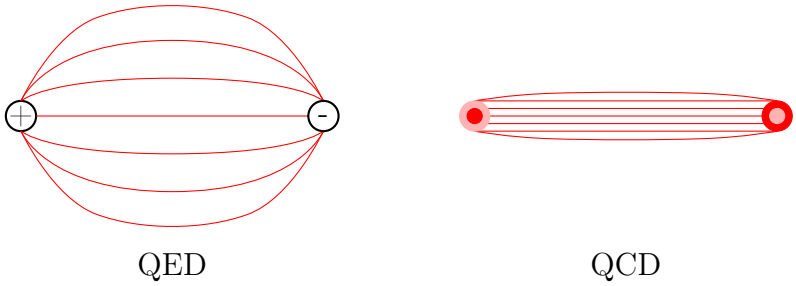

Figure 4.7.: Field lines between two charged particles for QED and QCD.

large angle emissions, the heavy quark emits like light quarks; however, for small angles they stop emitting. In Herwig this is treated with a hard cut off in the emission, where the heavy quark does not radiate below $\theta_0 = \mathrm{m}_q/\mathrm{E}_q$. This is known as the 'dead-cone' effect. While parton showers can deal with one extra hard emission, multi-jet events are not expected to be predicted well. However, parton shower models have many tunable parameters, and it has been shown that good results for multiple jets can be obtained with specific tunes of the parton showers. Once the parton shower has reached the limits of pQCD, the produced particles are passed to the hadronisation step.

4.4.3. Hadronisation

At around 1 GeV and below, our ability to calculate QCD with perturbation theory breaks down. As such, the physics simulation at this level is based on different models and approximations. The dominant affects at this energy are the formation and decay of hadrons, known as hadronisation. There are two main approaches in hadronisation modelling, the string model and the cluster model.

The motivation for a string model, for instance the Lund string model [54] as implemented in Pythia, can be understood when considering the field between two charged particles, Fig. 4.7. In both the QED and QCD case, field lines connect the two particles. However, for QCD the gluons are also charged and attracted to each other. This leads to a linear potential and confinement. From measuring the quarkonia spectrum this linear, or 'string', potential is found, $k \approx 1\,\mathrm{GeV\,fm^{-1}}$. As colour connected particles get further apart, the potential between them increases and they are drawn back together. For ground state mesons, this leads to 'yo-yo modes' where the two quarks oscillate back and forth. When the two quarks have more energy, they can go further apart. This produces an intense chromatic field between them and allows $q\bar{q}$-pairs to be created from quantum tunnelling. The four quarks in the system become two colour-neutral pairs that carry on oscillating. Baryons can be pictured as three quarks attached to a common centre. When they

become particularly energetic, the system acts like a single quark oscillating with a tightly bound quark pair. The string model has a strong theoretical motivation and leads to many good features such as smooth matching to the parton shower, independent fragmentation, and universal treatment of emissions.

The cluster model, as implemented in Herwig, takes advantage of the colour structure of the parton shower. The colour flow through the particles in the parton shower leads to colour-singlet pairs ending up close to each other in phase space, this is known as 'preconfinement'. A useful feature of these colour singlets is that they are independent of the physics process or energy scale. First, any remaining gluons in the event are non-perturbatively split into quark-antiquark pairs. These then form colour-singlets with other quarks in the event. The colour-singlets form clusters which can be thought of as highly excited hadron resonances. These high mass resonance/clusters decay into lighter states and stable hadrons. Occasionally, the original clusters are too heavy to decay directly into hadrons. When this happens, a $q\bar{q}$ pair is created from the vacuum and forms two new clusters with the original partons from the heavy cluster. Once all clusters are light enough for a two-body decay into hadrons to be a good description, the clusters are decayed into hadrons. Unfortunately, through the process of forming the clusters and their decay, the spin information of the partons is washed out. As such, the cluster decay is entirely based on available phase space.

It is generally accepted that the string model is the better approach for hadronisation, as it handles the non-perturbative effects in a theoretically consistent way. However, the problem is that it is too successful; it can hide flaws in the perturbative part of the MC simulation. This represents the different approaches between the different Monte Carlo groups. Those that use cluster models assume that as long as the perturbative part it done correctly, then any hadronisation model will do. String enthusiasts assume that because hadronisation is non-perturbative, non-perturbative motivated methods need to be used. As more data has become available to distinguish the two methods, cluster based methods have become more 'string-like' and groups who use string methods have corrected their perturbative methods. For example, the Pythia group incorporated angular ordering into their parton shower and the Herwig group introduced the stage where heavy clusters split into lighter colour-connected clusters.

4.4.4. Underlying Event

Out of all the parts of the Monte Carlo simulation, the modelling of the underlying event is the least developed. This part of the simulation deals with what happens to remnants of the protons after the initial parton-parton collision and its evolution. As the cross-section for soft interactions is larger than the total proton-proton cross-section, a key part of the underlying event is the modelling of multiple parton

interactions (MPI). The simplest models for this can be thought of a repetition of the primary proton-proton collision, each time removing the energy of the partons involved in the collision from the proton. This sequence is repeated until the energy of the proton goes below some defined minimum. The additional soft-collisions effect on the event can, naïvely, be thought of as a uniform addition of low energy particles in rapidity space.

4.4.5. POWHEG and MC@NLO

Historically, NLO theoretical predictions for different process have been available at fixed order, for example two incoming partons interact to form 3 outgoing partons. If non-perturbative effects, such as hadronisation, want to be included then a parton shower needs to be applied. As the parton shower itself introduces higher order corrections, when applying a parton shower directly to a fixed order calculation many terms are double counted.

Currently, NLO is the state-of-the-art for MC event simulation of $b\bar{b}$ production. There are two primary MC generators that are used, POWHEG [55–58] and MC@NLO [59, 60]. MC@NLO was the first NLO accurate parton shower MC to overcome the issues of double counting NLO terms in the parton shower. It does this by deriving the NLO terms in the parton shower, and adding subtraction terms into the matrix element to cancel these out. These cancelations lead to some undesirable effects such as MC@NLO events being linked to a specific parton shower. The subtraction terms need to be calculated by hand and implemented into the MC@NLO code. This means events generated for one parton shower cannot be used by another. The second drawback is that MC@NLO events can have negative weights. The POWHEG (POsitive Weight Hard Event Generator) overcomes these drawbacks. In principle, POWHEG generates only positive weighted events that can be showered with any parton shower. However, in practice there are subtleties that mean POWHEG does not work quite as advertised (e.g. it can generate negative weighted events). However, the impracticalities with both these generators are far outweighed by the increased accuracy they provide in physics modelling.

While both POWHEG and MC@NLO are accurate to NLO, they differ in their treatment of higher order terms. Such higher order effects are particularly important in $b\bar{b}$ production, and large differences are seen when looking in the dijet system. The specifics of these differences will be discussed in the analysis chapters of this thesis. The differences between the POWHEG and MC@NLO approaches mostly come from the later emissions after the NLO emission [58]. For instance, POWHEG treats the progression from the energy of the hard process to the energy of emission with its own method, while MC@NLO makes use of the method used by the parton shower it's linked too. As POWHEG uses its own method, the coupling associated with the POWHEG emission is evaluated at the p_{T} of the emission. While this is

true for some types of MC@NLO events, in events where MC@NLO adds a real NLO emission, the coupling is evaluated at the hard scale.

4.4.6. Simulation of $b\bar{b}$ Production in MC

Simulating $b\bar{b}$ production is challenging from a perturbative calculation point of view. Bottom production cross-sections are characterised by a fairly large value of the strong coupling constant, leading to sizeable higher order corrections [60]. All three production processes described in Sect. 2.2.3 must be considered, each has different kinematic signatures and hence dominating in different regions of phase space. Leading-order parton shower MC can take into account FCR in the matrix element and to a certain extent, FEX. However, GSP and the second b-quark in FEX require the parton shower to create them. Generating GSP events in the parton shower is very inefficient, as it requires generating general QCD events and hoping a gluon decays into two b-quarks. This inefficiency can mean areas of phase space dominated by gluon splitting being under populated. Another issue is that splitting of one hard parton into two well separated hard partons is outside the strict validity of most parton shower models. Thus, the kinematics of the event may not be as well described as if the entire process was calculated in a NLO matrix element.

Chapter 5.

Measurement of the inclusive and dijet cross-sections of b-jets in pp collisions at $\sqrt{s} = 7\,\text{TeV}$ with the ATLAS detector

This chapter focuses on the inclusive b-jet cross-section analysis as discussed in [8]. However, all measured distributions are discussed as Sect. 5.5 covers all the theory comparisons shown in the publication. The study of b-quark production at the LHC provides an interesting test of pQCD and allows the modelling of b-quark production in Monte Carlo simulation to be tested. This is important, as the b-quarks from QCD are a large background to many new physics searches. The measurement was made using the dataset collected in the 2010 running period of the ATLAS detector, corresponding to $34\,\text{pb}^{-1}$ of integrated luminosity. Jets are reconstructed using the anti-k_t algorithm with a distance parameter $\text{R} = 0.4$. An enriched sample of b-jets is selected by looking for a displaced vertex, identified by the SV0 b-tagging algorithm. The fraction of jets containing a b-hadron is extracted using a fit to the invariant mass of the tracks coming from the secondary vertex. The inclusive cross-section is measured as a function of jet p_{T}, in the range 20–400 GeV, and rapidity, in the range $0 < |y| < 2.1$. The rapidity range was chosen so the jets are fully contained within the inner detectors of ATLAS. The binning was chosen such that the bin boundaries in p_{T} were at least twice the jet energy resolution and the $|y|$ bin edges avoid boundary regions between the calorimeters. The bin boundaries are as follows:

p_{T} [GeV] :	[20, 40, 60, 80, 110, 160, 210, 260, 310, 400]
$\lvert y\rvert$:	[0.0, 0.3, 0.8, 1.2, 2.1]

In the region $30 < p_{\text{T}} < 140\,\text{GeV}$, a muon-based b-tagging method is used to provide a complementary, and largely independent, cross-section measurement as a function of jet p_{T}.

The $b\bar{b}$ dijet cross-sections are measured for the leading and sub-leading jet in the event, for jets with $p_{\mathrm{T}} > 40\,\mathrm{GeV}$ and $|y| < 2.1$. They are measured with respect to invariant mass, $110 < \mathrm{m}_{jj} < 760\,\mathrm{GeV}$, the azimuthal angle between the two jets, $\Delta\phi$, and the angular variable χ, where χ is given in equation 5.1:

$$\chi = e^{|y_1 - y_2|}. \tag{5.1}$$

Additional constraints are placed for the measurement of the χ distribution. All events must have $y_B < 1.1$, where y_B is defined in equation 5.2 and is called the 'boost' variable. This restriction is applied to reduce the sensitivity to uncertainties from the PDFs description of small x regions. The χ variable is defined such that the cross-section of 2→2 elastic scattering of point-like massless particles is approximately constant as a function of χ.

$$|y_B| = \frac{1}{2}|y_1 + y_2| \tag{5.2}$$

5.1. Event Selection and Trigger

Events were selected from $34\,\mathrm{pb}^{-1}$ of 7 TeV data [61, 62]. Only events which were recorded during optimal running of the ATLAS detector were used; this is decided by the inner detector, calorimeters and muon system all meeting certain data quality criteria. As *b*-tagging requires an accurate measurement of the primary vertex, only events with a primary vertex containing at least 10 tracks with $p_{\mathrm{T}} > 150\,\mathrm{MeV}$ are accepted. Further to this, the event must pass a p_{T} dependent trigger, which are listed in Table 5.1. The data recorded during the 2010 run was used to calibrate trigger systems. As such, different triggers are used for the first and second half of the data-taking period. The data is split into smaller sets, known as periods and labeled alphabetically. Each period represents a set of stable beam conditions. During periods A to F, only the L1 triggers were active. For periods G to I, the EF triggers were being calibrated so events were only rejected at L1 and L2.

Trigger Efficiency

A trigger accepts an event if it meets certain criteria. For single jet triggers, an event is expected to be accepted if a single jet within the η range of the trigger has an E_{T} greater than the threshold. However, due to resolution effects and mismeasurements, the needed E_{T} for the trigger to be ∼100% efficient may be higher than the stated threshold. Trigger inefficiencies need to be corrected for to ensure they do not bias the final result.

p_{T} range [GeV]	Trigger Used		Luminosity [pb^{-1}]
	Periods A-F	Periods G-I	
20–40	L1_MBTS_1 (A-C), EF_mb_M1_eff (D), EF_mbMbts_1_eff (E-I)		10.1×10^{-4}
40–60	L1_J5	EF_j20_jetNoEF	3.2×10^{-2}
60–80	L1_J10	EF_j20_jetNoEF	1.1×10^{-1}
80–110	L1_J15	EF_j35_jetNoEF	5.7×10^{-1}
110–160	L1_J30	EF_j50_jetNoEF	2.2
160–210	L1_J55	EF_j75_jetNoEF	8.9
210–260	L1_J75	L1_J95	33.9
260–310	L1_J95	L1_J95	33.9
310–400	L1_J95	L1_J95	33.9

Table 5.1.: Triggers used for a given run period and p_{T} bin in the 2010 inclusive b-jet cross-section. The jet trigger names follow the convention X_Y_Z, where X refers the trigger level, Y refers the E_{T} threshold to fire the trigger, and Z refers to any additional information about the trigger. In this case, for the EF triggers, Z tells us that the EF filter wasn't active and it was only the L2 trigger that was rejecting events. The triggers used for the 20–40 GeV bin are triggers designed to accept an inclusive sample of events.

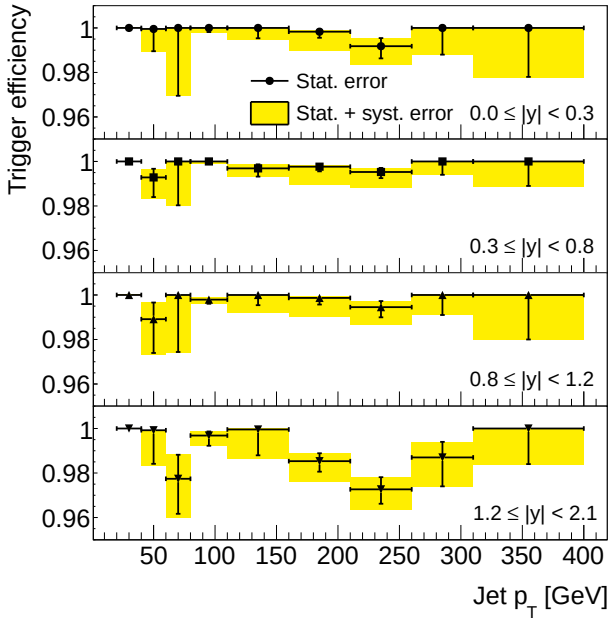

Figure 5.1.: Trigger efficiencies for the inclusive *b*-jet cross-section measurement.

Each bin in the analysis uses a different trigger in order to maximise the number of events in it. In order to avoid complications in the phase space where the trigger is not fully efficient, known as the 'turn-on' region, triggers are only used when they are close to 100% efficient. The trigger efficiency can be found by comparing the trigger of interest to an unbiased sample of events. The efficiency can then be measured by seeing what percentage of events for a given area of phase space are accepted by the trigger. An unbiased sample can be obtained using events from the minimum bias trigger stream, as the name suggests this trigger accepts events with as little experimental bias as possible. It has been shown for jet events, that the minimum-bias trigger is effectively unbiased [63]. Using this event sample, the lowest threshold jet trigger efficiencies are calculated. However, the events from the minimum bias trigger are mostly low energy events, so do not reach high enough in E_{T} to be used for higher E_{T} jet triggers. These are evaluated using the 'boot-strap' method. The minimum bias sample is used for the lowest E_{T} jet trigger; then, in the region where the low E_{T} trigger is 100% efficient, a higher E_{T} jet trigger is evaluated. Using this method, the efficiency of all the triggers can be measured. The important result for the analysis, is the overall trigger efficiency in a given bin, shown in Fig. 5.1. In order to combine the different triggers used for a single bin, a luminosity-weighted average is taken of the two. The trigger efficiency is above 97% for all regions and typically closer to 100%. The trigger efficiency predicted by the MC are consistent with the data-driven results.

Jet Selection

Jets are reconstructed using the anti-k_t algorithm with a distance parameter $R = 0.4$. Jets are accepted into the analysis if they have $20 < p_{\text{T}} < 400\,\text{GeV}$ and $0 < |y| < 2.1$. In order to avoid accepting jets produced from poorly calibrated parts of the detector or electronic noise, all jets must pass certain quality criteria [64]. As a pre-*b*-tagging criteria, all jets much contain at least one track that passes the SV0 track quality cuts, as listed in Table 4.1. In addition to the standard jet calibration, described in Sect. 4.1.2, an additional semi-leptonic correction is applied to all jets with a muon with $p_{\text{T}} > 5\,\text{GeV}$ and within $\Delta R < 0.5$ of the jet-axis. This is designed to correct for energy lost when the *b*-hadron decay produces a muon and neutrino. The correction adds the muon four-vector to the jet and corrects for the neutrino missing energy. The neutrino correction is an average correction derived from MC simulation. The effect of this correction can be seen in Fig. 5.2. While still not perfect, the reconstructed energy of the jet becomes much closer to the true value after the correction is applied. The remaining difference between the detector- and particle-jets are due to the correction being derived from an independent MC event sample, thus statistical fluctuations and other sample differences will affect the closure. As the residual differences between detector- and particle-jets are corrected for in the unfolding, the corrections was not re- derived for the primary MC sample. No such correction is applied for electrons, as identifying electrons within jets is difficult. However, only the neutrino energy is lost as the electron energy is deposited in the calorimeter. The combined efficiency of the event reconstruction and quality requirements was found to be above 96% for *b*-jets.

The SV0 algorithm is used to create a *b*-jet enriched sample of jets. Only jets that have a SV0 weight > 5.85 are used in the analysis. This is a standard working point for the SV0 algorithm, for which data/MC scaling factors were derived, and corresponds to a 50% *b*-jet tagging efficiency with a light-jet mistag rate of about 0.5%.

Simulated Datasets

Samples of simulated dijet events from proton-proton collisions at $\sqrt{s} = 7\,\text{TeV}$ were produced with the Pythia 6.423 [65] event generator. The events were generated using the MSRT LO* [24, 66] PDFs and a set of tuned parameters that reproduce available data, these are listed in [67]. The events were then passed through a full simulation of the ATLAS detector [68] based on Geant 4 [69]. The result of the full simulation is the expected detector response to the physics signals from the MC generator. This is then passed through the same reconstruction software that is used on data.

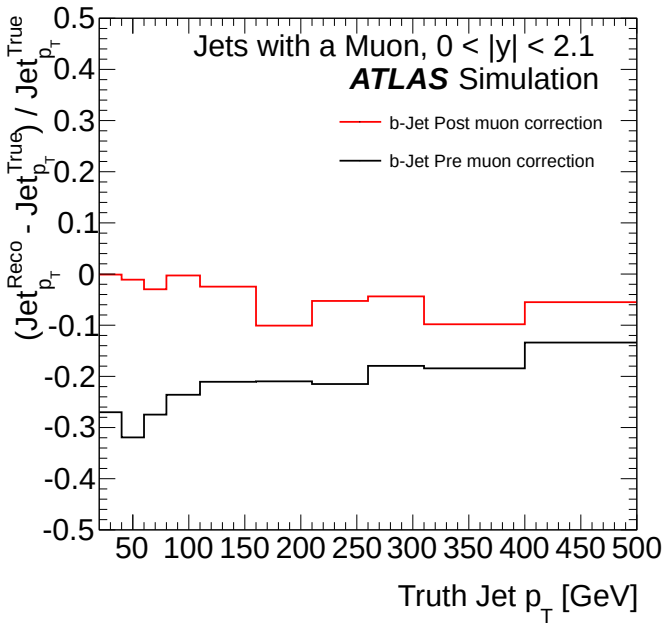

Figure 5.2.: Effect of the semi-leptonic correction in MC simulation.

5.2. b-tagging Efficiency

Algorithms that identify jets originating from b-quarks look for typical features of b-jets, conversely, b-jets with atypical features are not identified. The b-tagging efficiency can be calculated from the MC by taking the ratio of all b-labelled jets and the b-labelled jets which are also b-tagged, where b-labelling is described in Sect. 4.2. Using the independent b-tagging techniques, data driven efficiencies can be calculated as was done in [52]. This leads to p_{T} dependent scale factors to correct differences between data and MC simulation, as described in Sect. 4.2.4. The values for the b-tagging efficiency, as shown in Fig. 5.3, are then used to correct the measured data.

5.3. Purity Fit

A binned likelihood fit is used to derive the number of jets containing b-hadrons from the SV0 tagged jet sample. Templates, derived from MC, of the secondary vertex mass for the different jet flavours are fitted to the data. This fit is preformed for each bin in the analysis by minimising a log-likelihood function which takes into account the statistical error on the data and MC. In order to avoid biasing the error, the number of b-, c- and light jets are obtained without using additional constraints. The binning of the vertex mass is chosen such that at least one bin exceeds 100 entries in

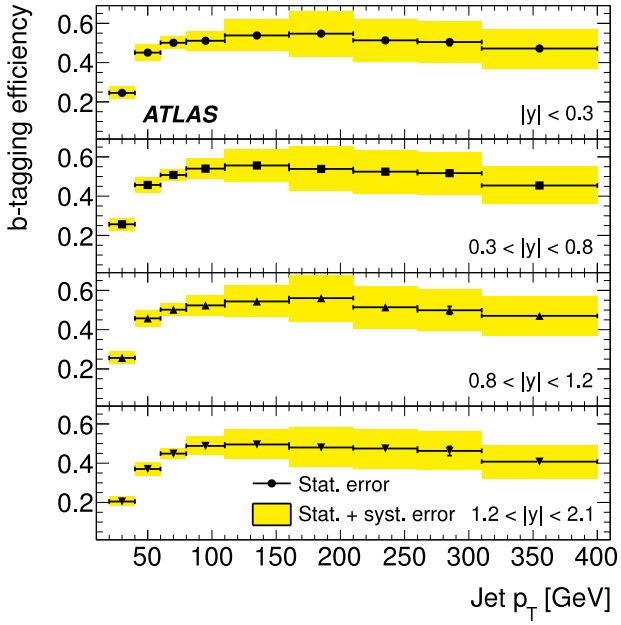

Figure 5.3.: The b-tagging efficiency for b-jets tagged with the SV0 algorithm in bins of p_{T} and y. Systematic uncertainties include the calibration uncertainty associated with the b-tagging scale factors.

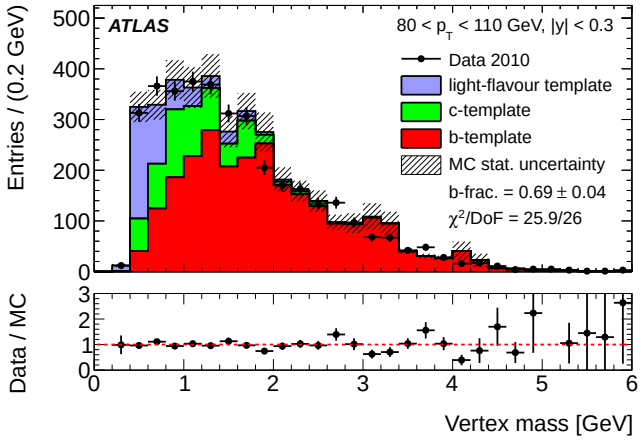

Figure 5.4.: Example purity fit of the inclusive b-jet cross-section.

data, with a minimum bin size of 200 MeV. If the fit does not converge or is unstable, then the bin size is increased by steps of 50 MeV until the fit is stable. Examples of instability are negative values for the number of jets from a flavour template or different final values when using different starting values. An example of a purity fit can be seen in Fig. 5.4.

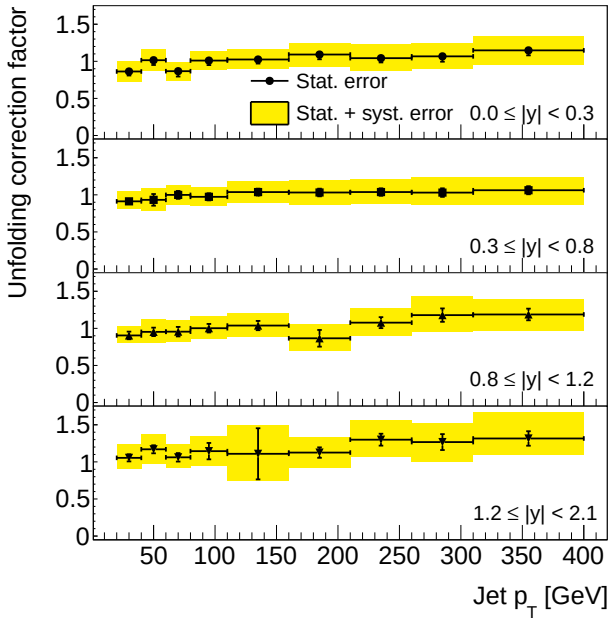

Figure 5.5.: Unfolding correction factors applied to the inclusive *b*-jet cross-section.

5.4. Unfolding

As discussed in Sect. 4.3, to compare the data to theory predictions, the detector level results need to be unfolded to particle level. For this analysis, this is done using a bin-by-bin unfolding method. This is a comparatively straightforward unfolding method, but is suitable for early analyses that have comparatively large bin widths. The bin size is important, as the migration of events from one bin to another is the main effect the unfolding corrects for. By requiring bins to be at least two times the jet p_{T} resolution, bin migration can be minimised. Bin migration for the inclusive *b*-jet cross-section is predominantly due to the steeply falling p_{T} spectrum. More jets will migrate from a higher p_{T} bin, due to the intrinsic jet energy resolution, than will migrate the other way.

The Pythia dijet samples described in Sect. 5.1 are used to calculate the unfolding correction factors. This is done by taking the ratio of *b*-labelled particle jets and *b*-labelled reconstructed jets. The results can be seen in Fig. 5.5. The first thing to note is that the majority of values are above one; this is unexpected when only considering bin migration. However, the unfolding is correcting the detector level jets back to particle jets that contain neutrinos and muons. While a semi-leptonic correction is applied for muons to detector level jets, neutrinos associated with electrons still need to be corrected for.

5.5. Theory

Currently the most advanced theory predictions for b-quark production come from the NLO generators POWHEG and MC@NLO interfaced with parton showers. Events generated with MC@NLO are tailored for a specific parton shower. For the case of $b\bar{b}$ production only Herwig 6 can be used. For this analysis, MC@NLO 3.42 with the MSTW2008nlo [24] PDFs was showered with Herwig 6.510. The POWHEG-hvq module within the POWHEG-BOX framework is used to generate events using the MSTW2008nlo PDFs as well. As long as the parton shower does not produce a harder emission then POWHEG, events generated with POWHEG-BOX can be showered with any parton shower. Events produced from POWHEG were showered with Pythia 6.423 and Herwig 6.510 for this analysis.

5.5.1. Motivation for Theoretical Uncertainties

POWHEG was chosen as the generator to investigate the theoretical uncertainties. The source of the theoretical uncertainties can be understood by examining the equation for a generic cross-section, a simplified version of equation 2.8 is expressed in equation 5.3.

$$\sigma = \sum_a \sum_b \overbrace{f_{a/A}(x_a, \mu_F^2) f_{b/B}(x_b, \mu_F^2)}^{PDFs} \underbrace{\left[\sigma_{LO} + \alpha_{\mathrm{S}}(\mu_R)\sigma_{NLO} + ...\right]}_{HardScatter}. \tag{5.3}$$

The uncertainty comes in the parametrisation of the PDFs and the energy scales at which the interaction takes place, the renormalisation, μ_R, and factorisation, μ_F, scales.

Scale Variation

The scales μ_R and μ_F represent the energy scales of the parton collision; where μ_R is the scale at which α_{S} is calculated and μ_F is the scale at which the PDFs are sampled. Having these scales explicitly in the cross-section equation is a side-effect of only being able to calculate pQCD to a certain order. If pQCD could be calculated to all orders, these terms would disappear. Assuming enough physics is contained within the prediction, varying these values can give an idea of the effect of missing higher order terms.

In the POWHEG-BOX hvq module, μ_F and μ_R are chosen to be equal to the transverse mass of the heavy quarks in their rest frame, given by equation 5.4:

$$\mu_F = \mu_R = m_{\mathrm{T}} = \sqrt{m^2 + p_{\mathrm{T}}^2}. \tag{5.4}$$

Any value of the same order for μ_R and μ_F is also theoretically justifiable. To evaluate the uncertainty in the freedom of the scale choice, the nominal value for μ_R and μ_F were varied up and down independently by a factor of two. The factor of two was chosen because of historical convention; as mentioned earlier, any value of a similar order to the nominal value is defendable. The largest source of uncertainty came from the renormalisation scale variation, implying that b-quark production has large higher order corrections.

PDF Variation

There is currently no method to calculate the proton's PDFs using purely theoretical means. When creating the PDFs, different groups use the available data and certain assumptions to derive their best predictions. However, different groups use different assumptions, resulting in different answers. By taking the envelope of different PDFs, an attempt can be made to evaluate the known uncertainty on the values. For this analysis the following PDFs were used: NNPDF 2.1 [26], CT10 [22] and MSTW2008nlo. These PDFs were chosen because they were fitted using all available data. Other PDFs only use selective datasets.

5.5.2. Difference between the NLO Generators

POWHEG and MC@NLO are both accurate to NLO; however, higher order terms are treated differently. This can lead to substantial differences between the two generators. The differences are discussed in the POWHEG heavy quark production introductory paper [58] and are attributed to the perturbative corrections for low-mass quarks being significant. Figure 5.6 shows the ratios of POWHEG, showered with Herwig 6, and MC@NLO, showered with Herwig 6, with respect to POWHEG showered with Pythia 6. These plots show two interesting features: first, there is a distinct shape difference when POWHEG is interfaced with different parton showers. Secondly, there is a significant difference between MC@NLO and POWHEG. The difference between the different parton showers is unexpected, as the differences between Pythia 6 and Herwig 6 were expected to be small. This effect is seen in all jet distributions produced from POWHEG, and at the time of writing is not properly understood. However, the difference between two showers is not enough to explain the shape difference seen between POWHEG and MC@NLO. There appears to be a rapidity dependence in MC@NLO not seen in POWHEG, this is confirmed

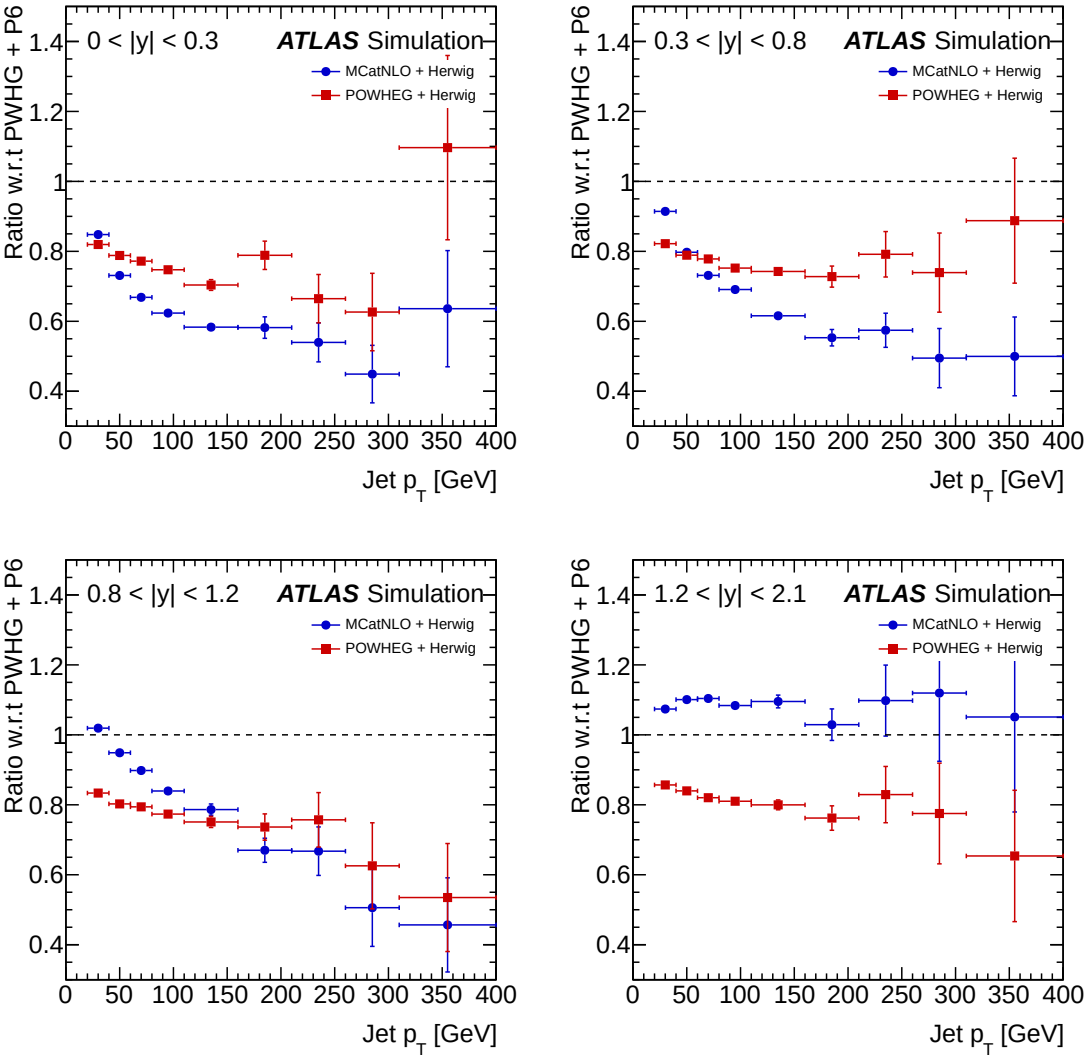

Figure 5.6.: Ratio of POWHEG+Herwig 6 and MC@NLO+Herwig 6 with respect to POWHEG+Pythia 6.

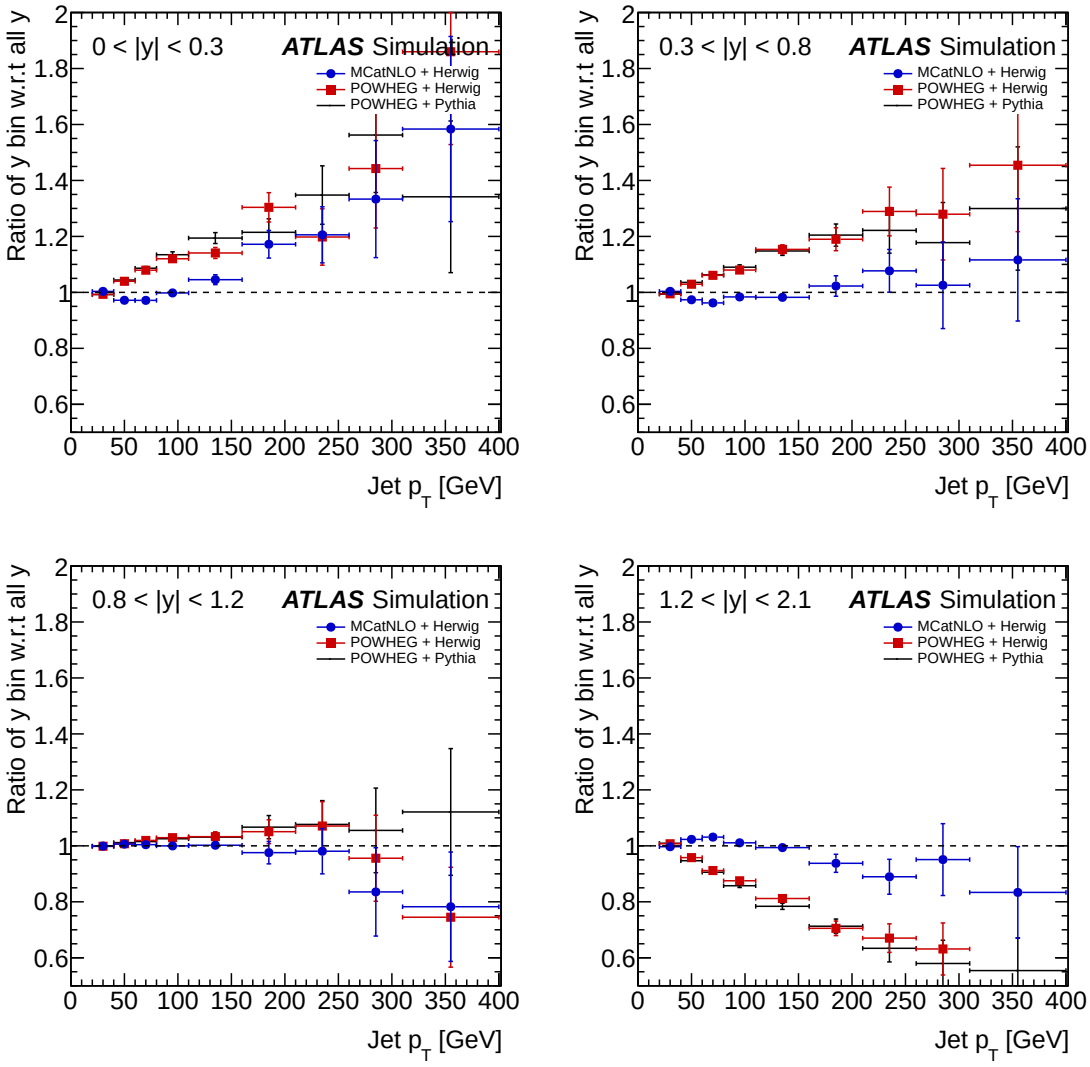

Figure 5.7.: Ratio of NLO predictions for each $|y|$ bin with respect to all $|y|$

in Fig. 5.7. It can be seen that the y dependence in POWHEG is not effected by the parton shower, but comes from the matrix element.

5.6. Systematics

Uncertainties on an experimental measurement can be put into one of two categories, statistical and systematic. Statistical errors represent the significance of the number of events in the measurement, while systematic uncertainties are a catch-all term to bracket our lack of knowledge of certain areas. In many cases, the known unknowns

Source of syst. uncertainty	Uncertainty [%]
Jet Energy Scale/Resolution	10 – 20
b-tagging efficiency	5 – 20
b-jet purity fit	3 – 8
Luminosity	3.4
Other sources	2

Table 5.2.: Summary of the most important systematic uncertainties on the inclusive *b*-jet cross-section.

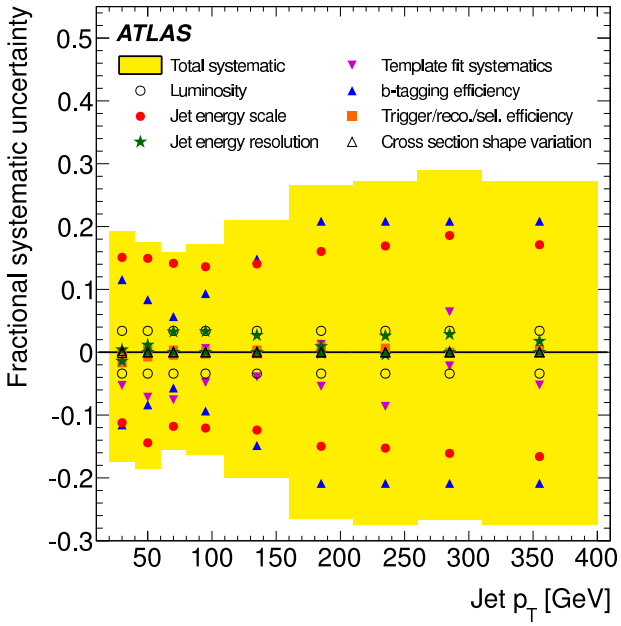

Figure 5.8.: Summary plot of the fractional size of systematic uncertainties from different sources. The total systematic uncertainty is derived by adding the individual sources of uncertainty in quadrature.

can be constrained and quantified quite accurately. For others, conservative estimates can be given for the uncertainty introduced because of the missing information. The systematic uncertainties considered in this analysis are shown in Fig. 5.8 and summarised in Table 5.2. The dominant systematic uncertainties come from the *b*-jet energy scale calibration and determination of the *b*-tagging efficiency and purity.

5.6.1. Jet Energy Scale and Resolution

The jet energy scale (JES) is commonly one of the largest systematic uncertainties in any analysis involving jets. This accounts for the uncertainty on the overall calibration of the detector, representing the accuracy that the measured jet energy corresponds to the actual energy of the jet. A change in the jet energy scale would shift the jet energy the same amount for all jets. This is not to be confused with the jet energy resolution, which represents the inherent inaccuracy in the detector and will shift the measured jet energy randomly around some true value. The resulting JES uncertainty varies from between 2% and 6% percent depending on the jet p_{T} and rapidity region. Dealing with b-jets introduces additional JES uncertainty, although their response is similar to inclusive jets. To account for this, an additional 2.5% uncertainty is added in quadrature to the standard inclusive jet energy scale uncertainty. To asses the jet energy scale uncertainty, the p_{T} of jets measured in data were shifted up and down by one standard deviation (σ) of the uncertainty. When propagated through to the cross-section, this leads to an uncertainty between 10% and 20%.

As MC simulation played a large role in this analysis, differences between data and MC need to be evaluated. The jet energy resolution was determined in both data and simulation, and it was found that the MC has a slightly better resolution. To account for any effects this may have, the jets in the MC were smeared by additional factors, based on their p_{T} and η, to give the same effective resolution in data and MC. The difference between the smeared and nominal measurements was taken as the systematic uncertainty.

5.6.2. *b*-tagging Efficiency

When calculating the b-tagging efficiency, the uncertainty on the b-tagging scale factor are evaluated. As discussed in Sect. 4.2.4, the accuracy of the scale factor are a significant source of uncertainty. The uncertainty primarily comes from high p_{T} b-jets ($> 140\,\text{GeV}$) which are not constrained by data-driven methods.

5.6.3. Shape Dependencies on Unfolding

An implicit assumption of the unfolding is that any shape difference between the MC and nature will make little difference in the unfolding factors. This can be evaluated by modifying the shape of the jet p_{T} distribution, which is done by re-weighting events based on the p_{T} of their leading jet. The equation for the weights is given by

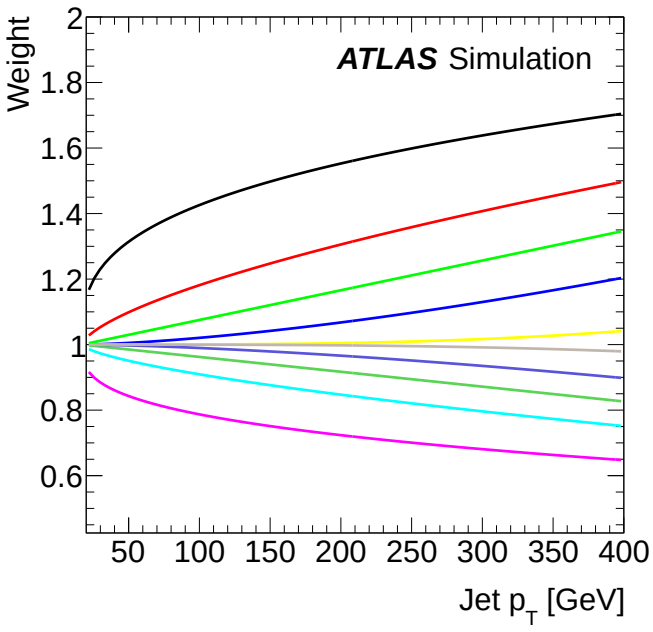

Figure 5.9.: Functions used to evaluate the shape dependence in the unfolding.

equation 5.5, and the values are shown in Fig. 5.9.

$$W = 1 + A \times \left(\frac{Jet_{p_{\mathrm{T}}} - 17}{1103} \right)^{B} . \tag{5.5}$$

In the above, the values used for the parameters A and B were $A = 1$ or -0.5 and $B = 0.33$, 0.66, 1, 1.5 or 3. This weighting function is, to a large extent, arbitrary, but should give an estimate of the effect of a different underlying shape. It was found that the re-weighting had less than a 1% difference on all bins in the analysis.

5.7. Results

The double-differential inclusive b-jet cross-section is shown in Fig. 5.10 and the single differential inclusive b-jet cross-section, with the muon based measurement, is shown in Fig. 5.11. Figure 5.11 shows the life-time based b-tagging analysis on the same plot as the, largely independent, muon based b-tagging measurement for the rapidity region $0 < |y| < 2.1$. A broad agreement can be seen between the two measurements. Figure 5.10 shows the lifetime-based b-tagging measurement for the four different measured rapidity regions. Here, the comparisons with theoretical predictions can be seen more clearly. For the purposes of a shape comparison to data, Pythia 6 is scaled by a factor of 0.67. As the predictions are only accurate to

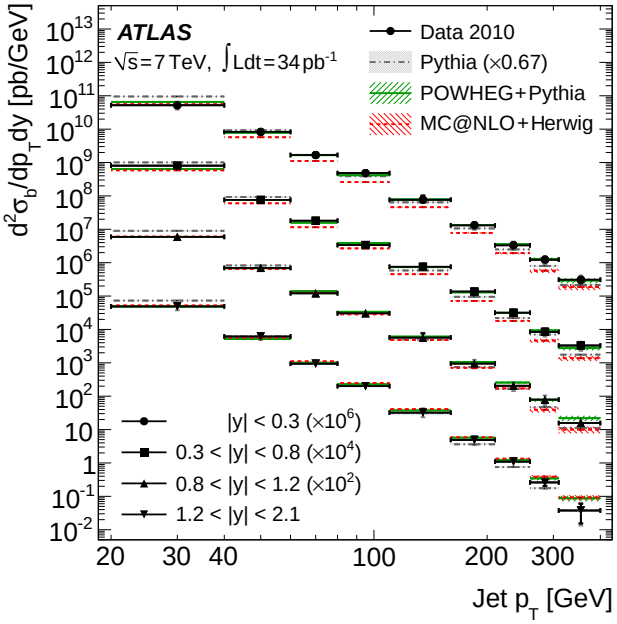

Figure 5.10.: Double-differential inclusive b-jet cross-section with respect to p_{T} and y.

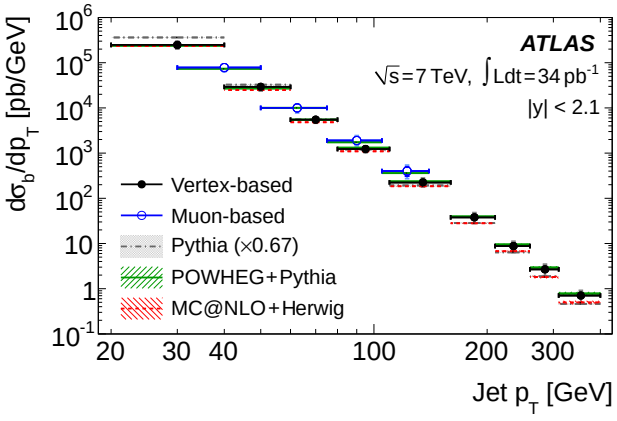

Figure 5.11.: Single differential inclusive b-jet cross-section with respect to p_{T}. Showing the muon- and lifetime based b-tagging analyses.

leading-order in pQCD, Pythia 6 is not expected to get the normalisation right. The overall agreement between the data and different MC is good.

This can be further examined in the ratio plots, figures 5.12 and 5.13. These plots show the ratio between data and POWHEG and MC@NLO, with the top panel showing the ratio over the full rapidity range. POWHEG provides a better description of the inclusive b-jet cross-section across all rapidity regions, while MC@NLO under-

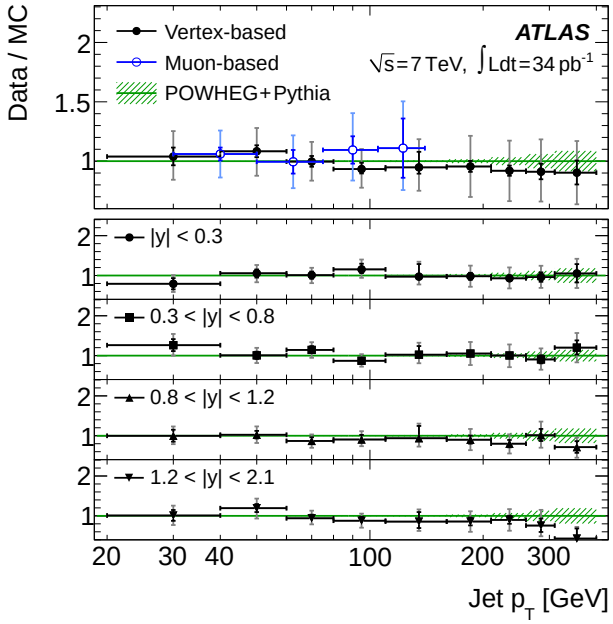

Figure 5.12.: Ratio of the inclusive b-jet measurement with the POWHEG+Pythia 6 prediction. POWHEG+Pythia 6 error band derived from statistical uncertainty only.

predicts the rate of b-jets at low rapidity. As discussed in Sect. 5.5.2, this behaviour appears to be primarily from differences in the POWHEG and MC@NLO matrix elements, although, it is possible that some of the normalisation effect could be from the Herwig 6 parton shower used by MC@NLO. Looking at the top panel in these two plots it is worth noting the good agreement between the two analysis methods. This gives further confidence that the measurements are correct. Figure 5.14 shows the ratio of Pythia 6 and data. It can be seen that there is a notable shape difference between data and Pythia 6.

The $b\bar{b}$ dijet measurements can be seen in figures 5.15, 5.16 and 5.17. The first thing to note, is the general agreement between all theoretical predictions and data. Often, POWHEG+Pythia 6 and MC@NLO+Herwig 6 bracket the measured value. This is particularly evident in Fig. 5.15, the dijet mass spectrum. Here, POWHEG+Pythia 6 tends to be a little low, while MC@NLO+Herwig 6 is a little high. Pythia 6 is scaled differently than in the inclusive b-jet measurement, which is not surprising given the differences in event selection between the inclusive b-jet analysis and the $b\bar{b}$ analysis. The requirement that the leading and sub-leading jets in the event both be b-tagged biases the event sample away from those where the b-jets are produced via gluon splitting. Thus, higher order production mechanisms, that are present in the inclusive analysis, are suppressed. No scaling is applied in the angular variables as these measurements are normalised to the number of events

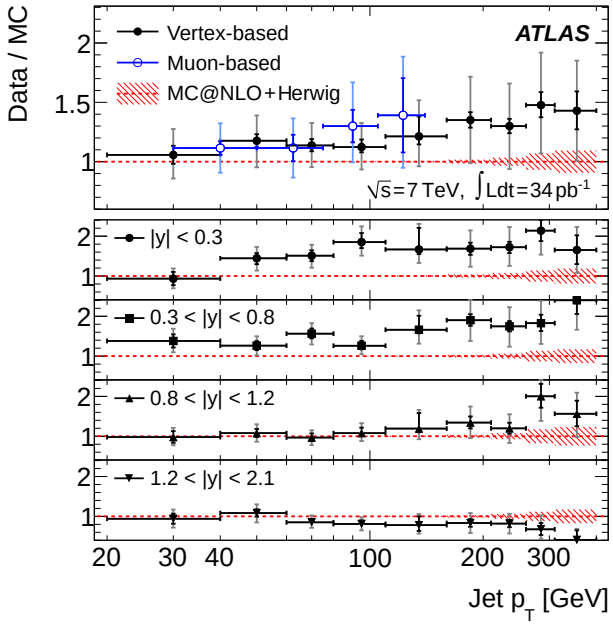

Figure 5.13.: Ratio of the inclusive b-jet measurement with the MC@NLO+Herwig 6 prediction. MC@NLO+Herwig 6 error band derived from statistical uncertainty only.

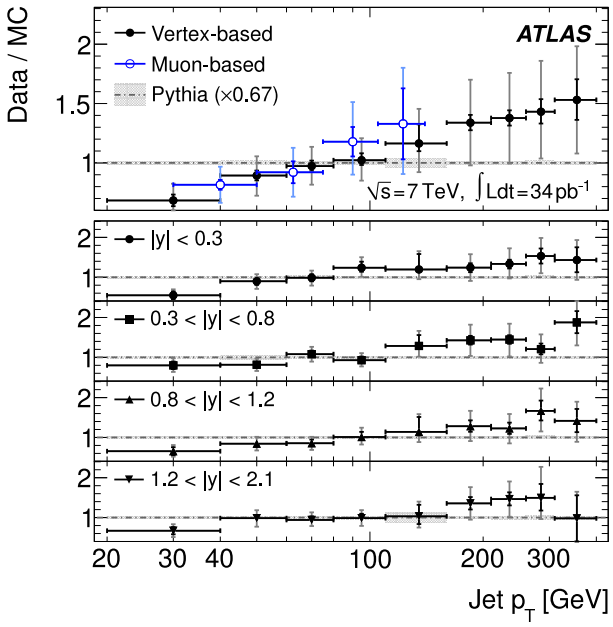

Figure 5.14.: Ratio of the inclusive b-jet measurement with the Pythia 6 prediction. Pythia 6 error derived from statistical uncertainty only.

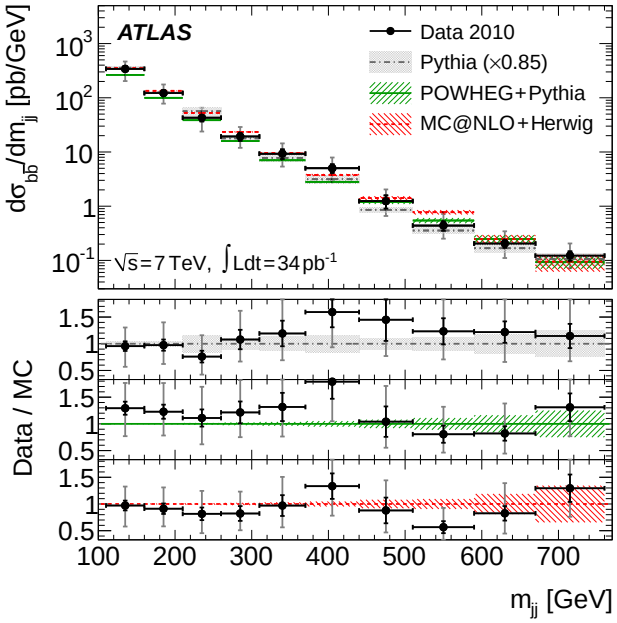

Figure 5.15.: Dijet mass cross-section measurement compared to the POWHEG+Pythia 6, MC@NLO+Herwig 6 and Pythia 6 predictions. Theory error band derived from statistical uncertainty only.

in the distributions. Both NLO generators provide a good shape description of data for the angular variables.

5.8. Conclusion

The inclusive and dijet cross-sections of b-jets in pp collisions at $\sqrt{s} = 7\,\text{TeV}$ have been measured with the ATLAS detector. The independent methods to measure the inclusive cross-section provide confidence in the analysis methods used, with the presented results later being confirmed by a CMS measurement, Fig. 5.18. It is worth noting that, at the time of publishing this thesis, the CMS results are the only competing results and only cover half the phase space covered by the analysis presented here. Both POWHEG and MC@NLO both performed well in the simulation of the dijet $b\bar{b}$ cross-section, while POWHEG performed better in modelling the inclusive b-jet cross-section.

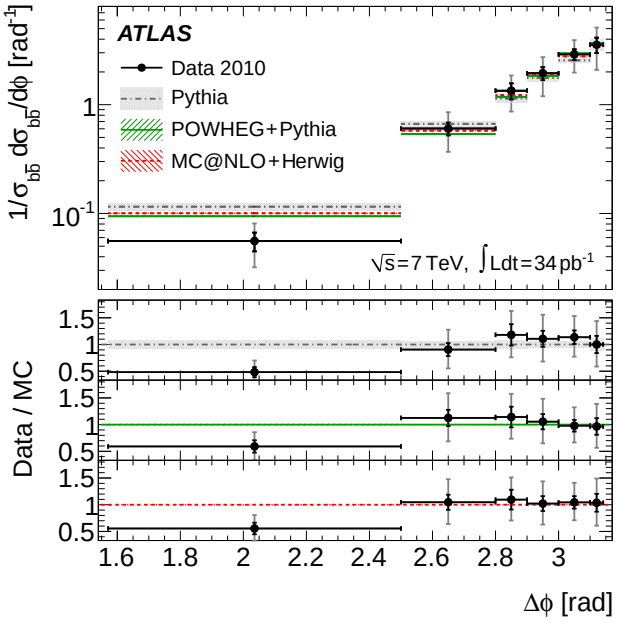

Figure 5.16.: Dijet $\Delta\phi$ cross-section measurement compared to the POWHEG+Pythia 6, MC@NLO+Herwig 6 and Pythia 6 predictions. Theory error band derived from statistical uncertainty only.

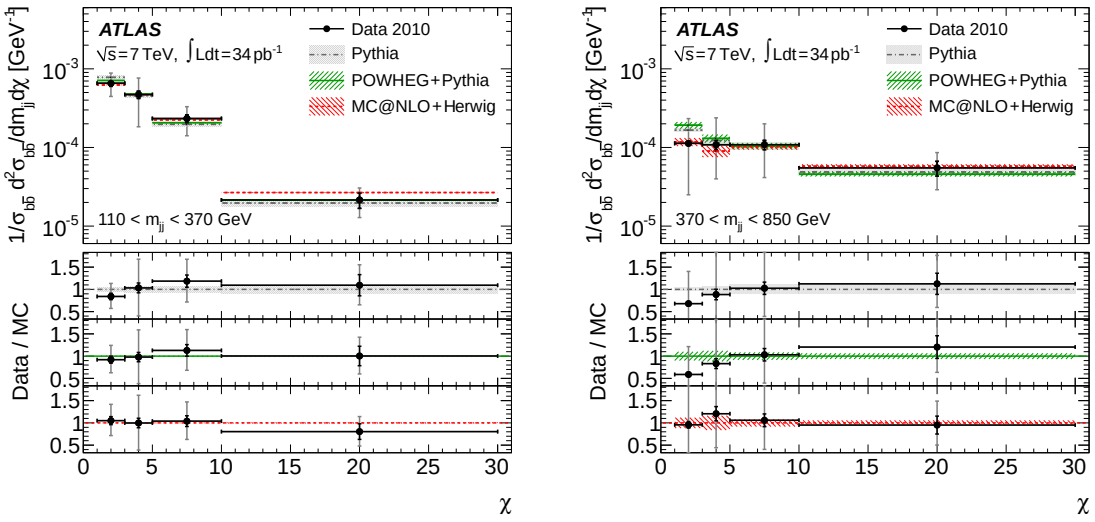

(a) $110 < m_{jj} < 370$ **(b)** $370 < m_{jj} < 850$

Figure 5.17.: Dijet χ cross-section measurements compared to the POWHEG+Pythia 6, MC@NLO+Herwig 6 and Pythia 6 predictions. Theory error band derived from statistical uncertainty only.

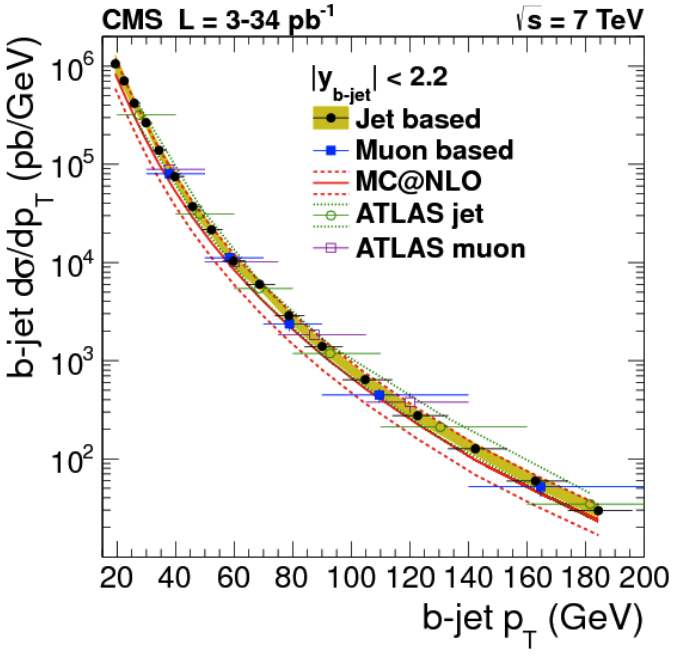

Figure 5.18.: CMS measurement of the inclusive b-jet cross-section with respect to p_{T}. Both ATLAS and CMS results are plotted [70].

Chapter 6.

Measurement of the $b\bar{b}$-dijet cross-section in pp collisions at $\sqrt{s} = 7\,\text{TeV}$ with the 2011 dataset collected by the ATLAS detector

This chapter covers the di-b-jet cross-section measurements done on the 2011 ATLAS dataset, which corresponds to a integrated luminosity of $4.31\,\text{fb}^{-1}$. This is an expansion on the 2010 analysis described in chapter 5, taking advantage of the larger event sample available to examine a broader region of phase space. The requirement of the leading and sub-leading jet in the event to be b-tagged in the 2010 analysis biases the event selection towards a back-to-back topology. Referring to the diagrams shown in Fig. 2.2, such a topology is similar to FCR-like production. This selection suppresses the affects of higher order corrections, thus providing a fairer test for LO Monte Carlo. However, with the availability of more advanced Monte Carlo generators it is important to examine the full phase space of $b\bar{b}$ production. In the analysis presented here, the only requirements of event selection are that there are two b-jets within the fiducial region of interest.

This analysis investigates a variety of variables which examine different regions of the di-b-jet phase space. Those considered are: dijet mass, m_{jj}, where $110 < m_{\text{jj}} < 1000\,\text{GeV}$; dijet p_{T}, $p_{\text{T,jj}}$, $0 < p_{\text{T,jj}} < 500\,\text{GeV}$; the azimuthal separation of the dijet system, $\Delta\phi$, $0 < \Delta\phi < \pi$; the ΔR separation of the dijet system, $0.4 < \Delta R < 4$, the χ of the dijet system, $1 < \chi < 30$ and the boost, y_{b}, $0 < y_{\text{b}} < 2.5$, where χ and y_{b} where described in chapter 5. It is worth noting that the events making up different distributions may differ, for instance events below $m_{\text{jj}} = 110\,\text{GeV}$ are included in the $p_{\text{T,jj}}$ distribution.

The dominant $b\bar{b}$ production mechanisms at lowest order are shown in Fig. 2.2. Each production mechanism tends to produce events with distinctive dijet kinematics. Thus, in some dijet variables, one production mechanism will be dominant in certain areas of phase space. In order to further understand the different behaviour, the

events can be separated into different categories which reflect the lowest order production mechanism they are most like. This is done with respect to the p_{T} ordering of the b-jets, if the leading and sub-leading jet in an event are b-tagged then the event is labelled a FCR-like event, if neither of the b-jets is the highest p_{T} jet in the event, it is labelled a GSP-like event, all other jets are labelled FEX-like events. Assigning a production mechanism based on the p_{T} ordering of the jets is not a robust physical definition, especially when considering the distinction between GSP and FEX events. However, it does provide some insight into the features observed in the cross-section as functions of different variables. In data, only FCR-like and non-FCR-like events are identified. These two event types still capture enough of the differences in the production mechanisms to be useful.

6.1. Event Selection and Trigger

Events are selected for this analysis if they are accepted by the trigger and they include at least two b-tagged jets with $p_{\mathrm{T}} > 40\,\mathrm{GeV}$ and $|\eta| < 2.5$. Events are required to come from data taking periods where the detector is running optimally and corresponds to an integrated luminosity of $4.31\,\mathrm{fb}^{-1}$. If there are more then two b-jets in the event, the two b-jets with the highest p_{T} are selected.

6.1.1. Triggers

Events are selected using the calorimeter-based single-jet triggers. To maximise the available statistics and ensure an unbiased phase space coverage of the p_{T} range from 40 GeV onwards, multiple triggers are used. The efficiencies of the different triggers were investigated to decide at which point to switch from one trigger to another. The trigger efficiency with respect to p_{T}, known as 'turn-on' curves, are shown in Fig. 6.1. The efficiency of a given trigger is defined inclusively[1], as a function of leading jet p_{T}:

$$\varepsilon(p_{\mathrm{T}}) = \frac{N(\mathrm{pass}|p_{\mathrm{T,lead}} > p_{\mathrm{T}})}{N(\mathrm{total}|p_{\mathrm{T,lead}} > p_{\mathrm{T}})}, \tag{6.1}$$

where N is the number of events. For an event to be included in the trigger turn-on calculation, it must pass the analysis selection. This is to avoid introducing inefficiencies from the differences between fully inclusive jet samples and those used in our analysis. The triggers used in the analysis are listed in Table 6.1, included in the table for each trigger is the leading jet p_{T} requirement, number of events recorded and the average prescale. The large prescales on low p_{T} triggers make it difficult to calculate the trigger turn-on points from data. This is because the trigger of interest

[1]No matching between jets and trigger regions-of-interest is performed.

must pass its own prescale, as well as that of the 100% efficient trigger it is being compared to. Due to this, low p_{T} triggers turn-on points are calculated from MC. While the triggering for event selection is done with respect to the leading jet p_{T}, the efficiencies with respect to jet p_{T} do not directly affect the measurement. The trigger efficiencies measured with respect to variables investigated in this analysis are derived directly from data. This means any mismodelling of the turn on the point in MC compared to data for the lower triggers will have little effect on the final analysis.

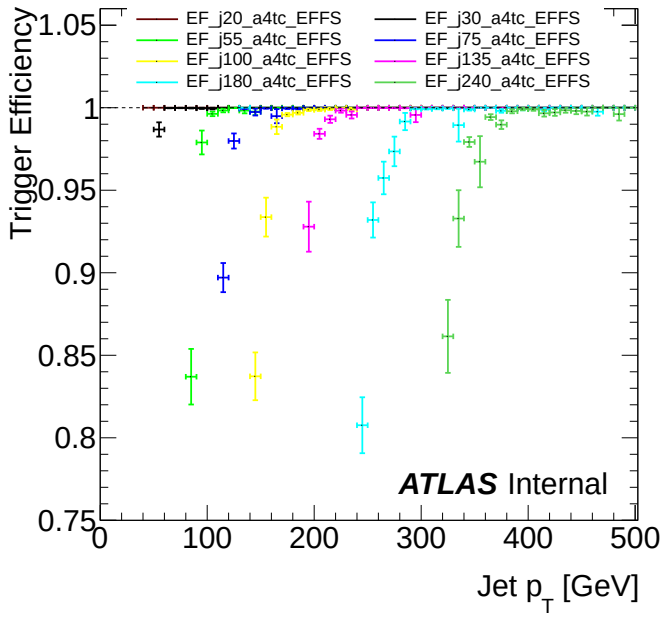

Figure 6.1.: Turn-on curves of the triggers used as a function of leading jet p_{T} at the hadronic scale.

The trigger turn-on points are calculated using the jet energies that are seen by the detector. When calculating the trigger efficiencies for the different variables in our analysis, additional corrections are made to the jet energies. These corrections include a correction for muons from semi-leptonic b-decays and additional calibration. In Fig. 6.2 the trigger efficiency for the dijet mass distribution is shown calculated for data and MC. It can be seen that the trigger efficiency predicted by the MC is consistently higher then in data. However, this is less then a 1% difference which comes from a slightly lower p_{T} turn-on point observed in MC. The trigger efficiencies for the other measured distribution can be seen in Appendix A.

Trigger	$p_{\mathrm{T,lead}}$ [GeV]	N_{events}	Avg. Prescale
EF_j20_a4tc_EFFS	$40 < p_{\mathrm{T}} < 55$	20,447	137930
EF_j30_a4tc_EFFS	$55 < p_{\mathrm{T}} < 95$	115,175	12917
EF_j55_a4tc_EFFS	$95 < p_{\mathrm{T}} < 120$	50,659	3062
EF_j75_a4tc_EFFS	$120 < p_{\mathrm{T}} < 170$	91,356	842
EF_j100_a4tc_EFFS	$170 < p_{\mathrm{T}} < 210$	55,109	244
EF_j135_a4tc_EFFS	$210 < p_{\mathrm{T}} < 270$	193,823	28.1
EF_j180_a4tc_EFFS	$270 < p_{\mathrm{T}} < 355$	465,064	3.6
EF_j240_a4tc_EFFS	$p_{\mathrm{T}} > 355$	515,575	1.0

Table 6.1.: Triggers used for each of the p_{T} slices in this analysis. The column N_{events} lists the number of events with at least 1 b-tagged jet in each slice.

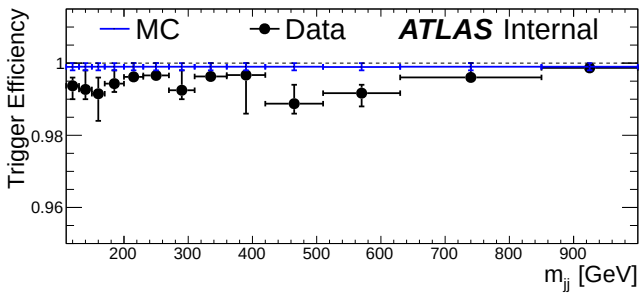

Figure 6.2.: Trigger efficiency for the dijet mass distribution.

6.1.2. Jet selection

Jets are reconstructed from energy clusters in the calorimeter using the anti-k_t algorithm with a distance parameter of $R = 0.4$. To remove jets that originated from noisy calorimeter cells or regions where the jet energy is badly measured, the jets are classified in three categories: good, bad and ugly [64,71]. Bad jets are fake jets caused by detector effects, while ugly jets are (generally low energy) jets in problematic regions such as the gap between two calorimeters. Only good jets are used in this analysis. To reject jets resulting from pile-up, the jet vertex fraction (JVF), defined as the fraction of the $\sum p_{\mathrm{T}}$ of the tracks inside the jet originating from the primary vertex, is required to be larger than 0.75. Due to the track-based b-tagging that is applied later, these selections have negligible inefficiency for the jets considered in this analysis.

6.2. Simulated Datasets

To investigate efficiencies and model the data, simulated dijet events produced by the Pythia 6.425 [65] event generator are used. Pythia implements a LO matrix element for 2→2 processes, a p_{T}-ordered parton shower with leading-logarithmic accuracy and multi-parton interactions to simulate the underlying event. The hadronisation is described using the Lund string model, as described in Sect. 4.4.3. Events were generated with the MRST LO** [24,66] PDFs and a set of specially tuned parameters, AUET2B-LO** [72]. The '**' notation used in the PDF naming scheme implies an MC-adapted PDF [73–75]. Such PDFs are designed to give LO PDF behaviour in regions of phase space relevant for soft QCD models while at the same time modifying the high-x PDF to resemble NLO calculations. The generated events are passed through a full simulation [68] of the ATLAS detector and trigger based on GEANT4 [69].

The cross-section measurements are compared to NLO predictions generated using the POWHEG [55–58] and MC@NLO [59, 60] methods. Events are generated using the CT10 [22] PDFs and a b-quark mass of 4.95 GeV. Events generated with the POWHEG method are showered with Pythia 6 and MC@NLO events are showered with Herwig 6 [76]. As with Pythia 6, Herwig 6 is a LO MC generator. It uses an angular-ordered parton shower with a cluster hadronisation model. Herwig 6 uses the MRST LO** PDFs and the set of tuned parameters AUET2-LO** [77].

To improve the accuracy of the simulation, the inclusive jet p_{T} spectrum is reweighted to match the inclusive jet p_{T} spectrum in data. This reweighted MC is used throughout this analysis. The only time the unweighted prediction is used is for the final data/MC comparison in Sect. 6.7.

6.3. Purity Fit

The sample of b-tagged events contains light-, c- and b-jets. A template fit, using a binned likelihood method, is performed to identify the fraction of di-b-jet pairs in this sample. By requiring two b-tags, very few light jet pairs are accepted. As such, the distinction between c-jets and b-jets is important. The templates to derive the fraction of di-b-jet pairs are based on the sum of the probability of a jet originating from a b-quark divided by the probability of a jet originating from a c-quark for each jet in the dijet pair, as described in equation 6.2.

$$\log\frac{p_{b,1}}{p_{c,1}} + \log\frac{p_{b,2}}{p_{c,2}}, \tag{6.2}$$

where $p_{f,i}$ is the probability of a jet i to be of flavour f. The templates are constructed using the Monte Carlo simulation described in Sect. 6.2. For each bin in each distribution, templates for the different jet flavour combinations need to be created. Unfortunately, for the dijet system, some bins have very few MC events to form these templates. Thus, forming dijet templates directly isn't possible and a single jet convolution method is used. The characteristics looked for by a b-tagger in one jet are independent of the other jet in the dijet system and largely independent of any variable except p_{T}. As such, single jet templates can be derived based on the jet flavour and p_{T}, then convoluted together to for a dijet template. Instead of each dijet event in a bin representing one entry in a template, each event represents a complete template. For a given bin in the analysis, the dijet template for a flavour pair is the sum of all corresponding flavour pair dijet templates in the bin. Templates are created for four flavour combinations, (b,b) , $(b,?), (c,?)$ and (l,l), where $(q,?)$ refers to jet pairs with at least one jet of flavour q, except flavours which are heavier then q. An example of the constructed templates and their fit to data can be seen in Fig. 6.3.

To test this method, the dijet templates derived directly from MC are compared to the dijet templates derived from single jet convolution in Fig. 6.4. Despite the large statistical uncertainties on the direct method, good agreement can be seen between the two methods. The convolution methods makes use of the much larger single jet statistics and any statistical fluctuations present is smoothed out due to the convolution process. Due to the small statistical uncertainties, the template fit is done assuming no uncertainty on the templates.

While the convolution method deals with statistical fluctuations in the Monte Carlo, the trigger prescales introduce large statistical uncertainties in the data. Due to the finite event output rate of ATLAS and the jet production rate falling steeply with respect to p_{T}, the prescale weight associated with some events can be tens of thousands of times that of an unprescaled event. These fluctuations cause problems for the convergence of the template fit. To deal with such fluctuations, instead of

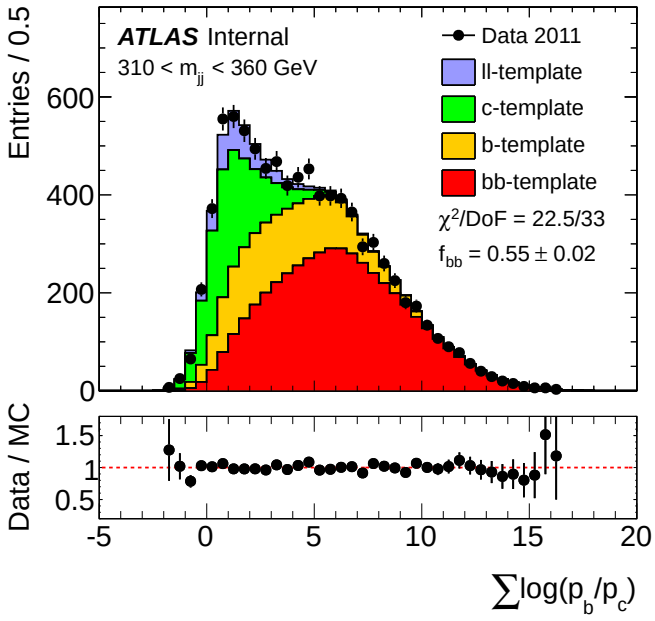

Figure 6.3.: Example of a dijet flavour template fit.

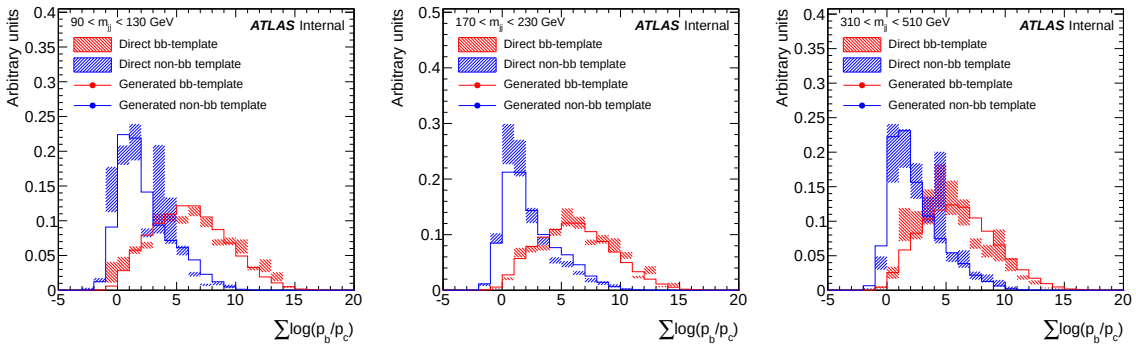

(a) **(b)** **(c)**

Figure 6.4.: Comparison of the direct and convoluted methods of deriving dijet templates.

scaling the prescaled event up, the templates which represent the events with the same p_{T} are scaled down. This ensures the p_{T} spectrum of events in both data and MC are the same and avoids large fluctuations. However, an implicit assumption of this method is that the p_{T} of the leading jet in the event does not have a significant correlation with the shape of the template fit variable. This was investigated, and the effect was found to be negligible. After the fit is performed, the fraction of di-b-jet pairs in the event is then scaled to the appropriate luminosity.

6.3.1. *b*-Tagging Efficiency

As mentioned in Sect. 5.2, an algorithm designed to identify typical b-jets will miss atypical ones. This effect needs to be corrected for and is done using correction factors derived from MC. As with the purity fit templates, deriving dijet correction factors directly from the MC gives results with large statistical fluctuations. As such, the single jet convolution method is used to derive the efficiency. A comparison between the direct and convolution methods is shown in Fig. 6.5.

6.4. Unfolding

As mentioned in Sect. 4.3, to compare measured data to theory predictions the detector effects need to be accounted for.

The simplest form of unfolding is the bin-by-bin unfolding method. This method treats each bin in a distribution as an independent measurement and corrects them separately. In this analysis, the measured detector level cross-section is corrected to the particle level using the Iterative, Dynamically Stabilised (IDS) unfolding technique [78]. The IDS method has two benefits over the bin-by-bin unfolding method. The primary benefit is the IDS method keeps track of the movement of events between bins, this means the correlations between the measured values in different bins can be dealt with. The bin correlations are important if the shape of the data is different to that of simulation. For example, an increase in the number of events in one bin means the event migration to other bins will also increase. While the relative rate of bin migration from the bin with the excess may not change, the neighbouring bins will receive more events and their relative rate will vary compared to the bin-by-bin prediction. The other is the ability to handle and incorporate new structure present in the data but missing from the MC simulation. The shape difference that meant more events migrated from an excess to it neighbours means the bin becomes a more likely source of events as well. When trying to move events back to the bin they originated from, this extra source of events needs to be accounted for. This feature allows the unfolded data to be used for searches for new physics. An example is if a new resonance is found that introduces a bump. By including

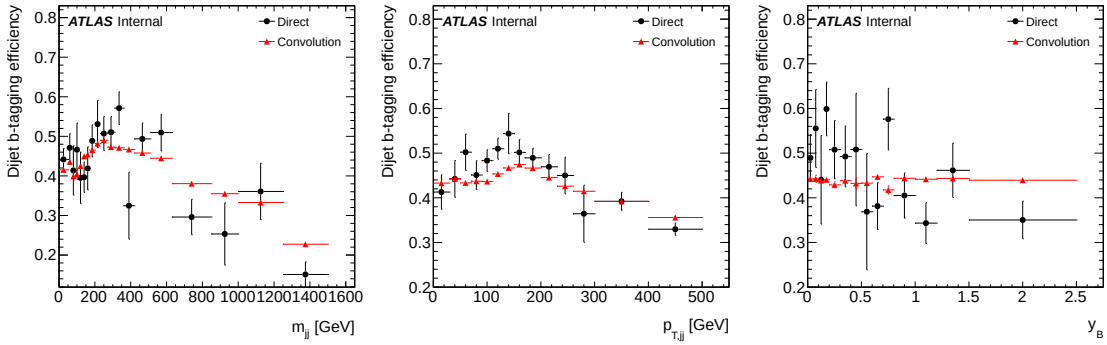

(a) $\varepsilon_{bb}(m_{\mathrm{jj}})$ **(b)** $\varepsilon_{bb}(p_{\mathrm{T,jj}})$ **(c)** $\varepsilon_{bb}(y_B)$

(d) $\varepsilon_{bb}(\chi)$ **(e)** $\varepsilon_{bb}(\Delta\phi_{\mathrm{jj}})$ **(f)** $\varepsilon_{bb}(\Delta R_{\mathrm{jj}})$

Figure 6.5.: Comparison of the results for the b-tagging efficiency correction factors derived with the direct (black) and convolution (red) method.

the information about this bump into the unfolding, the rate of event migration to and from the bins containing the bump can be altered. The IDS is different from a standard iterative Bayesian method because of its ability to sensibly deal with statistical fluctuations. Instead of performing a fixed number of iterations, the IDS method uses regularisation functions to identify statistical fluctuations and if necessary exclude them from the iterative process.

6.4.1. Method

The unfolding primarily takes into account bin migrations due to detector resolution. This information is contained within transfer matrix, which is derived from MC containing the particle (truth) and detector (reconstructed) level simulation. In a binned measurement, a transfer matrix describes the migration of events that were generated in bin i but were reconstructed in bin j. While it is never directly used in the unfolding, it contains all the information from the simulation relevant to the unfolding. The transfer matrix is only defined for events where both the particle and detector level results are within the fiducial boundaries of the analysis. Thus detector level events are omitted when the particle level result is outside the fiducial boundaries and vice versa. After events have been passed through the transfer matrix, the results are corrected for detector inefficiencies. This is shown diagrammatically in Fig. 6.6.

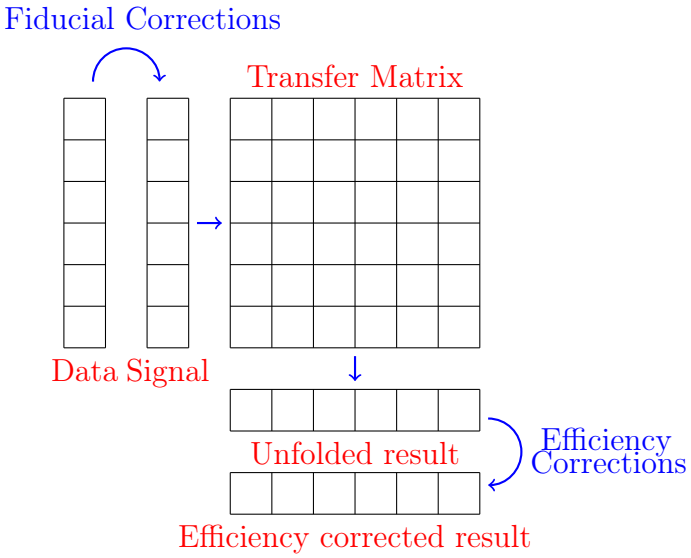

Figure 6.6.: Diagram of the unfolding procedure.

Using the transfer matrix, A_{ij}, the folding, P_{ij}, and unfolding, $\tilde{P}_{ij}$, matrices are determined:

$$P_{ij} = \frac{A_{ij}}{\sum_{k=1}^{N_{bins}} A_{kj}} \tag{6.3}$$

and

$$\tilde{P}_{ij} = \frac{A_{ij}}{\sum_{k=1}^{N_{bins}} A_{ik}}, \tag{6.4}$$

where P_{ij} gives the probability for an event generated in bin j, to be reconstructed in bin i, and $\tilde{P}_{ij}$ gives the probability for the 'source' of an event reconstructed in bin i to be in bin j. While the transfer matrix describes the total predicted bin migration of events in a given bin, P_{ij} and $\tilde{P}_{ij}$ describe the probability for the migration of one event. In addition to the folding and unfolding matrices, the particle- and detector-level predictions are derived from the transfer matrix.

In many situations, there are normalisation issues with the MC. This is accounted for by scaling the MC to the data. If the data has 'unknown' structure from physics not included in the MC, then this may affect the overall normalisation. Ideally, the MC unfolding would only be scaled to the 'known' physics in the data; the unknown parts will be accounted for later. To do this, the IDS makes use of regularisation functions.

Regularisation functions try to quantify the probability that a discrepancy between data and MC is from a statistical fluctuation or from unknown physics. A regularisation function is determined by 3 variables, $f(\Delta x,\sigma,\lambda)$, where Δx is the difference between data and simulation; σ is the uncertainty associated to the data and simulation and λ is a scaling factor. When $\Delta x = 0$, $f(\Delta x,\sigma,\lambda)$ should return 0. When $\Delta x \gg 0$, i.e. a large disagreement between data and prediction, $f(\Delta x,\sigma,\lambda)$ should return 1. There are many functions that can satisfy these criteria, two were investigated in this analysis:

$$f_1 = 1 - e^{-\left(\frac{\Delta x}{\lambda\sigma}\right)^n}, \tag{6.5}$$

$$f_2 = 1 - \frac{1}{1 + \left(\frac{\Delta x}{\lambda\sigma}\right)^n}. \tag{6.6}$$

The behaviour of these functions can be seen in Fig. 6.7. The power term, n, affects the slope of the function. Assuming, when $f(\Delta x,\sigma,\lambda)$=1 the function is 'on', the regularisation term, λ, affects the 'turn on' point. A smaller value of λ means a quicker turn on.

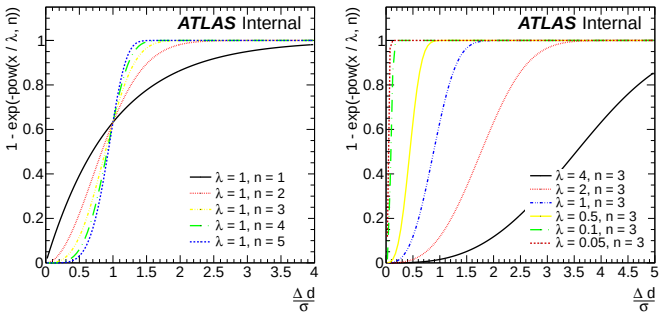

Figure 6.7.: IDS regularisation functions plotted against $\frac{\Delta x}{\sigma}$ for different values of n and λ, with $\frac{\Delta x}{\sigma}$ used as a proxy for the statistical significance of the difference between data and simulation.

To scale the MC to the data, the ratio of the number of MC events to the number of data events from known physics is taken. The number of data events in the ratio is calculated iteratively. The initial estimation of the number of known data events, N_D^k, is the total sum of all data. Step 2 loops over each bin, adding or subtracting the number of events that are likely to be from unknown physics using a regularisation function. This is expressed in equation 6.7:

$$N_D^{k\prime} = N_D^k + \sum_{k=1}^{Nb}(1 - f(|\Delta d_k|, \tilde{\sigma}(d_k), \lambda_N)) \cdot \Delta d_k. \tag{6.7}$$

The new estimate of the number of known data events is compared to the previous estimate. If the two values are close enough, the iterations are stopped. If not, step 2 is repeated. This is shown in Fig. 6.8.

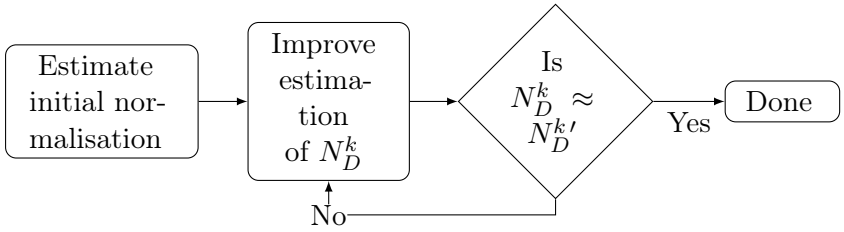

Figure 6.8.: Flow chart of the MC scaling process.

After the data and MC are normalised, the actual unfolding can take place. This is done one bin at a time. An initial estimate for the particle level bin value is taken as the MC truth value. The difference between the number of data events and reconstructed MC events is then looked at. This is shown in equation 6.8.

$$u_j = t_{MCj} \cdot \frac{N_D^k}{N_{MC}} + \sum_{k=1}^{Nb} \begin{cases} f(|\Delta d_k|, \tilde{\sigma}(d_k), \lambda) \cdot \Delta d_k \cdot \tilde{P}_{kj} & \text{if } \mathrm{r}_{MCk} \neq 0 \\ \quad +(1 - f(|\Delta d_k|, \tilde{\sigma}(d_k), \lambda)) \cdot \Delta d_k \cdot \delta_{kj} & \\ \Delta d_k \cdot \delta_{kj} & \text{otherwise} \end{cases} \tag{6.8}$$

If Δx is consistent with a statistical fluctuation, i.e. f(Δx,σ,λ) is small, then the fluctuation is incorporated into the unfolded estimation without modification. However, if Δx is consistent with unknown physics, the events making up the difference are unfolded. The ability to sensibly deal with statistical fluctuations is a useful feature of this method.

The last step of the iteration process is to incorporate unknown structure into the transfer matrix. This is done as described in equation 6.9.

$$A'_{ij} = A_{ij} + f(|\Delta u_j|, \tilde{\sigma}(u_j), \lambda_M) \cdot \Delta u_j \cdot \frac{N_{MC}}{N^k_{MC}} \cdot P_{ij} \tag{6.9}$$

Here, the difference between the truth MC and unfolded data, Δu, is used to indicate new physics. Any differences between the unfolded data distribution and the predicted truth distribution are added into the transfer matrix via the folding matrix. The iteration process stops if there is little change between A'_{ij} and A_{ij}, this can be seen diagrammatically in Fig. 6.9. For this analysis, the iterations stop when every element in A'_{ij} and A_{ij} are within 1% of each other.

The limited MC statistics for the derivation of transfer matrices means it is important to take into account the MC uncertainty in the regularisation functions. When bins are modified, the uncertainty is scaled by the change in the bin central value.

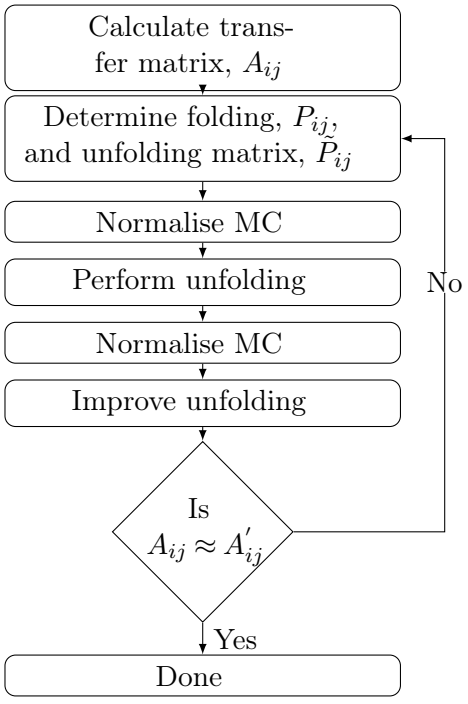

Figure 6.9.: Flow chart of the IDS unfolding method.

6.4.2. Fiducial and Efficiency Corrections

The data before unfolding represents a pure sample of b-jets. To represent this in the transfer matrix, detector jets with a b-hadron within a $\Delta R < 0.3$ are defined as b-jets and are matched to particle jets. The particle jet is identified by finding the closest particle jet, in ΔR, to the detector jet. If no particle jet is found with a $\Delta R < 0.3$ to the detector jet, the event is rejected. Inefficiencies, such as this, in event reconstruction are accounted for by fiducial and efficiency corrections, applied before and after the unfolding. A primary effect to correct for is the detector smearing a jet into or out of the fiducial resolution of the analysis. For instance, if a 39 GeV particle-level jet is measured with 40.1 GeV it would, falsely, be included in this analysis. This effect is corrected for by calculating the chance of matched particle-jets pair failing the fiducial selections of the analysis. Another effect is that a 40.1 GeV particle jet is measured with a p_{T} less then 40 GeV. This effect is calculated by applying the event selection on particle-level jets to select a di-b-jet pair and matching them to detector-level jets. The matching is done by looking for a detector jet with $\Delta R < 0.3$ of the selected particle. An efficiency correction is calculated for the detector-level jets that fall outside of the fiducial bounds of the analysis. The term fiducial correction in this case corresponds the corrections with respect to detector-level jet pairs that should be included in the analysis but were not. The efficiency correction accounts for particle-level jets that have incorrectly excluded the measurement. The fiducial corrections, which are applied before the unfolding, account for the following inefficiencies:

- detector jets that are matched to a particle jet that fails the event selection (i.e. $p_{\mathrm{T}} < 40$ GeV, no matched b-hadron or $|\eta| > 2.5$) and
- detector jet pairs that are matched to particle jet pairs with kinematics outside the studied fiducial range (e.g. $m_{jj} < 110$ GeV in the mass distribution).

The efficiency corrections, which are applied after the unfolding, include the following:

- trigger inefficiencies;
- particle jets that are matched to a detector jet that fails the event selection;
- particle jet pairs that are matched to a detector jet pair with kinematics outside the studied fiducial range, and
- differences between analysis-selected particle jets and the detector-jet-matched particle jet.

The corrections for the dijet mass distribution can be seen in Fig. 6.10, the corrections for the other distributions are shown in Appendix B. Some structure can be seen in the corrections due to competing effects from different detector inefficiencies, such as the jet energy resolution discussed earlier. This is particularly

evident in the dijet p_{T} distribution. The largest correction in both cases comes from the matched jet being below the p_{T} cut in the event selection.

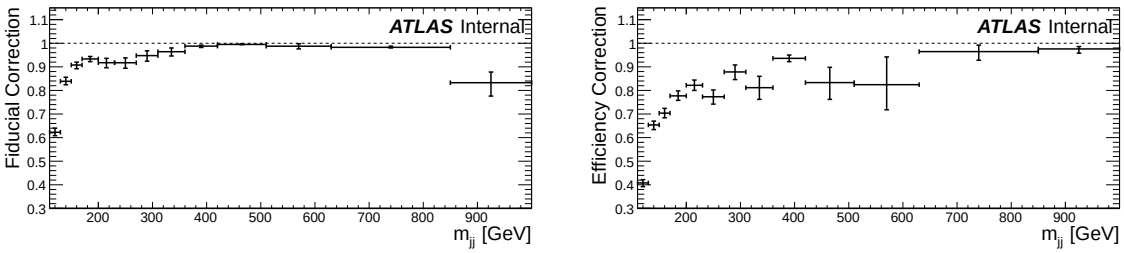

Figure 6.10.: Fiducial and efficiency corrections applied to the dijet mass measurement. The drop in the final m_{jj} fiducial correction bin is due to events with a particle level mass above 1000 GeV being measured with lower mass and so included in the distribution.

6.4.3. Parameter Choice

The free parameters within the unfolding are those that control the regularisation function. By using Monte Carlo, the results of different parameter values can be evaluated. The parameter scan was done with three different test cases:

- unfolding half of the Pythia 6 dijet MC with a transfer matrix derived from the other half;
- unfolding Herwig 6 MC with a transfer matrix derived from Pythia 6, and
- unfolding Pythia 6 dijet MC with an injected 900 GeV Z' signal with a transfer matrix derived using Pythia 6.

In all these cases, the 'success' was evaluated with a χ^2 test. The parameters n, λ_M and λ_U were varied. Sample plots of the results can be seen in Fig. 6.11. The ΔR distribution favoured a low λ_U. However, in all other distributions this parameter had little effect on the unfolding. The Herwig 6 tests were most sensitive to n, where a higher value was preferred. The values chosen for the analysis were n = 5, $\lambda_M = 3.75$ and $\lambda_U = 0.75$.

6.4.4. Propagation of Statistical Error

In order to account properly for the statistical uncertainties present in the input values, the central values are varied within their uncertainties and fed through the

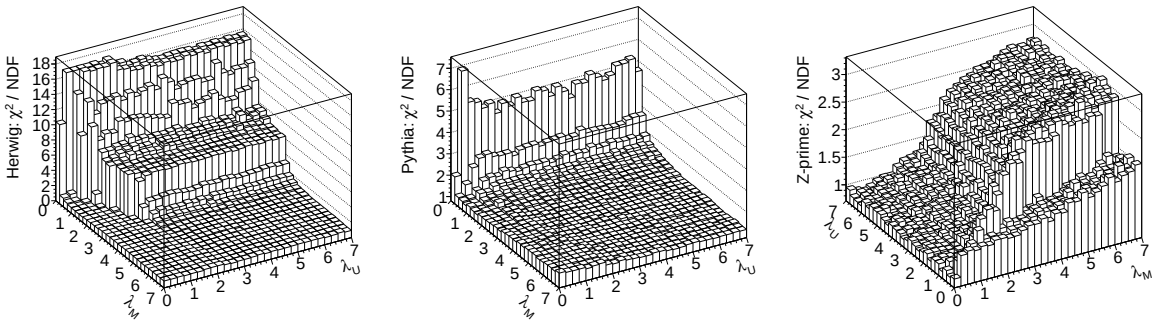

Figure 6.11.: Parameter scans of the dijet mass unfolding parameters, for n = 5.

unfolding process. The final uncertainty is taken from the resulting spread of output values. Every time the process is repeated, the value of the bin is recorded with respect to the nominal value according to equation 6.10.

$$x = \frac{x_{nom} - x_{var}}{x_{nom}} \tag{6.10}$$

The results of such a variation with respect to the mass can be seen in Fig. 6.12. The expectation value for each bin is taken as the central value and the uncertainty is taken as 34.1% of the distribution up and down from the expectation value. Examples of a bin with small and large statistical uncertainty in the fits can be seen in Fig. 6.13.

To do the above variation, knowledge on the distribution of uncertainties is important. Values from the data, as they come from a purity fit, are assumed to be Gaussian, while the uncertainties from the transfer matrix are assumed to follow a Poisson distribution. As the transfer matrix is made from weighted samples, each MC sample is varied independently. The unweighted number of events in each bin is used to calculate the uncertainty. The weighted MC samples used to calculate the efficiencies are an additional complication. Efficiency calculations have a Poisson-like uncertainties, but Poisson uncertainties need to be calculated with unweighted data. The central values are reasonably straightforward: the efficiency is the ratio of the weighted sum of the number of events that pass over the total number of events. The variance on the result is the weighted average. In order to deal with the weighted events, the efficiency probability distribution function (pdf) is assumed to follow a beta distribution, as described by the equation 6.11 [79]:

$$p(x; a, b) = \frac{\Gamma(a+b)}{\Gamma(a)\Gamma(b)} x^{a-1}(1-x)^{b-1}, \tag{6.11}$$

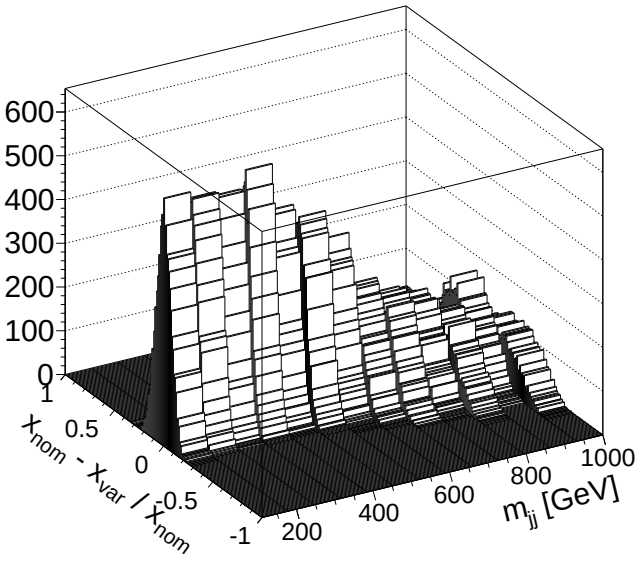

Figure 6.12.: Toy MC to investigate the statistical uncertainty in the unfolding.

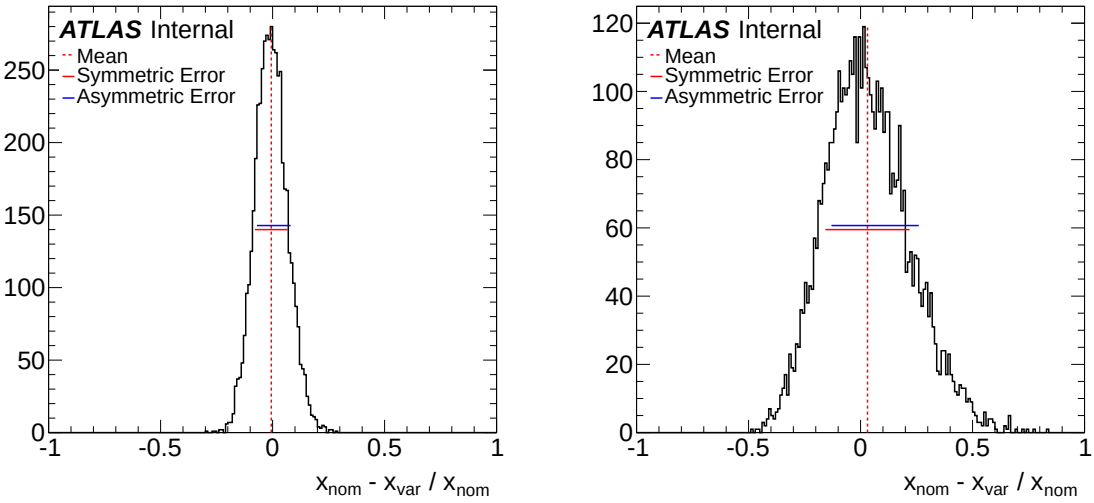

Figure 6.13.: Example uncertainty distributions in bins with high and low statistics.

where Γ is the gamma function and a and b are found using the central values of the efficiency and variance in the MC:

$$a = E\left[\frac{E(1-E)}{V} - 1\right], \tag{6.12}$$

and

$$b = (1-E)\left[\frac{E(1-E)}{V} - 1\right]. \tag{6.13}$$

E and V are the expectation value and the variance of the efficiency, respectively. When E is close to 1 this approximation breaks down. In practice, the variance from a binomial distribution for these cases is very small. The small variance means a Gaussian approximation can be used with little fear of having a value more than one. When this does occur, the value is taken as $x' = 1-(x-1)$, where x is the result of the Gaussian smearing and x' is the recorded value. The Gaussian approximation is only used in cases were $E > 0.99$. The shape of the different uncertainty approximations can be seen in Fig. 6.14. The same method is used to calculate the trigger efficiency uncertainty distribution, which is taken to be the luminosity weighted average of the different triggers.

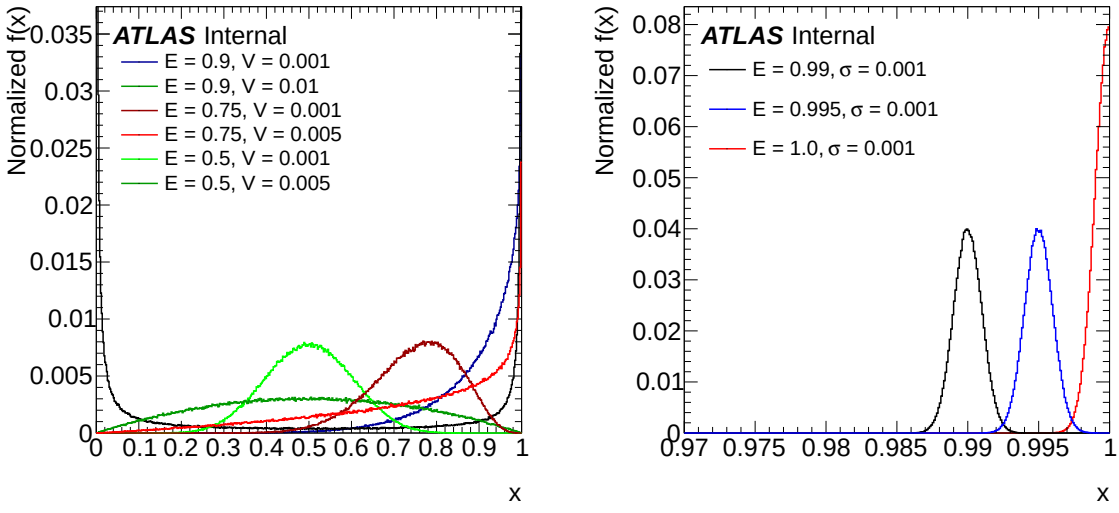

Figure 6.14.: Uncertainty distribution for different prior assumptions.

6.4.5. Closure Checks

Using the values decided upon by the parameter scans, the next step is to see if the detector level MC results can be corrected back to the particle level for all the test cases. The three test cases used in the unfolding parameter estimation, mentioned in Sect. 6.4.3, were also used for the closure checks. The results for the dijet mass distribution can be seen in Fig. 6.15, the other variables can be seen in Appendix C. In general, accounting for the statistical variation there is good agreement between the unfolded and particle level values. The excellent closure for the majority of the phase space for the Z' variables is expected the only difference between the MC used for the unfolding parameters and input sample is the injected Z' signal.

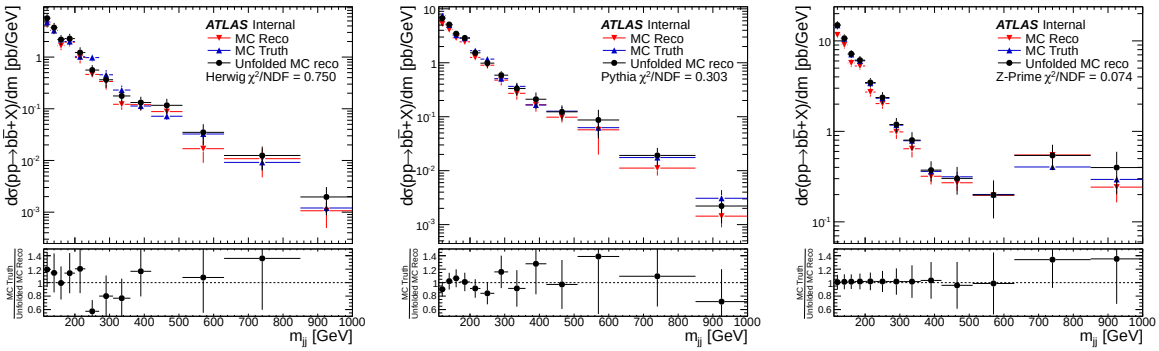

Figure 6.15.: Closure test of the unfolding for different Monte Carlos.

6.4.6. Comparison with Bin-by-bin Unfolding

As well as checking the internal consistency of the IDS unfolding method, the results were compared to an independent unfolding method. Bin-by-bin unfolding was used as the cross-check. As mentioned earlier, bin-by-bin unfolding works by taking the ratio of the detector jet and particle jet distributions, combining all the necessary corrections into a single factor. Despite being less sophisticated, it is still considered a robust method.

To perform the test, the data was unfolded using both the IDS and the bin-by-bin method. The ratio of the results was then plotted, shown in Fig. 6.16, to compare the results. To judge the agreement between the two methods, the correlated errors between the two results need to be removed. These come from two sources, the use of the same MC and the same input data. The errors from the input data are dealt with by not propagating them through the unfolding. However, the correlated errors from the MC are non-trivial to untangle and so are left in. Within the statistical uncertainties, there is good agreement across all distributions.

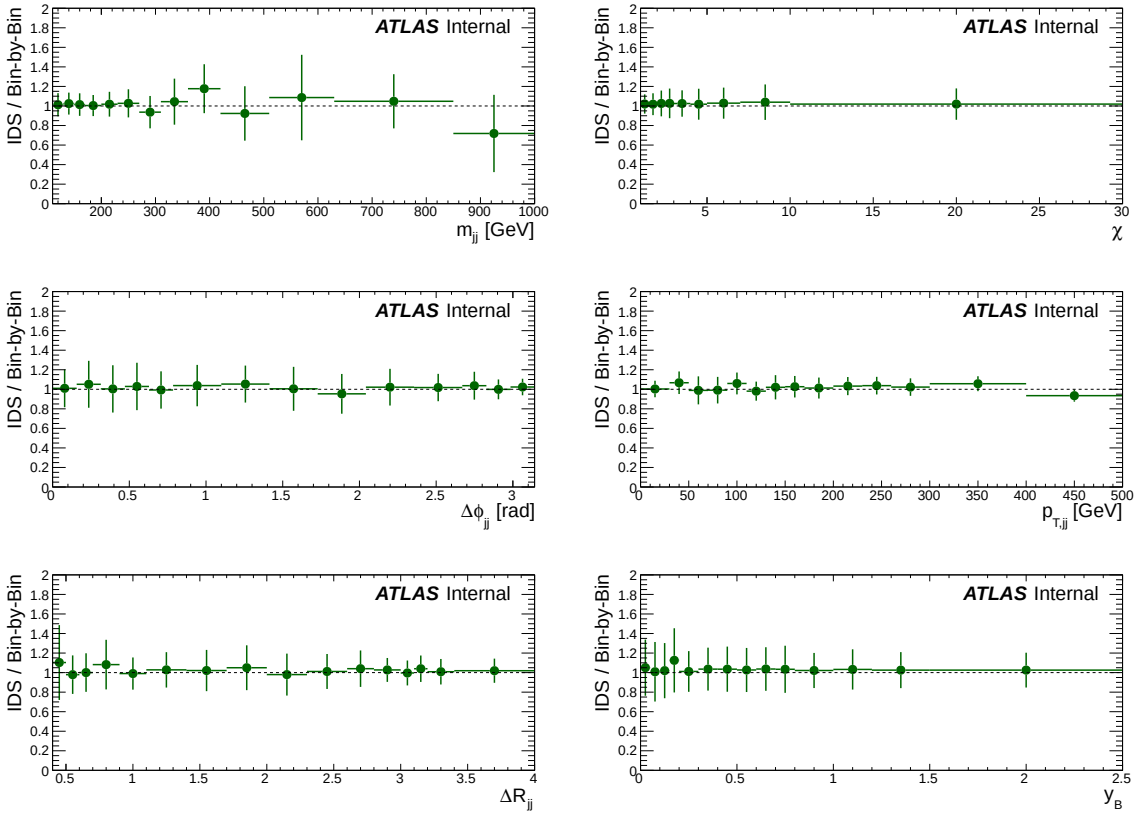

Figure 6.16.: Comparison of IDS unfolding to bin-by-bin unfolding.

6.5. Theory

In this analysis, NLO events are generated using the POWHEG-BOX hvq module and showered using the p_{T}-ordered parton shower of Pythia 6. The MC@NLO events are showered with Herwig 6. For both generators, the b-quark mass was set to 4.95 GeV and the CT10 PDFs were used.

6.5.1. Theoretical Uncertainties

As discussed in chapter 5, the main sources of uncertainty are the choice of μ_R, μ_F and PDFs. By far the largest source of theoretical uncertainty comes from the μ_R scale variation. This varies from around 20% up to 50% in regions of phase space where the two b-jets are close together. In addition to the PDF and scale uncertainty, additional sources of uncertainty were examined to evaluate their affect on the theoretical predictions.

Number of Light Quark Flavours

While $b\bar{b}$ production with MC@NLO is designed to work with PDFs that treat b-quarks as light, the case for the POWHEG is less clear. This ambiguity also extends to whether b-quarks should be produced from the parton shower, as this runs the risk of double counting higher order terms. To investigate the effect of the model ambiguity, the following configurations were studied:

(1) 5 light quarks in the PDF and $g \to b\bar{b}$ allowed in the parton shower.

(2) 5 light quarks in the PDF and no $g \to b\bar{b}$ allowed in the parton shower.

(3) 4 light quarks in the PDF and $g \to b\bar{b}$ allowed in the parton shower.

(4) 4 light quarks in the PDF and no $g \to b\bar{b}$ allowed in the parton shower.

The results of these variations can be seen in Fig. 6.17. Decreasing the number of light quarks in the PDFs appears to have little effect on the shape of the distributions, but does uniformly raise them. This can be understood as the b-quarks being translated into an increased gluon contribution in the PDFs. By not including gluon splitting in the parton shower, not only is the overall rate reduced but also the shape is modified. Option (1) was chosen for the central value of the theory prediction. It was decided to keep $g \to b\bar{b}$ in the parton shower as this allows the NLO prediction to have more than 2 b-jets in the final state. As this is something that is explicitly accounted for in the unfolding step, it seems appropriate to include the effect in the theory prediction. The choice of using a 5-flavour PDF was made to remain consistent with other ATLAS measurements.

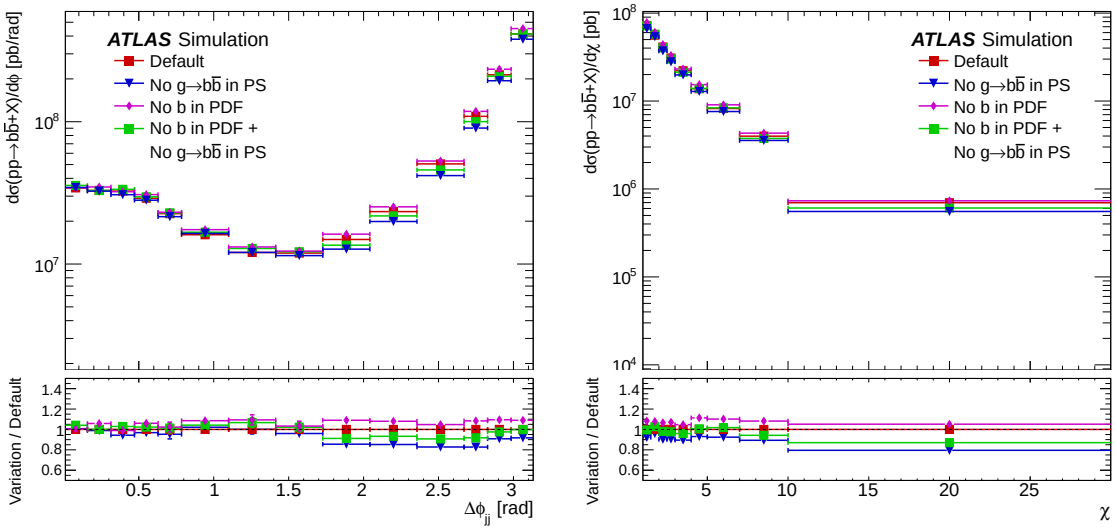

Figure 6.17.: Effect of the number of light quarks used in the parton shower and PDF.

Scale Matching in POWHEG

The POWHEG method works by generating the hardest emission in the event at NLO accuracy, then allowing the parton shower to fill in the rest of the emissions. The p_{T} of the hardest emission is passed on to the parton shower, this is known as the matching scale. Problems can occur if the p_{T} of an emission in POWHEG and the parton shower are calculated with respect to different reference frames. In these cases the scale at which the parton shower starts can be too high. If this happens, initial state radiation (ISR) can dominate the event, changing the overall event topology. In the example depicted in Fig. 6.18, the hard ISR pushes the back-to-back b-jets close together. To evaluate the effect of the possible scale mis-match, the scale of an event is modified according to recommendations of the POWHEG authors. The modified scale is taken as the minimum of the three possibilities:

- the p_{T} of the partons,
- the square root of the dot product of a parton with any other parton in the event, or
- the original scale.

Applying these modifications has the effect of reducing the matching scale, thus reducing the importance of the parton shower on the event kinematics. The above recommendations were intended for use with the inclusive jet production. To explore the effect on heavy quark production, the scale was modified with respect to just the b-quarks as well. The effect of the scale matching can be seen in Fig. 6.19. As

expected, the largest effects are seen in the regions of phase space dominated by close-by b-jets. The effect of the scale matching is about 20% in these regions. The scale matching uncertainty isn't included in the final quoted theory uncertainty as this behaviour is the result of a 'feature' of POWHEG. The main aim of the study was to investigate the structure seen in the $d\sigma/dp_{\mathrm{T,jj}}$ distribution, as discussed in Sect. 6.7, and the conclusion is that the scale matching does not explain that feature.

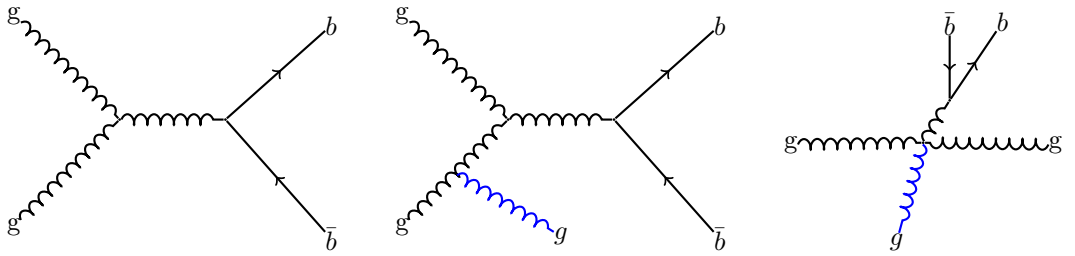

(a) Flavour creation **(b)** Hard ISR **(c)** "Gluon-splitting-like" event

Figure 6.18.: Possible effects of incorrect scale matching in POWHEG.

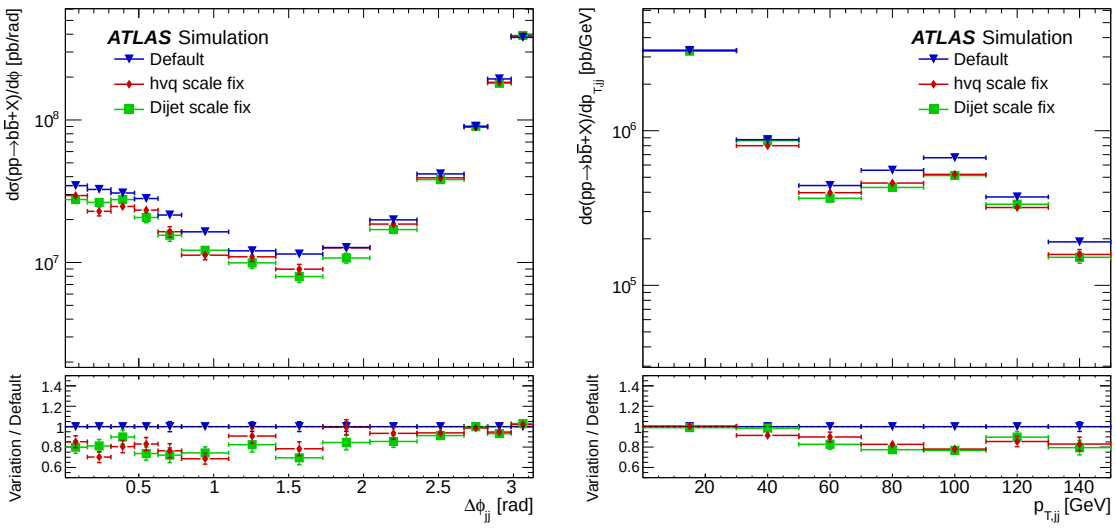

Figure 6.19.: Effect of the different POWHEG matching scales.

Variation of b-quark Mass

The POWHEG Monte Carlo simulation uses the pole mass of the b-quark as an input parameter. However, the accuracy to which the mass is constrained is of the

order of Λ_{QCD}. In order to investigate the effect of the b-quark mass on the theory predication, the nominal value, 4.95 GeV, was varied up and down by 1 GeV. The effects of the variation can be seen in Fig. 6.20. The $p_{\mathrm{T,jj}}$ distribution shows that the effect of changing the b-quark mass is of the order of 10%. As the effects of the b-quark mass are small compared to the scale variation they are not included in the final quoted theory uncertainty.

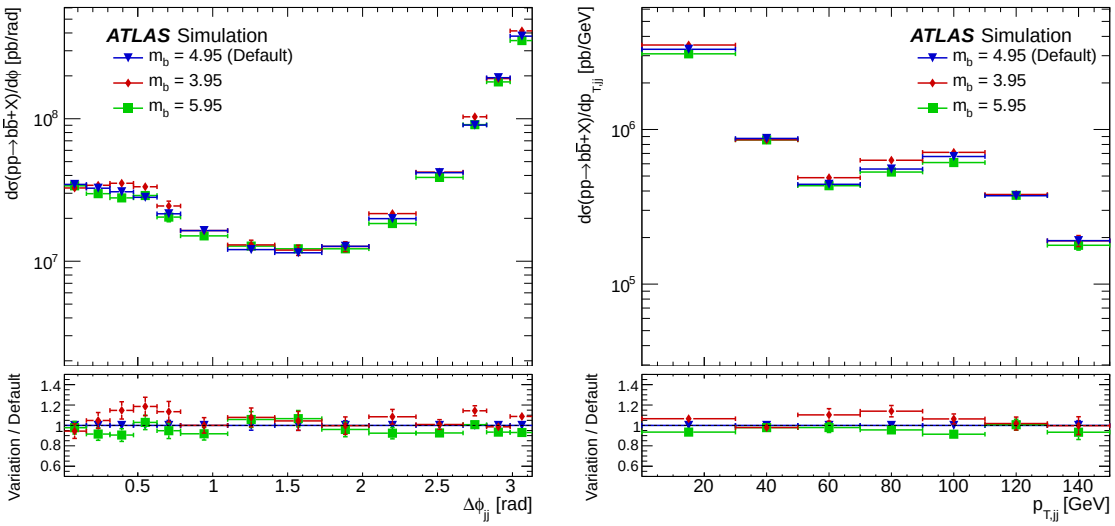

Figure 6.20.: Effect of the b-quark mass in the POWHEG-BOX hvq simulation.

6.5.2. Practical Considerations

There are limitations for any tool. In this case, the challenge when generating $b\bar{b}$ events is to efficiently generate high p_{T} events. The POWHEG-BOX hvq module has no means of preferentially generating these events. In a rapidly falling p_{T} spectrum, this means that a very large number of low p_{T} events are generated for each high p_{T} event. In order to save disk space and CPU time, two levels of filters are used to generate events in p_{T} slices based upon the p_{T} of the leading jet.

The first filter, between POWHEG and the parton shower, filters the Les Houches Event Format (LHEF) [80] events. POWHEG was adapted to feed events into a FIFO[2]. The LHEF filter then reads in all events and only writes out those that passed a p_{T} cut on the hardest parton. This filter works in the same way a matrix element level cut would. The main benefits of using the LHEF filter can be summarised in two points.

[2] An acronym standing for First In First Out, a method of organising and transmitting data on a computer

- Computer processing time; POWHEG-BOX generates events faster than a parton shower processes them. By only showering useful events, CPU time is spent on event generation rather then showering.
- Disk space; in many regions of phase space there is only one useful event per 10^6 or more. Saving and transferring such a large number of events before the showering stage is impractical.

Figure 6.21 shows the effect of the parton level cut on final state observables. The jet p_{T} spectrum is affected in a similar way for both the LHEF filter and matrix element cuts.

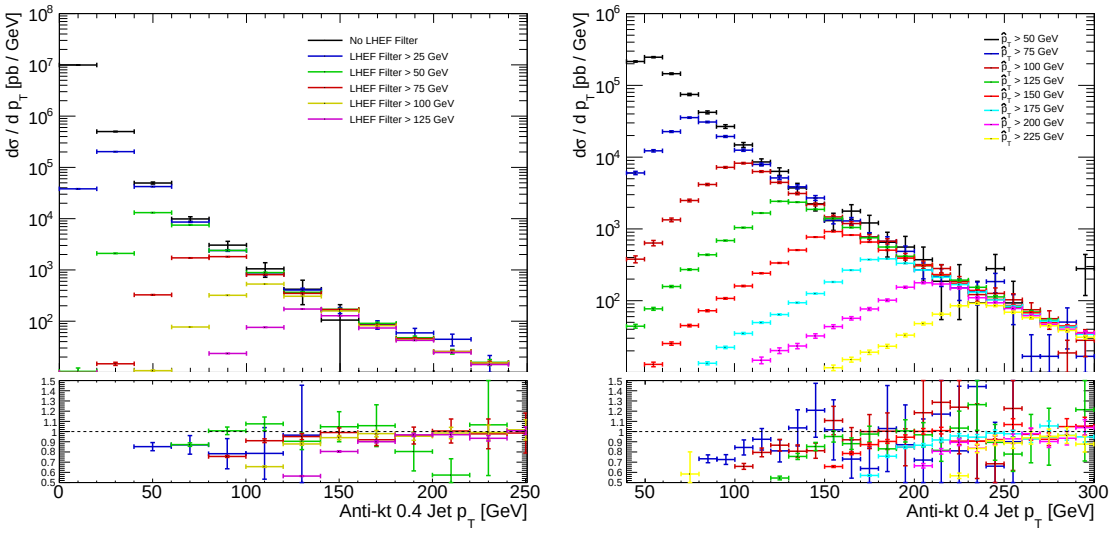

(a) LHEF filter **(b)** Matrix element cut

Figure 6.21.: Effect on jet p_{T} from a parton level p_{T} cut.

The next filter occurs after the parton shower. This filter is used to reduce the number of events that are saved. It only accepts events that satisfy the following conditions:

- contains two particle-level b-jets with:
  - $p_{\mathrm{T}} > 15\,\mathrm{GeV}$,
  - $|y| < 2.7$;
- the leading jet of the event has a p_{T} within a defined slice.

The p_{T} cuts in the filters are listed in Table 6.2. The results of the NLO predictions can be seen in section 6.7.

LHEF filter [GeV]	Parton Shower Filter [GeV]	
$p_{\mathrm{T,min}}^{\mathrm{parton}}$	$p_{\mathrm{T,min}}^{\mathrm{jet}}$	$p_{\mathrm{T,max}}^{\mathrm{jet}}$
0	0	150
75	150	300
200	300	600
400	600	-

Table 6.2.: p_{T} cuts applied to filtered POWHEG Monte Carlo samples.

6.5.3. Event Generation Validation

The samples were validated by comparing the newly generated POWHEG predictions to data from the previous b-jet analysis described in chapter 5. It can be seen in Fig. 6.22 that the agreement between the generated events is at a similar level to the previous analysis.

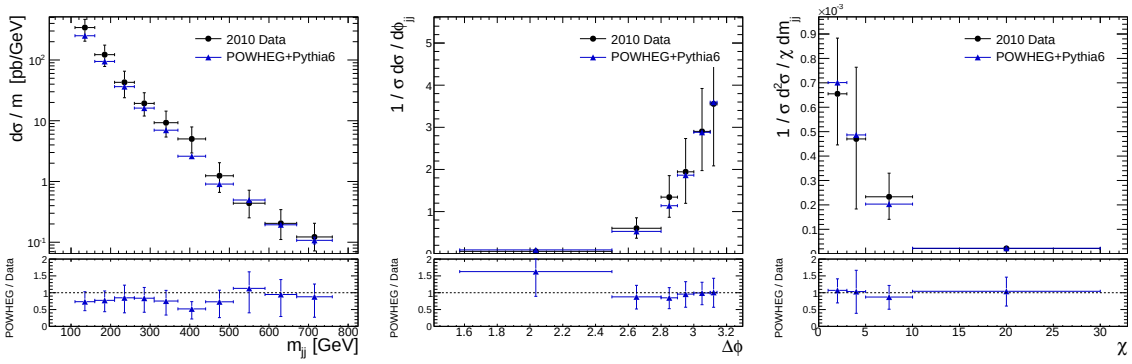

(a) Dijet mass distribution **(b)** $\Delta\phi$ distribution **(c)** χ distribution for events with $110 < m_{jj} < 370$ [GeV]

Figure 6.22.: Validation plots comparing POWHEG-hvq events to data.

Validating Filters

There is a chance that a bias could be introduced by applying the filter. This could be in the form of rejecting a region of phase space or as a normalisation issue. Figure 6.23 shows the leading jet p_{T} when all the POWHEG p_{T} slices are added together. A mistake in calculating the filter efficiency of a sample would show up here.

Any discontinuities in the regions where samples are joined, i.e. 150 GeV and 300 GeV, would indicate a problem. The different coloured distributions in the ratio plot show the same variable, but from samples with different scale values. Each distribution represents an independent calculation of the filter efficiency. It can be seen, within statistical error, there are no discontinuities in the POWHEG distributions.

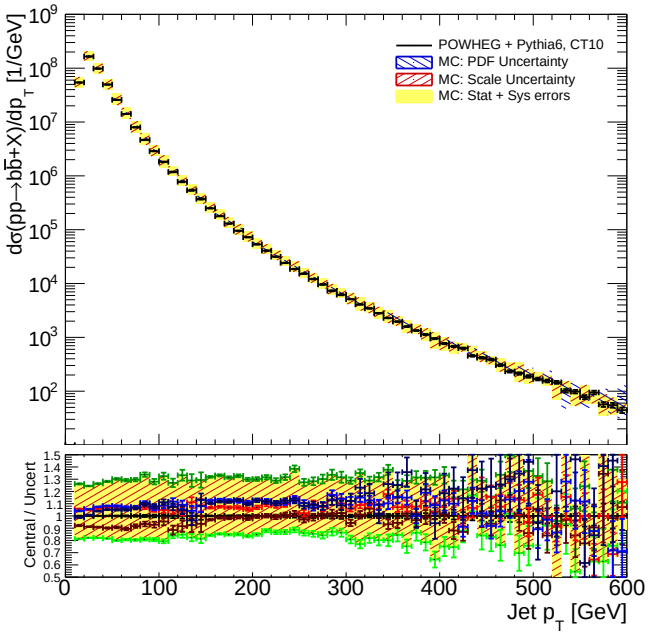

Figure 6.23.: Leading jet p_{T} distribution. The different colours in the ratio plot are the results of different scale variations.

To check if the filter introduced any bias due to its event selection, the filtered samples were compared to unfiltered samples. Unfortunately, the analysis p_{T} cut of 40 GeV placed on the b-jets means there are few usable events in an unfiltered sample. In order to a get a more statistically significant result, the p_{T} cut was lowered to 20 GeV for these validation tests. For the statistically significant regions, it can be seen that there is good agreement between the filtered and unfiltered samples. It can be seen in Fig. 6.24 that there appears to be no bias introduced by filtering the MC events.

6.5.4. MC@NLO

As mentioned in Sect. 4.4.5, POWHEG and MC@NLO deal with higher order terms differently. As $b\bar{b}$ production is sensitive to such terms, it is important to compare to both generators.

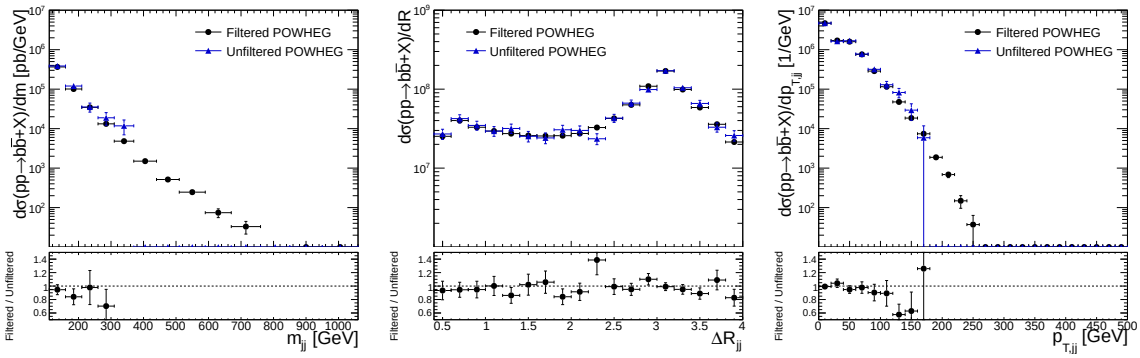

Figure 6.24.: Validation plots comparing filtered with unfiltered POWHEG events.

Practical Considerations

MC@NLO, like POWHEG, does not have a method of preferentially producing $b\bar{b}$ events in a desired region of phase space. In order to cover all the desired regions of phase space an additional filter was used between MC@NLO and the parton shower. Unfortunately, this is not as straightforward an operation as with POWHEG. The main difference is that MC@NLO will not always produce the hardest emission within the matrix element. Thus cutting on the p_{T} of the partons, $\hat{p_{\mathrm{T}}}$, in the hard process is only loosely related to the final jet p_{T}, $p_{\mathrm{T}}^{\mathrm{jet}}$. This can be seen in Fig. 6.25: events where the hardest parton have a p_{T} less then 5 GeV produce jets with a $p_{\mathrm{T}} > 90$ GeV. This is because MC@NLO does not produce the hardest emission within the hard process, nor is the Herwig 6 parton shower p_{T} ordered.

The loose relationship between $\hat{p_{\mathrm{T}}}$ and $p_{\mathrm{T}}^{\mathrm{jet}}$ means that the method used for filtering the POWHEG event samples is not appropriate for MC@NLO. Instead, events are produced in $\hat{p_{\mathrm{T}}}$ slices. A proof of principle of this can be seen in Fig. 6.26. The comparison between a high statistics MC@NLO inclusive sample and the sum of the three $\hat{p_{\mathrm{T}}}$ samples shows good agreement in the ratio plot.

The final cuts used for the MC@NLO event generation are shown in Table 6.3. In addition to the parton p_{T} cuts, for the lowest $\hat{p_{\mathrm{T}}}$ slice a leading jet filter is also used. This is to preferentially generate the low parton p_{T} events that have high p_{T} jets. Figure 6.27 shows the relative contribution each event slice makes to the overall sample. The POWHEG prediction is plotted to provide a comparison. This plot shows the extent to which the leading jet p_{T} does not depend on the parton p_{T}. Events with a parton $p_{\mathrm{T}} < 100$ GeV produced jets throughout the entire p_{T} range of the analysis. While the combined sum of MC@NLO should provide an accurate representation of the overall prediction, one should be careful when interpreting the event topology of high p_{T} events.

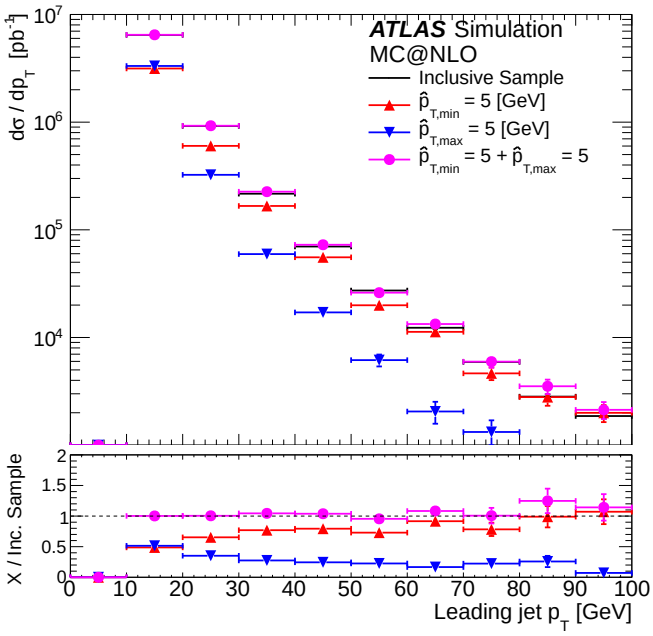

Figure 6.25.: Comparison of filtered MC@NLO samples.

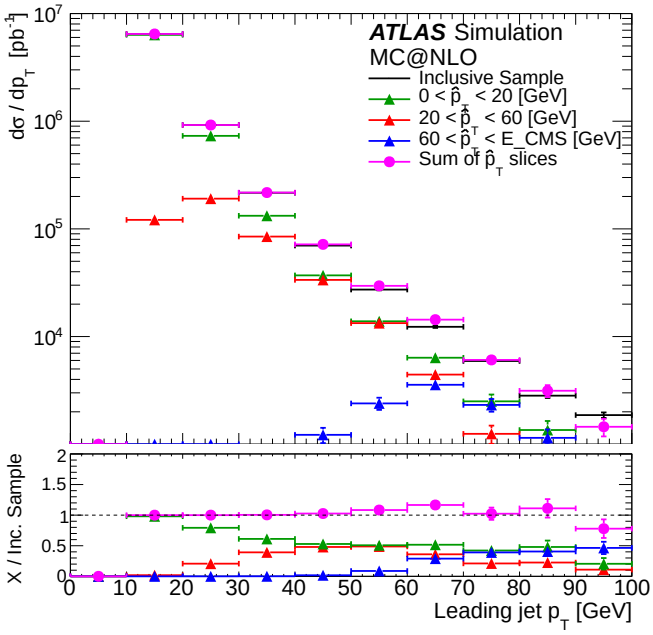

Figure 6.26.: Proof of principle for producing MC@NLO events grouped with respect to the high p_{T} parton in the hard process.

LHEF filter [GeV]		Parton Shower Filter [GeV]	
$p_{\mathrm{T,min}}^{parton}$	$p_{\mathrm{T,max}}^{parton}$	$p_{\mathrm{T,min}}^{jet}$	$p_{\mathrm{T,max}}^{jet}$
0	100	0	150
0	100	150	N/A
100	300	N/A	N/A
300	N/A	N/A	N/A

Table 6.3.: Parton and jet p_{T} cuts used in the MC@NLO event generation.

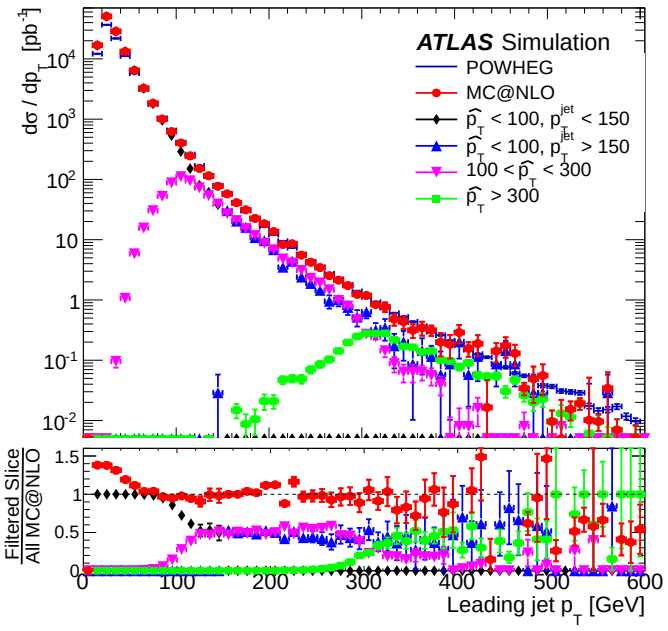

Figure 6.27.: Top Panel: Contributions from different MC@NLO event samples to the combined sum. POWHEG (blue) is shown for comparison. Bottom Panel: The ratio of the combined MC@NLO sample with POWHEG is in red. All other distributions are the ratio of the MC@NLO event slice and the combined total.

6.5.5. Topologies

The different lowest order production channels for $b\bar{b}$ tend to have characteristic event topologies. While at higher orders the distinction between a $b\bar{b}$ pair coming from GSP or FCR breaks down, the lowest order approximation does provide insight into the event kinematics. Using the p_{T} ordering of the jets as a handle, the analysis events can be separated into which lowest order production channel they are most similar to. Events are considered FCR-like if the two leading jets in the event are b-tagged, GSP-like events are those where neither b-jet is the leading jet, and the rest are considered FEX-like events. It is worth noting that the distinction between GSP and FEX events is somewhat ill defined. In general, they are clumped together as non-FCR-like events. Using these definitions, the events from POWHEG and MC@NLO are classified.

Figure 6.28 shows the contributions from different event topologies in the $p_{\mathrm{T,jj}}$ distribution. The FCR-like events are dominant for low $p_{\mathrm{T,jj}}$ values, but then fall away steeply. After $p_{\mathrm{T,jj}} \sim 80$ GeV FEX-like and GSP-like become dominant. This is expected, as the event selection does not allow GSP-like events until this point. Before the production of the $b\bar{b}$ pair, GSP events can be thought of as a pair of back-to-back gluons. In order to produce two b-jets with a $p_{\mathrm{T}} > 40$ GeV, they must be produced from a gluon with a p_{T} of at least 80 GeV. As such, the $p_{\mathrm{T,jj}}$ of such events is at least 80 GeV. There is a difference in the size of the structure at 80 GeV between the NLO predictions, MC@NLO predicts that the FCR-like events fall off much steeper than in POWHEG. The mass distribution shown in Fig. 6.29 has the opposite topological ordering. Here, FCR-like events dominate the entire observed distribution, as the majority of the GSP- and FEX-like events are in the low mass region below 110 GeV. The χ distributions, shown in Fig. 6.30, appear to be largely independent of event topology. This is a useful feature when trying to distinguish relative production rates. The variables ΔR and $\Delta\phi$, shown in Figs. 6.31 and 6.32 respectively, behave as expected. The back-to-back topology of the FCR events means that they tend to have an angular separation of around π, while the gluon-splitting-like events tend to be close together.

6.6. Systematics

This section will describe the procedures used to evaluate the effect of various systematic uncertainties on the cross-section measurement. The systematic uncertainties are summarised in Table 6.4.

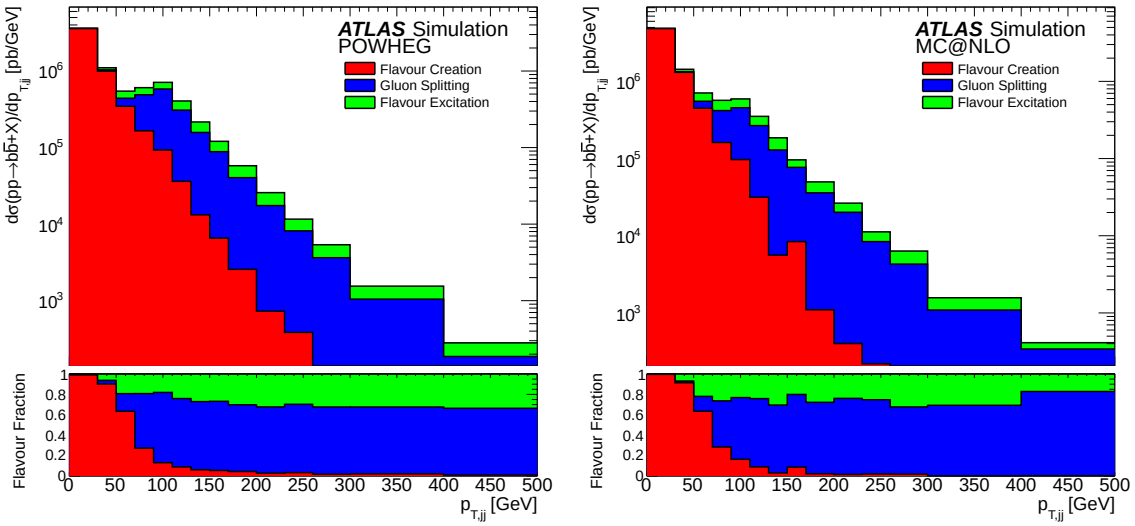

Figure 6.28.: Contribution from $b\bar{b}$ event topologies to the $p_{\mathrm{T,jj}}$ distribution.

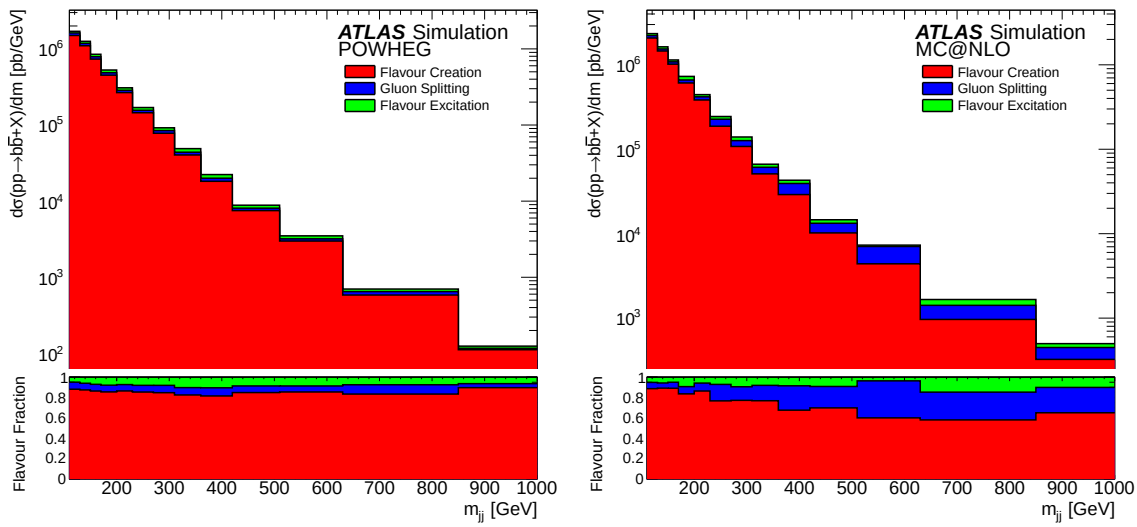

Figure 6.29.: Contribution from $b\bar{b}$ event topologies to the $\mathrm{m_{jj}}$ distribution.

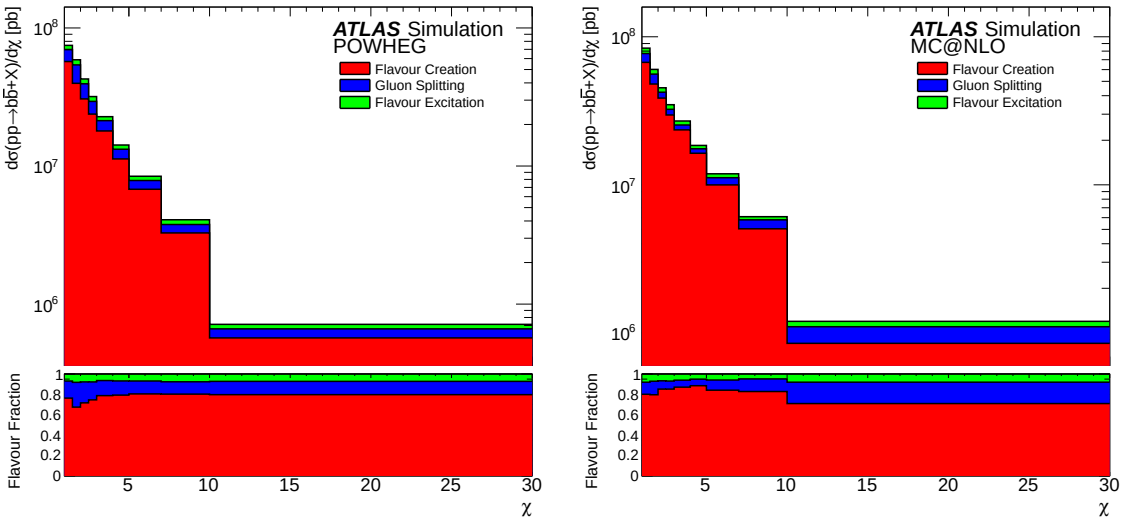

Figure 6.30.: Contribution from $b\bar{b}$ event topologies to the χ distribution.

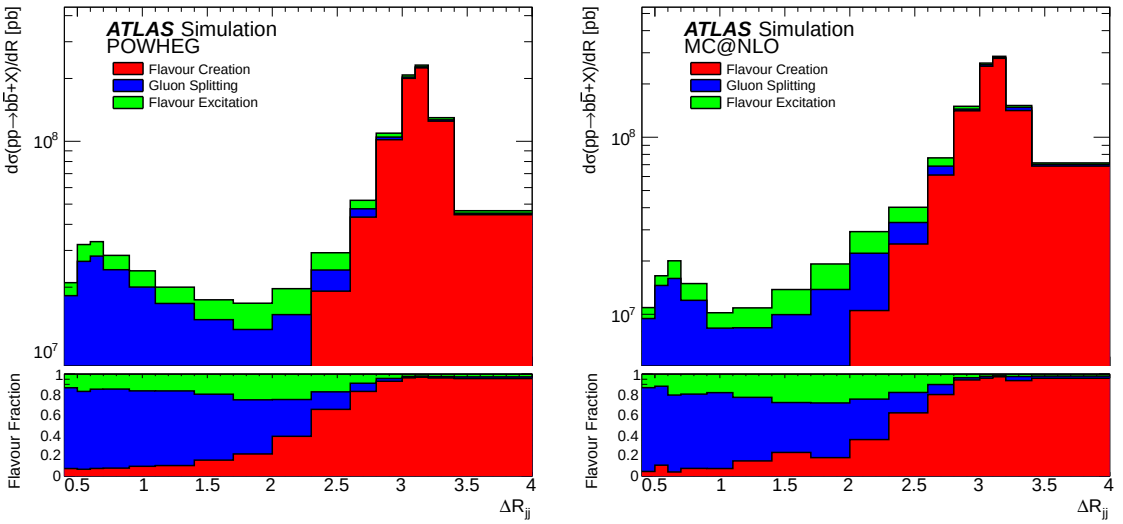

Figure 6.31.: Contribution from $b\bar{b}$ event topologies to the ΔR_{jj} distribution.

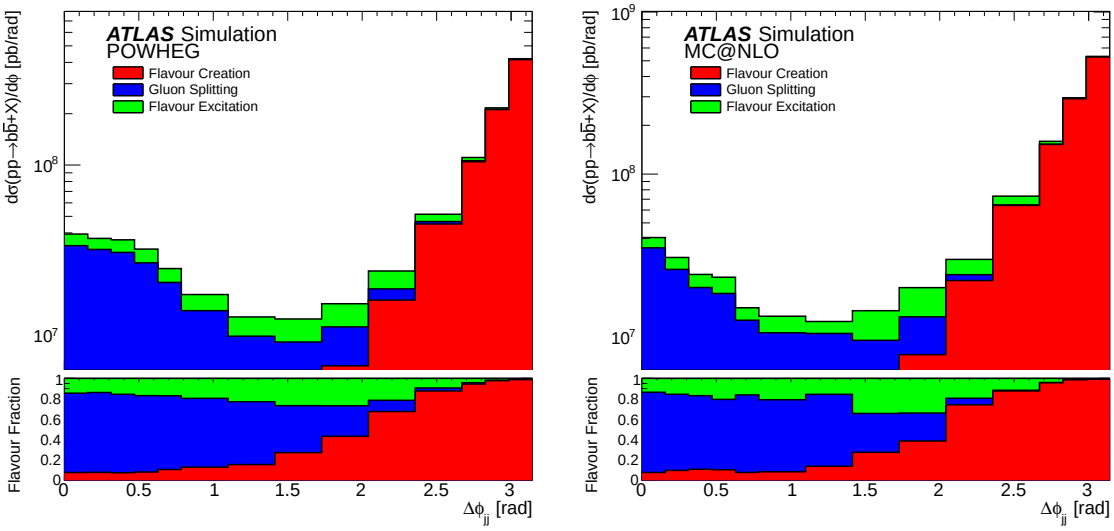

Figure 6.32.: Contribution from $b\bar{b}$ event topologies to the $\Delta\phi_{\mathrm{jj}}$ distribution.

Source of syst. uncertainty	Uncertainty [%]
Jet Energy Scale/Resolution	5 – 10
Flavour-tagging	15 – 60
Luminosity	1.8
Unfolding	2 – 10
Other sources	2 – 5

Table 6.4.: Summary of the most important systematic uncertainties.

6.6.1. Trigger Selection

The trigger efficiency for the distributions measured in this analysis is estimated directly from data, using a sample obtained with a lower threshold jet trigger. Differences between inclusive jets, b-labelled jets and b-tagged jets have been studied in Monte Carlo simulation. As no large differences were seen and trigger efficiencies were calculated from data, no systematic error is assigned for the trigger efficiency.

6.6.2. b-jet Identification

Differences in the simulation of the particle decay and detector performance can lead to differences in the predicted b-tagging efficiency. As described in Sect. 4.2.4, the measured b-tagging efficiency in data is compared to simulation and a scale factor is derived to correct the simulation. The b-jet identification systematic represents the uncertainty on the scale factors and thus the uncertainty on the performance of the b- tagging algorithms.

The scale factors for the tagging efficiency of b-, c- and light-flavour jets are varied up and down by one standard deviation. Simultaneously, the inefficiency scale factor is varied in the opposite direction. For example, to full assess the effect of increasing the b-tagging efficiency of b-labelled jet, the weight of untagged b-labelled jets are shifted down within the inefficiency uncertainty. For each variation, the b-tagging efficiency is recalculated and the template fits are repeated to reevaluate the purity. The difference in the final cross-sections are added in quadrature and taken as the flavour systematic uncertainty.

Uncertainties with the flavour tagging provide the dominant systematic uncertainty in this analysis. The angular distributions are dominated by low p_{T} jets, and are well constrained by data driven efficiency calculations. However, in the high $p_{\mathrm{T,jj}}$ and mass bins are dominated by higher p_{T} jets which have a much larger uncertainty. The 60% quoted uncertainties applies only to a few bins dominated by high p_{T} b-jets.

6.6.3. Template Fits

The templates used in this analysis are based upon the output of a track based b-tagger. Differences between the input tracks in data and MC could lead to differences in the shape of the templates. While the overall agreement between data and MC is good, some variance is seen in the track multiplicity. To assess the effect of the disagreement between data and MC, the simulation is re-weighted to match the data and the template fits are repeated. The difference in the output of the purity fit is found to be of the order of 1%, a value much smaller then other systematic uncertainties.

6.6.4. Jet Energy Scale and Resolution

As stated previously, the understanding of the accuracy to which jets are measured in the ATLAS detector represents one of the larger systematic uncertainties in an analysis involving jets. The uncertainty is split into the jet energy scale, jet energy resolution and the jet angular resolution. Since the 2010 b-jet analysis, the understanding of the jet energy scale in ATLAS has improved and is separated into its various sources which are quantified as nuisance parameters [49, 81]. Each nuisance parameter represents an uncorrelated systematic uncertainty that affects the JES. In this analysis, 16 nuisance parameters where investigated, including the uncertainty for jets which a small angular separation, pile-up and the additional uncertainties when working with b-jets. For each nuisance parameter, the jet energy was scaled up and down according to the associated uncertainty.

The jet energy resolution uncertainty is evaluated by smearing the jet energy in the simulation an additional amount so that it is the same in both data and MC. Studies were done using MC with different detector material descriptions and fragmentation functions to find the angular resolution in these different conditions. To be conservative, the jet angular resolution in the nominal MC sample was smeared to match the worst resolution in the investigated samples and the purity fits were redone. The uncertainty was taken as the differences on the measured cross-section.

6.6.5. Luminosity

The luminosity uncertainty for data recorded in 2011 is 1.8% [82]. This uncertainty is applied uniformly across all measurements.

6.6.6. Unfolding Shape Dependence

An underlying assumption of the unfolding process is that the differences between nature and the computer simulation have a small effect on the unfolding process. However, it is important to test these assumptions. To test the effect of shape differences between data and MC distributions, the MC is re-weighted to data and the unfolding is done again.

The re-weighting is done with a smooth function. The function is found by comparing the raw data to the detector level simulation, for this analysis the data after the purity fits was compared to MC events with two b-tagged and b-labeled jets. This function needs to significantly improve the data/MC agreement, but does not need to be a perfect fit. An example of the reweighing can be seen in Fig. 6.33. The other fits can be seen in Appendix D.

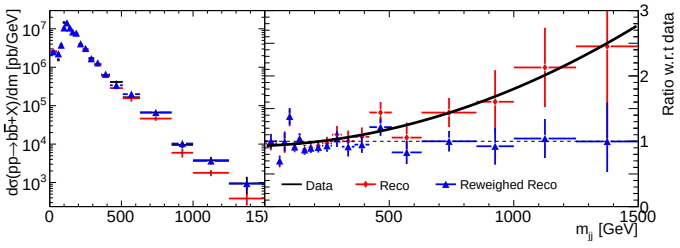

Figure 6.33.: MC re-weighting to data using a smooth functional form.

The analysis is re-run to reweight the simulation according to the smooth function just found. Using reweighted MC the unfolding factors efficiency corrections are recalculated. As mentioned earlier, the nominal MC already has a jet p_{T} reweighting applied to it, the systematic is taken as the envelope on the unfolding factors derived for the unweighted Pythia prediction and the jet p_{T} plus the variable specific reweighting. The dijet mass spectrum can be seen in Fig. 6.34, the other distributions can be seen in Appendix D .

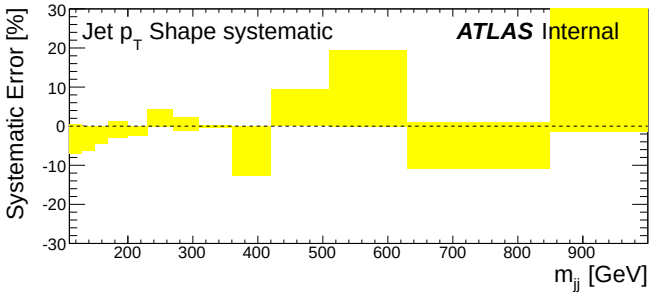

Figure 6.34.: Shape systematic for the unfolding of the dijet mass distribution

6.7. Results

The dijet p_{T} distribution is shown in Fig. 6.35. Here the black points show the results of the measurement and the yellow bands show the combined statistical and systematic uncertainty. The POWHEG prediction, in green, contains both the associated statistical uncertainty and the theoretical uncertainty. MC@NLO, in red, only includes the statistical uncertainty. As Pythia 6, in grey, is a LO MC generator it is not expected to have the correct normalisation, thus for a shape comparison it has been scaled down by 0.61. The middle panel shows the ratio of the theory predictions with data. From about 80 GeV a clear difference between the data and MC starts to develop. In the bottom panel, the ratio of FCR-like events to all events is shown.

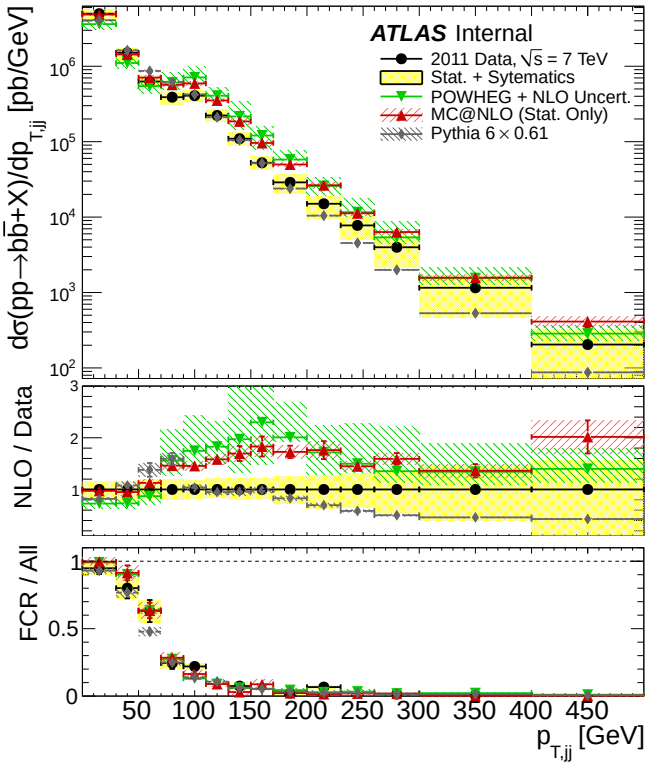

Figure 6.35.: Top Panel: The $p_{\mathrm{T,jj}}$ distribution as measured with the ATLAS detector compared to NLO distributions. Middle Panel: Ratio between NLO predictions and data. Bottom Panel: Ratio of FCR-like events to all events.

Figures 6.36 and 6.37 show the angular separation measured with respect to $\Delta\phi$ and ΔR. In these two plots both POWHEG and MC@NLO provide a good description of di-b-jets with a large angular separation. However, as the jets move closer together this agreement breaks down. In the region $1.5 < \Delta R < 3$, MC@NLO predicts too many events, while for $\Delta R < 1.5$ the agreement is better. For POWHEG the regions of agreement are reversed, i.e. better agreement for $1.5 < \Delta R < 3$ and poor agreement for $\Delta R < 1.5$. The level of agreement is similar in the $\Delta\phi$ distribution, except the disagreement in the region $1.5 < \Delta\phi < 3$ is less pronounced. In the description of ΔR, Pythia 6 predicts a very similar distribution to MC@NLO but provides a poor description of the $\Delta\phi$ distribution.

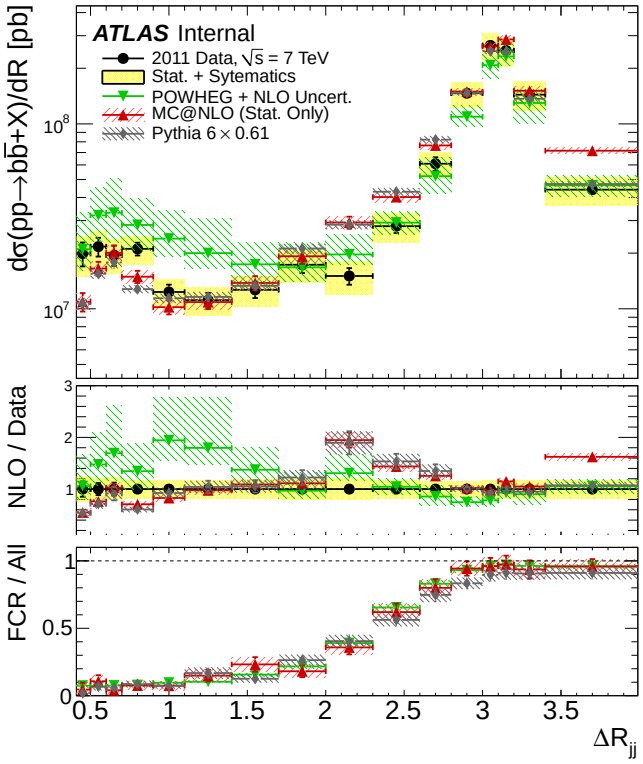

Figure 6.36.: Top Panel: The ΔR distribution as measured with the ATLAS detector compared to NLO distributions. Middle Panel: Ratio between NLO predictions and data. Bottom Panel: Ratio of FCR-like events to all events.

Figure 6.38 shows the dijet mass distribution. The bottom panel shows that the fraction of events that have a FCR-like event topology is high across the entire distribution. This implies a LO generator, like Pythia 6, should give a good description. The level of agreement between the data and Pythia 6 is good, and is at a similar level to the quality of the description given by POWHEG. MC@NLO tends to predict more events than POWHEG and gives a higher prediction than data in the high dijet mass bins. In many of the distributions shown, MC@NLO and

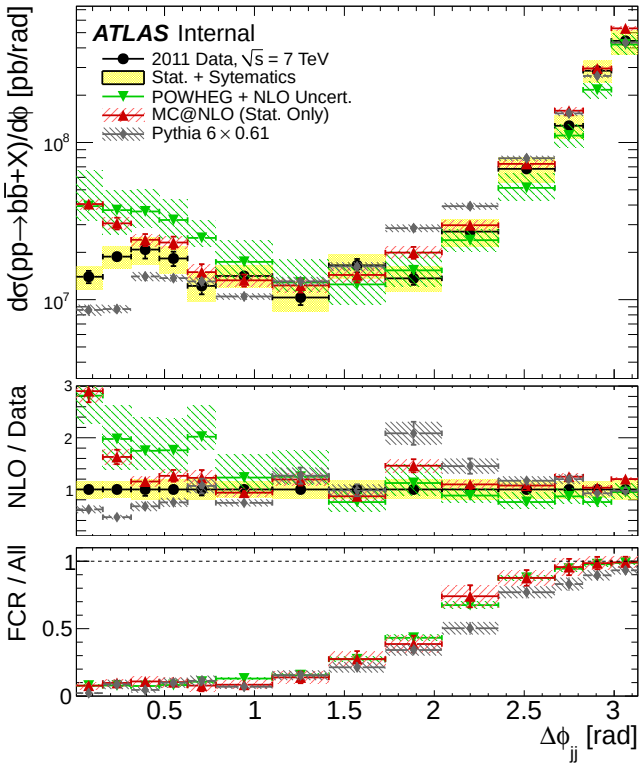

Figure 6.37.: Top Panel: The ϕ distribution as measured with the ATLAS detector compared to NLO distributions. Middle Panel: Ratio between NLO predictions and data. Bottom Panel: Ratio of FCR-like events to all events.

POWHEG bracket the data. For the higher dijet mass bins, as with the high dijet p_{T} bins, the systematic uncertainty dramatically increases. This is to due the poorly constrained uncertainty on the b-jet tagging for high p_{T} jets, which dominate the entries in these bins.

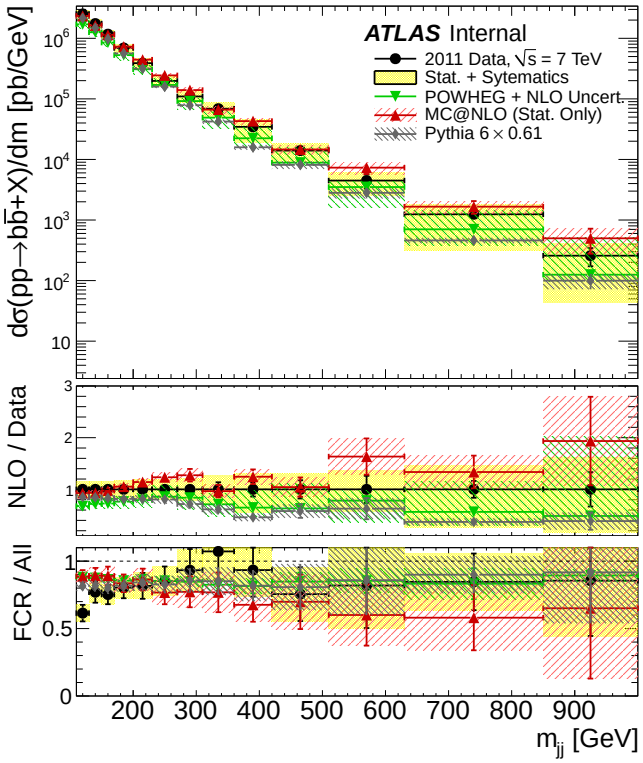

Figure 6.38.: Top Panel: The m_{jj} distribution as measured with the ATLAS detector compared to NLO distributions. Middle Panel: Ratio between NLO predictions and data. Bottom Panel: Ratio of FCR-like events to all events.

Figures 6.39 and 6.40 show the χ and y_B distributions. The χ distribution shows the largest disagreement between MC@NLO and data. The data/POWHEG agreement is best in the χ distribution. In the y_B distribution, POWHEG generally predicts fewer events and for low values of y_B there appears to be some shape difference. MC@NLO provides a much better description as a whole for the y_B distribution.

When examining all the data and MC comparisons shown in this section, a clear disagreement can be seen between theory and measurement. In order to have confidence in the final result, it is important to understand where this disagreement comes from. To test if differences seen in different regions of phase space are the manifestation of a single issue or multiple, the predictions can be reweighed to correct the difference in one distribution. If the difference is from a single source then this will correct all the distributions, if there are multiple sources causing the differences

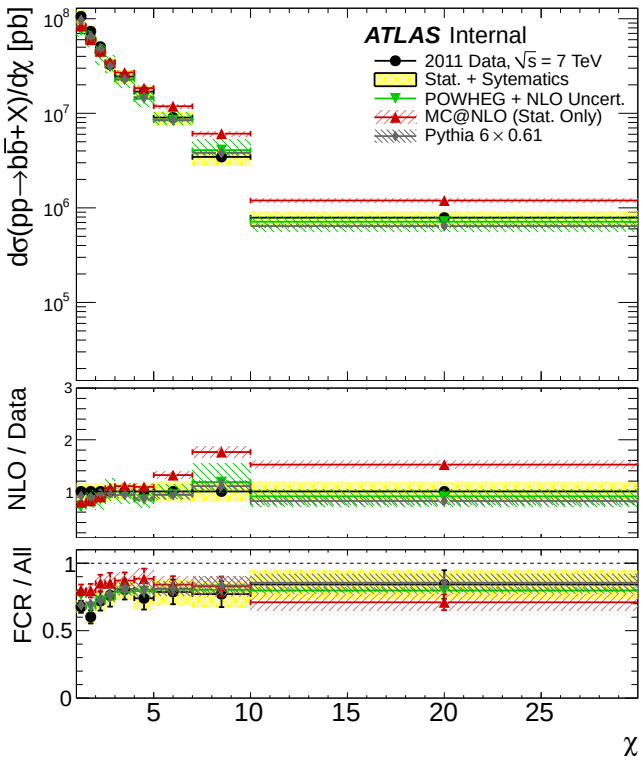

Figure 6.39.: Top Panel: The χ distribution as measured with the ATLAS detector compared to NLO distributions. Middle Panel: Ratio between NLO predictions and data. Bottom Panel: Ratio of FCR-like events to all events.

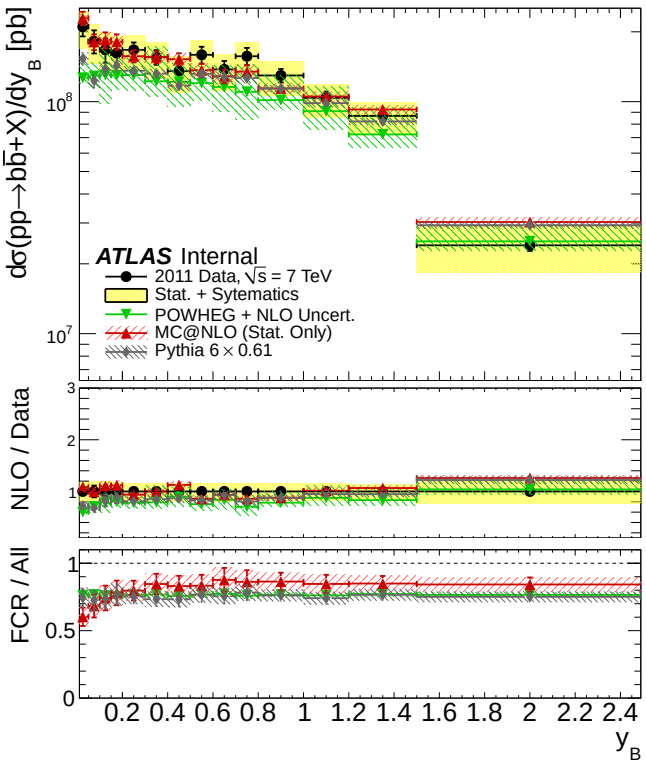

Figure 6.40.: Top Panel: The y_B distribution as measured with the ATLAS detector compared to NLO distributions. Middle Panel: Ratio between NLO predictions and data. Bottom Panel: Ratio of FCR-like events to all events.

then an improved MC description in the other distributions is not expected. The POWHEG $p_{\mathrm{T,jj}}$ distribution was reweighted by multiplying the event weight by 0.5 if $p_{\mathrm{T,jj}} > 80$ GeV. The results of the reweighting can be seen in Fig. 6.41. By modifying the POWHEG $p_{\mathrm{T,jj}}$ distribution, significant improvement in the ΔR distribution is seen. This suggests the a single source of disagreement which produced small ΔR and large $p_{\mathrm{T,jj}}$ di-b-jet pairs.

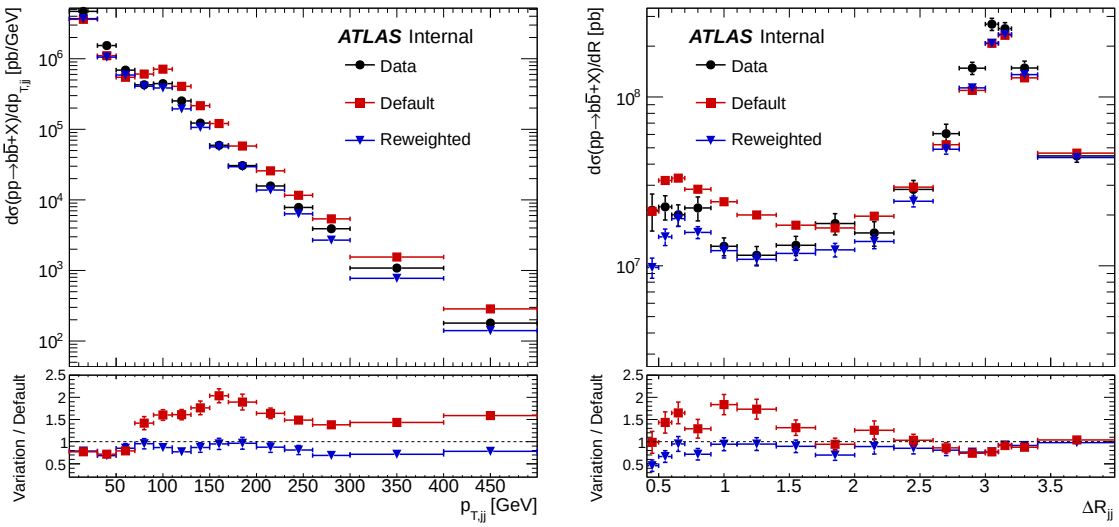

Figure 6.41.: Comparison of the unweighted and weighted POWHEG distributions to investigate source of excess in NLO predictions.

The excess of close-by b-jets with a large dijet p_{T} could be explained by the NLO generators producing too many $b\bar{b}$ events via gluon splitting. To look further into this, the events are separated into jet topologies as described in Sect. 6.5.5. Events are classified as either FCR-like or other (OTH). The $p_{\mathrm{T,jj}}$ distribution, which highlighted the differences, is split into its separate event topologies in Fig. 6.42. In plot (a) the FCR-like events are plotted, in the region where statistics are good there is good agreement between data and MC. However, for the non-FCR-like event distribution in plot (b) an excess of events can be seeing starting at 80 GeV. This supports the hypothesis that disagreement between data and NLO is from an excess of gluon-splitting like events. Similar distributions are shown in Fig. 6.43 and 6.44. The χ topology distributions suggest the excess of MC@NLO events in Fig. 6.39 come from non-FCR-like events. The mass topology distributions show an excess for MC@NLO in the non-FCR-like events as well. However, as Fig 6.29 and 6.38 indicate, this distribution is dominated by FCR-like event and so this excess does not have a large effect on the final result.

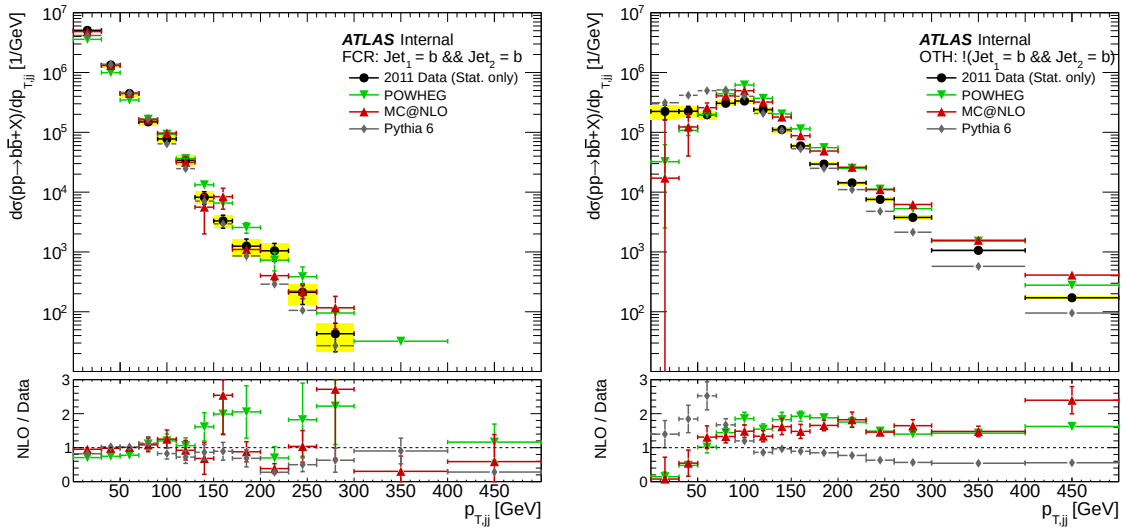

(a) (b)

Figure 6.42.: Left: $p_{\mathrm{T,jj}}$ distribution for events where the leading and sub-leading jets are b-tagged. Right: $p_{\mathrm{T,jj}}$ distribution for events not in left plot.

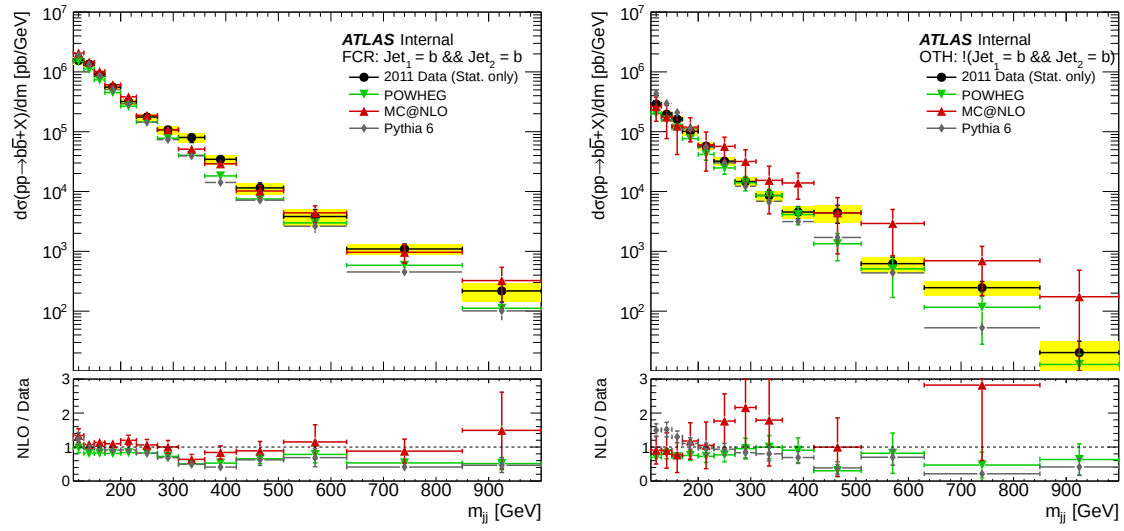

Figure 6.43.: Left: m_{jj} distribution for events where the leading and sub-leading jets are b-tagged. Right: m_{jj} distribution for events not in left plot.

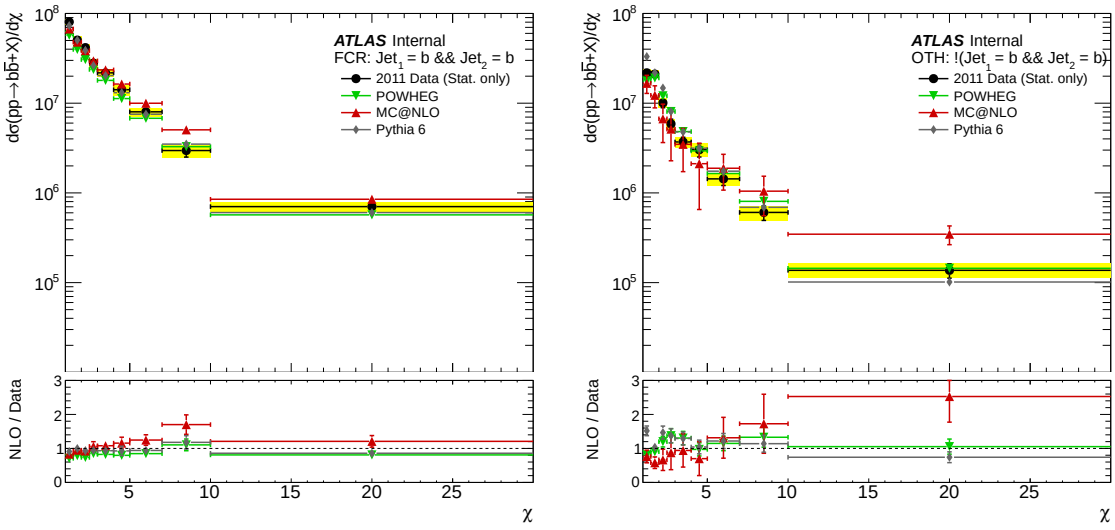

Figure 6.44.: Left: χ distribution for events where the leading and sub-leading jets are b-tagged. Right: χ distribution for events not in left plot.

6.8. Conclusions

The differential di-b-jet cross-section has been measured with respect to six variables and compared NLO predictions. In all distributions, a disagreement between data and NLO predictions is observed, which is consistent with the simulation mismodelling the relative rates of the different $b\bar{b}$ production mechanisms. The excess of b-jet pairs with a small angular separation and large dijet p_{T} suggest that these events originate from gluon splitting. For most distributions POWHEG and MC@NLO bracket the data and describe events with a back-to-back topology well. In regions where higher order terms are important, i.e. where the b-jets are not back-to-back, the NLO generators do less well. Pythia 6 provides a reasonable description of the dijet mass and ΔR spectrum, but there is room for improvement in other regions of phase space.

Chapter 7.

Conclusions

This thesis covered the measurement of the inclusive and dijet cross-sections of b-jets with the data recorded by ATLAS during 2010 and the measurement of the di-b-jet cross-sections with the 2011 dataset. The data was compared to the NLO MC generators POWHEG and MC@NLO as well as the LO generator Pythia 6.

The 2010 b-jet analysis described in chapter 5 looked at the inclusive b-jet cross-section with respect to two different b-tagging algorithms and the di-b-jet cross-section measured using the SV0 b-tagging algorithm. The primary measurement discussed was the inclusive b-jet cross-section measured with the SV0 algorithm. Measurements of the inclusive b-jet p_{T} were presented in four different rapidity regions in the region $20 < p_{\mathrm{T}} < 400\,\mathrm{GeV}$. The secondary inclusive b-jet measurement made with the p_{T}^{rel} algorithm was done with respect to a single rapidity region and up to a p_{T} of 140 GeV. The two results are consistent with each other, as shown in Fig 5.11. In Fig. 5.18 the results of the CMS inclusive cross-section measurement are compared to the ATLAS results and show good agreement. Differences between the MC@NLO and POWHEG predictions are evident in the different rapidity bins for the inclusive cross-section. The MC@NLO predictions have a rapidity dependence not seen in the data or in POWHEG.

The 2011 di-b-jet measurement discussed in chapter 6 looked at six different distributions in the dijet system. The event selection differed from the 2010 dijet measurement by selecting any event with two b-jets, rather then just events with the leading and sub-leading jets b-tagged. This produced a much more inclusive result with a greater sensitivity to higher order effects. A marked difference was seen between data and MC predictions for the $p_{\mathrm{T,jj}}$ distribution above 80 GeV and for jet pairs with small ΔR and $\Delta\phi$. Investigation into the cause of this difference showed it to be from a single source, the relative production rates of close-by b-jets. Regions of phase space which are dominated by close-by b-jets tend to be a b-jet pair recoiling against a third hard jet. This 3-jet topology means the NLO $b\bar{b}$ production is effectively LO here. There are sizeable higher order corrections expected in these regions so a LO description is not expected to predict nature well. The extent to which the higher order corrections are relevant can be seen in the differences

between the MC@NLO and POWHEG for these close-by jets. For very close-by jets, $\Delta R < 1.5$, MC@NLO provides a better description, but for $1.5 < \Delta R < 2.5$ POWHEG does better. Outside these regions, the different generators can be up to a factor of 2 out. In many areas of phase space, Pythia 6 provides a description of the $b\bar{b}$ topology at a similar level of accuracy to the NLO generators.

In general the description of the data provided by the MC generators performed poorly in areas where higher order corrections were important. In regions where the b-jets are in a back-to-back like topology the theoretical predictions perform better.

Appendix A.

Trigger Efficiencies

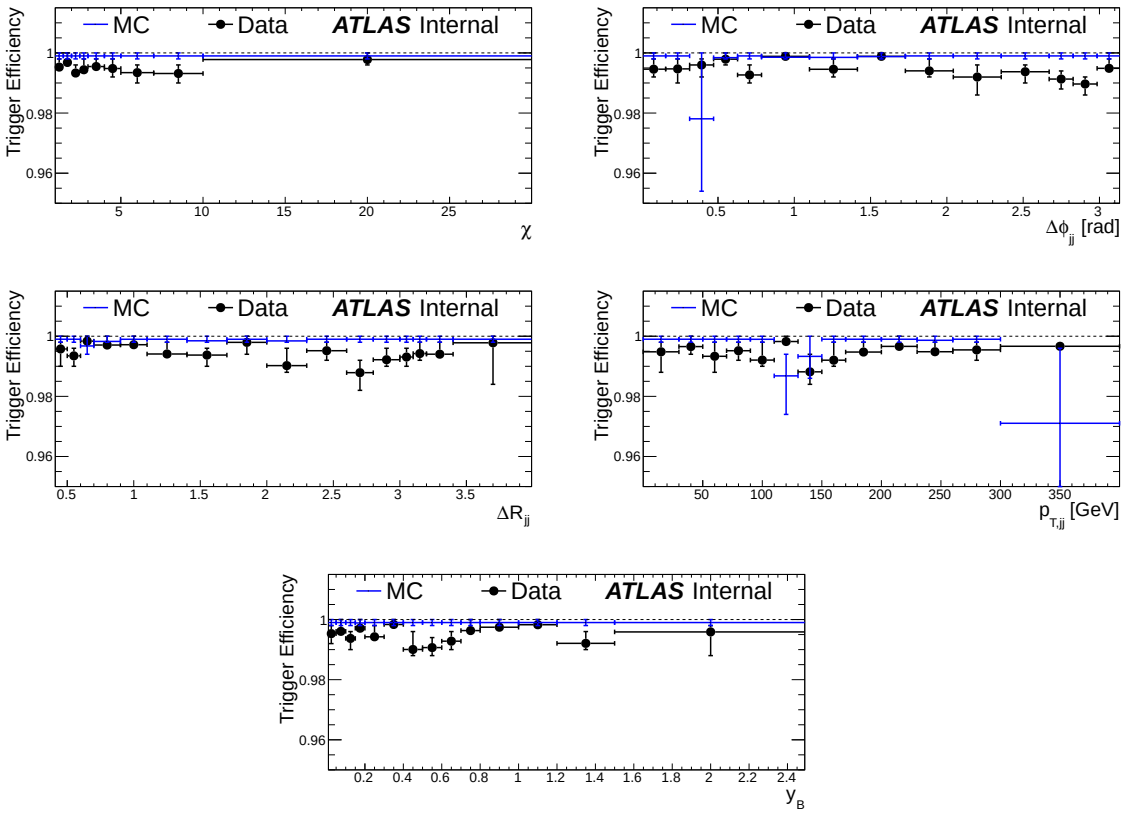

Figure A.1.: Trigger efficiencies for measured distributions.

Appendix B.

Fiducial and efficiency corrections

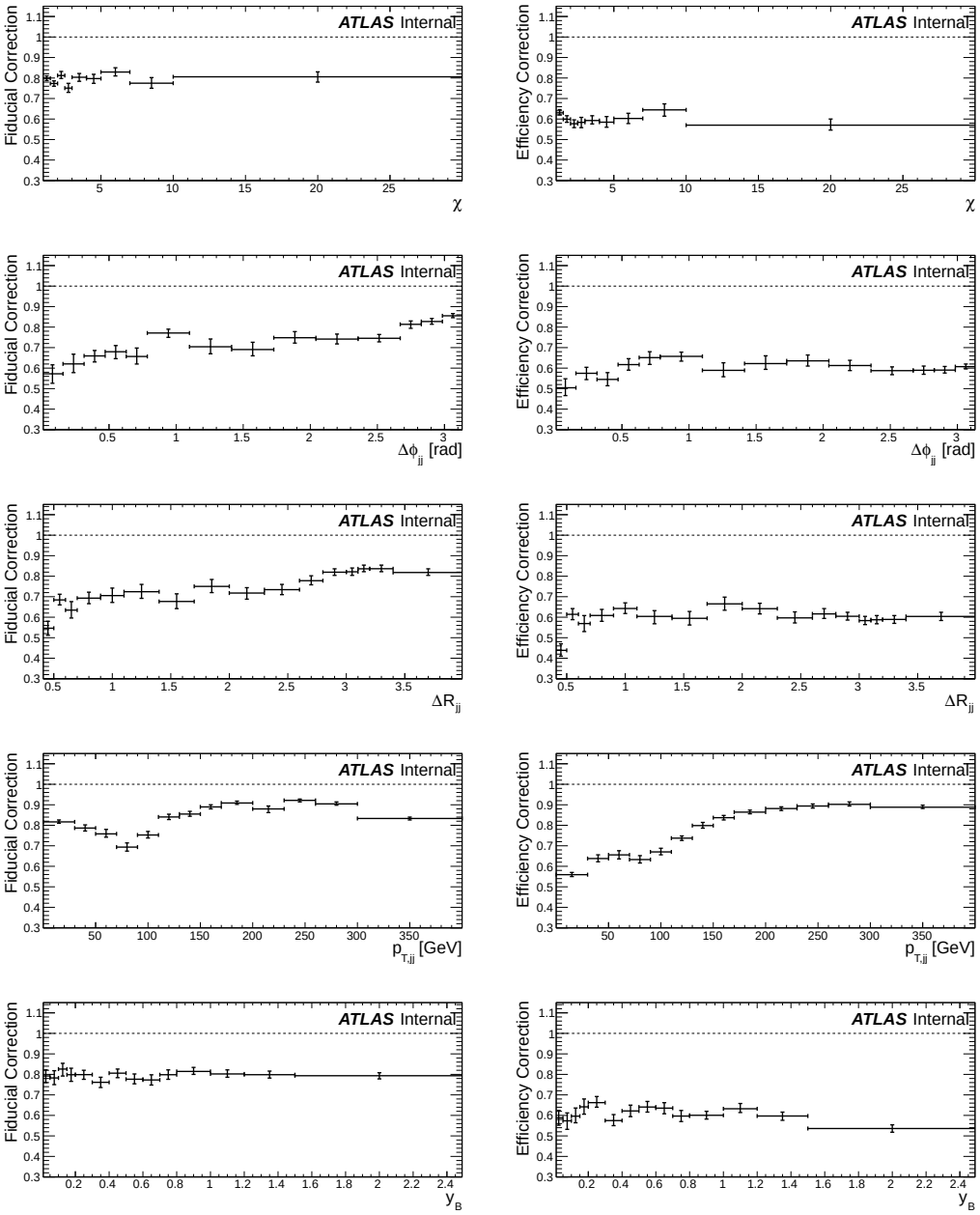

Figure B.1.: Fiducial and efficiency corrections. The shape in the $p_{\mathrm{T,jj}}$ distribution is due to matched truth jets being outside the fiducial cuts of the analysis. Events with low $p_{\mathrm{T,jj}}$ tend to be back-to-back and so each jet can have a large p_{T}. As dijet p_{T} gets larger, but before gluon splitting becomes accessible, one of the b-jets in the event needs to have radiated a third hard jet reducing its over all p_{T} and moving it closer to the fiducial boundary.

Appendix C.

Unfolding Closure Tests

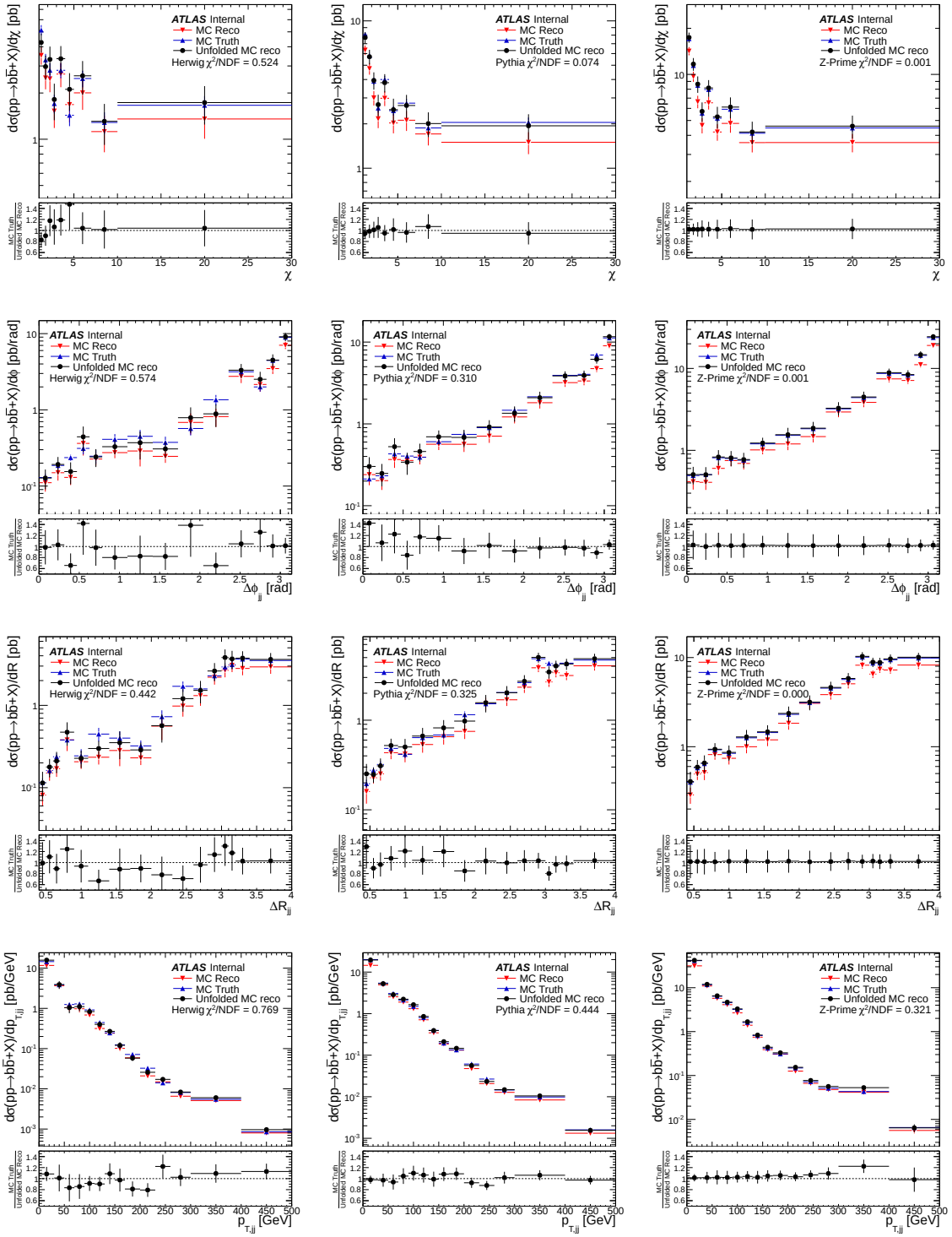

Figure C.1.: Closure test of the unfolding for different Monte Carlos.

Appendix D.

Unfolding Shape Variation Systematics

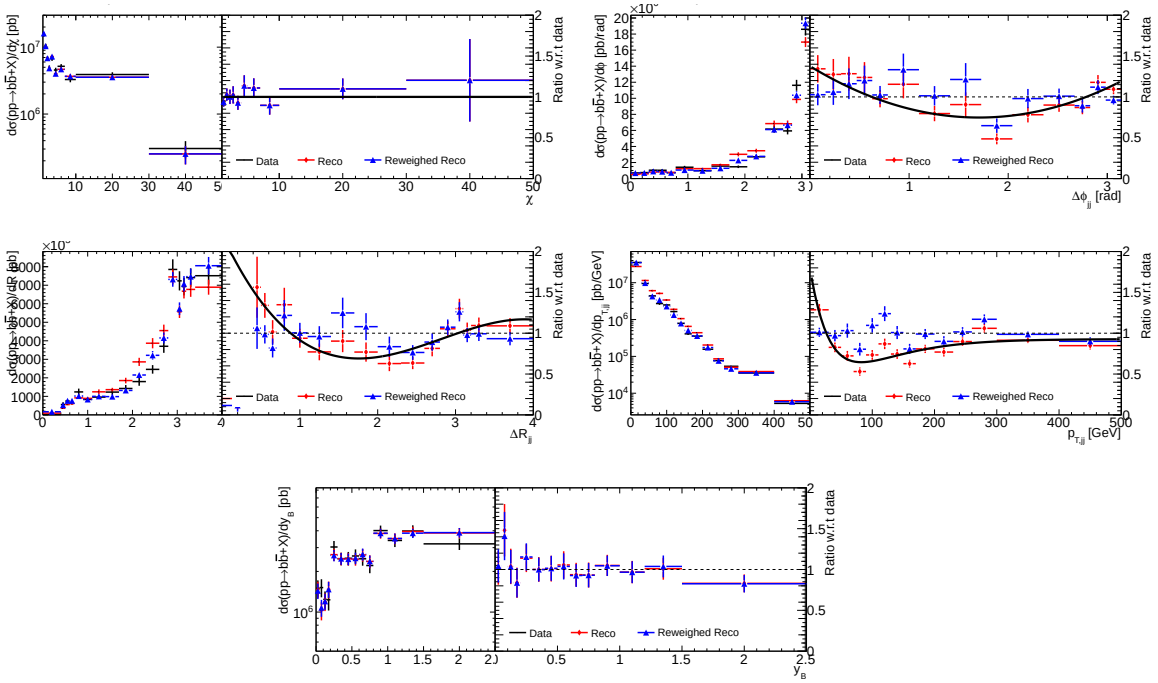

Figure D.1.: Monte Carlo re-weighting to data with smooth functional forms.

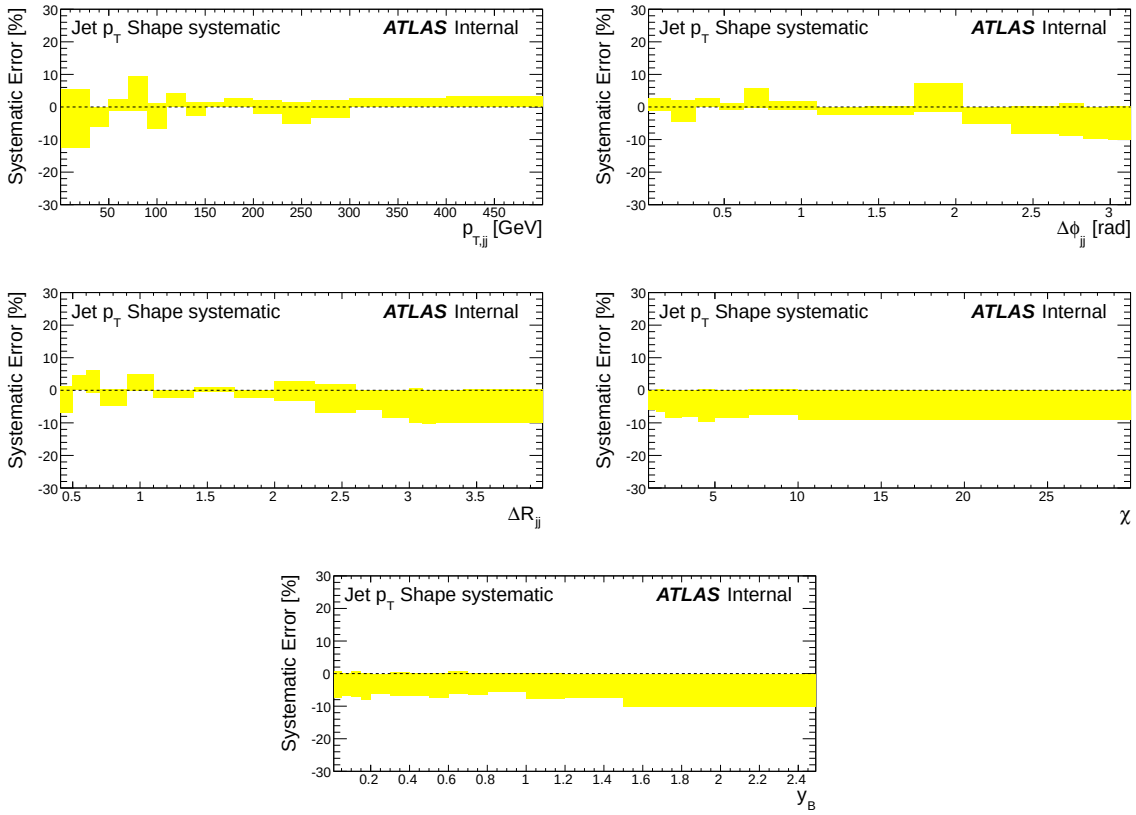

Figure D.2.: Shape systematic for the unfolding.

Bibliography

[1] N. Konstantindis, *Resonant structure and charge-flavour correlations in the $B\pi^{+/-}$ system using fully reconstructed B decays*. PhD thesis, Imperial College, UK, 1995.

[2] E. Jansen and N. De Groot, *Supersymmetry search using Z^0 bosons produced in neutralino decays at the ATLAS detector*. PhD thesis, Nijmegen U., Nijmegen, 2011. Presented 11 Apr 2011.

[3] M. Marx, *Standard Model and Exotic Diboson Production with the ATLAS Detector*. PhD thesis, Manchester U., 2013. Presented 09 May 2013.

[4] S. Baker, *Studies of Jets, Subjets and Higgs Searches with the ATLAS Detector*. PhD thesis, University College London, UK.

[5] E. P. Walters, *Death and conceptions of the afterlife in early modern England*. PhD thesis, Cambridge, UK.

[6] B. Xinyue, *The Divinity of Augustus in Augustan Poetry*. PhD thesis, University College London, UK.

[7] Daniel Lattimer, *Tekken brought lateral movement to the 'beat 'um up genre'*, tech. rep., Portsmouth University, UK, 2009.

[8] The ATLAS Collaboration, *Measurement of the inclusive and dijet cross-sections of b-jets in pp collisions at $\sqrt{s}$ = 7 TeV with the ATLAS detector*, Eur. Phys. J. **C71** (2011) 1846, `arXiv:1109.6833 [hep-ex]`.

[9] The UA1 Collaboration, *Beauty production at the CERN proton-antiproton collider*, Phys. Lett. **B186** (1987) 237–246.

[10] The UA1 Collaboration, *Measurement of the bottom quark production cross-section in proton-antiproton collisions at $\sqrt{s}$ = 0.63 TeV*, Phys. Lett. **B213** (1988) 405.

[11] The CDF Collaboration, *Measurement of the bottom quark production cross-section using semileptonic decay electrons in $p\overline{p}$ collisions at $\sqrt{s}$ = 1.8 TeV*, Phys. Rev. Lett. **71** (1993) 500–504.

[12] The CDF Collaboration, *Measurement of bottom quark production in 1.8 TeV $p\overline{p}$ collisions using semileptonic decay muons*, Phys. Rev. Lett. **71** (1993)

2396–2400.

[13] The DØ Collaboration, *The $b\bar{b}$ production cross-section and angular correlations in $p\overline{p}$ collisions at $\sqrt{s}$ = 1.8 TeV*, Phys. Lett. **B487** (2000) 264–272, arXiv:hep-ex/9905024.

[14] The DØ Collaboration, *Cross-section for b jet production in $\overline{p}p$ collisions at $\sqrt{s}$ = 1.8 TeV*, Phys. Rev. Lett. **85** (2000) 5068–5073, arXiv:hep-ex/0008021.

[15] The LHC*b* Collaboration, *Measurement of $\sigma(pp \to b\bar{b}X)$ at $\sqrt{s}$ = 7 TeV in the forward region*, Phys. Lett. **B694** (2010) 209–216, arXiv:1009.2731 [hep-ex].

[16] The CMS Collaboration, *Measurement of $B\overline{B}$ angular correlations based on secondary vertex reconstruction at $\sqrt{s}$ = 7 TeV*, JHEP **03** (2011) 136, arXiv:1102.3194 [hep-ex].

[17] The CMS Collaboration, *Inclusive b-hadron production cross section with muons in pp collisions at $\sqrt{s}$ = 7 TeV*, JHEP **03** (2011) 090, arXiv:1101.3512 [hep-ex].

[18] D. Griffiths, *Introduction to elementary particles.* John Wiley and Sons, inc, 1987.

[19] R.K. Ellis, W.J. Stirling and B.R. Webber, *QCD and Collider Physics.* Cambridge Press, 1996.

[20] J.C. Collins, D.E. Soper and G. Sterman, *Perturbative Quantum Chromodynamics.* World Scientific, 1989.

[21] S. Catani et al, *QCD*, arXiv:arXiv:hep-ph/0005025v1 [hep-ph].

[22] H.-L. Lai, M. Guzzi, J. Huston, Z. Li, P. M. Nadolsky, et al., *New parton distributions for collider physics*, Phys.Rev. **D82** (2010) 074024, arXiv:1007.2241 [hep-ph].

[23] The Durham HEP Data project Collaboration, *Online PDF plotting and calculation*, http://hepdata.cedar.ac.uk/pdf/pdf3.html.

[24] A. D. Martin, W. J. Stirling, R. S. Thorne, and G. Watt, *Parton Distributions for the LHC*, Eur. Phys. J. **C63** (2009) 189–285, arXiv:0901.0002 [hep-ph].

[25] D. Stump, J. Huston, et al., *Inclusive Jet Production, Parton Distributions, and the Search for New Physics*, JHEP 0310 (2003) 046 , arXiv:0303013v1 [hep-ph].

[26] S. Forte, L. Garrido, et al., *Neural Network Parametrization of Deep-Inelastic Structure Functions*, JHEP 0205:062 (2002) , arXiv:0204232v3 [hep-ph].

[27] V.N. Gribov and L.N. Lipatov, Sov. J. Nucl. Phys. **15** (1972) 438.

[28] V.N. Gribov and L.N. Lipatov, Sov. J. Nucl. Phys. **15** (1972) 675.

[29] G. Altarelli and G. Parisi, Nucl. Phys. **B126** (1977) 298.

[30] Yu. L. Dokshitzer, Sov. Phys. **JETP 46** (1977) 641.

[31] J.M. Campbell, J.W. Huston and W.J. Stirling, *Hard interactions of quarks and gluons: a primer for LHC physics*, Rep. Prog. Phys. 70 (2007) 89−193 (2007) .

[32] The ALICE Collaboration, *The ALICE experiment at the CERN LHC*, JINST 3 S08002 (2008) .

[33] The LHC*b* Collaboration, *The LHCb experiment at the CERN LHC*, JINST 3 S08005 (2008) .

[34] The ATLAS Collaboration, *The ATLAS Experiment at the CERN Large Hadron Collider*, JINST 3 S08003 (2008) .

[35] The CMS Collaboration, *The CMS experiment at the CERN LHC*, JINST 3 S08004 (2008) .

[36] The ATLAS Collaboration, *Commissioning of the ATLAS high-performance b-tagging algorithms in the 7 TeV collision data*, ATLAS-CONF-2011-102 (2011) .

[37] M. Aharrouche et al., *Responce uniformity of the ATLAS liquid argon electromagnetic calorimeter*, Nucl. Instrum. Meth. A 582 (2007) 429 .

[38] J. Colas et al., *Position resolution and particle identification with the ATLAS EM calorimeter*, Nucl. Instrum. Meth. A 550 (2005) 96 .

[39] M. Aharrouche et al., *Energy linearity and resolution of the ATLAS electromagnetic barrel calorimeter in an electron test-beam*, Nucl. Instrum. Meth. A 568 (2006) 601 .

[40] B. Dowler et al., *Performance of the ATLAS hadronic end-cap calorimeter in beam tests*, Nucl. Instrum. Meth. A 482 (2002) 94 .

[41] M. Hurwitz et al., *Module-to-Module uniformity at 180 GeV in 2002-2003 tile calorimeter calibration test-beams*, ATLAS Note ATL-PUB-TILE-2006-008 .

[42] S. Akhmadaliev et al., *Results from a new combined test of an electromagnetic liquid argon calorimeter with a hadronic scintillation-tile calorimeter*, Nucl. Instrum. Meth. A 449 (2000) 461 .

[43] The ATLAS Collaboration, *Performance of the ATLAS Jet Trigger in the Early* $\sqrt{s}$ *= 7 TeV Data*, ATLAS-CONF-2010-094, 2010.

[44] M. Cacciari, G. P. Salam, and G. Soyez, *The anti-k_t jet clustering algorithm*, JHEP **04** (2008) 063, arXiv:0802.1189 [hep-ph].

[45] Y. L. Dokshitzer et al., *Better Jet Clustering Algorithms*, JHEP **08** (1997) 001, arXiv:hep-ph/9707323 [hep-ph].

[46] The ATLAS Collaboration, *Jet energy measurement with the ATLAS detector in proton-proton collisions at $\sqrt{s}$ =7 TeV*, Eur. Phys. J. **C73** (2013) 2304.

[47] The ATLAS Collaboration, *Jet energy resolution in proton-proton collisions at $\sqrt{s}$=7 TeV recorded in 2010 with the ATLAS detector*, Eur. Phys. J. **C73** (2013) 2306.

[48] The ATLAS Collaboration, *Jet energy resolution and selection efficiency relative to track jets from in-situ techniques with the ATLAS Detector Using Proton-Proton Collisions at a Center of Mass Energy $\sqrt{s}$ = 7 TeV*, ATLAS-CONF-2010-054, 2010.

[49] The ATLAS Collaboration, *Jet energy scale and its systematic uncertainty in proton-proton collisions at sqrt(s)=7 TeV with ATLAS 2011 data*, ATLAS-CONF-2013-004, 2011.

[50] The ATLAS Collaboration, *Performance of the ATLAS Secondary Vertex b-tagging Algorithm in 7 TeV Collision Data*, ATLAS-CONF-2010-042 (2010) .

[51] G. Piacquadio, C. Weiser, *A new inclusive secondary vertex algorithm for b-jet tagging in ATLAS*, J. Phys.: Conf. Ser. 119 032032 (2008) .

[52] The ATLAS Collaboration, *Calibrating the b-Tag Efficiency and Mistag Rate in 35 pb^{-1} of Data with the ATLAS Detector*, Tech. Rep. ATLAS-CONF-2011-089, CERN, Geneva, Dec, 2011.

[53] The ATLAS Collaboration, *Measurement of the b-tag Efficiency in a Sample of Jets Containing Muons with 5 fb^{-1} of Data from the ATLAS Detector*, ATLAS-CONF-2012-043, 2012.

[54] B. Andersson, G. Gustafson, G. Ingelman, and T. Sjostrand, *Parton fragmentation and string dynamics*, Phys. Rept. **97** (1983) 31–145.

[55] P. Nason, *A new method for combining NLO QCD with shower Monte Carlo algorithms*, JHEP **11** (2004) 040, arXiv:hep-ph/0409146.

[56] S. Alioli, P. Nason, C. Oleari, and E. Re, *A general framework for implementing NLO calculations in shower Monte Carlo programs: the POWHEG BOX*, JHEP **06** (2010) 043, arXiv:1002.2581 [hep-ph].

[57] S. Frixione, P. Nason, and C. Oleari, *Matching NLO QCD computations with parton shower simulations: the POWHEG method*, JHEP **11** (2007) 070, arXiv:0709.2092 [hep-ph].

[58] S. Frixione, P. Nason, and G. Ridolfi, *A Positive-Weight Next-to-Leading-Order Monte Carlo for Heavy Flavour Hadroproduction*, JHEP **09** (2007) 126, arXiv:0707.3088 [hep-ph].

[59] S. Frixione and B. R. Webber, *Matching NLO QCD computations and parton shower simulations*, JHEP **06** (2002) 029, arXiv:hep-ph/0204244.

[60] S. Frixione, P. Nason, and B. R. Webber, *Matching NLO QCD and parton showers in heavy flavour production*, JHEP **08** (2003) 007, arXiv:hep-ph/0305252.

[61] The ATLAS Collaboration, *Luminosity determination in pp collisions at* $\sqrt{s}$ *= 7 TeV Using the ATLAS Detector at the LHC*, Eur. Phys. J. **C71** (2011) 1630, arXiv:1101.2185 [hep-ex].

[62] The ATLAS Collaboration, *Updated luminosity determination in pp collisions at* $\sqrt{s} = 7$ *TeV using the ATLAS detector*, ATLAS-CONF-2011-011, Mar, 2011.

[63] The ATLAS Collaboration, *Charged-particle multiplicities in pp interactions at* $\sqrt{s}$ *= 900 GeV measured with the ATLAS detector at the LHC*, Phys. Lett. **B688** (2010) 21–42, arXiv:1003.3124.

[64] The ATLAS Collaboration, *Data-Quality Requirements and Event Cleaning for Jets and Missing Transverse Energy Reconstruction with the ATLAS Detector in Proton-Proton Collisions at a Center-of-Mass Energy of* $\sqrt{s} = 7$ *TeV*, Tech. Rep. ATLAS-COM-CONF-2010-038, CERN, Geneva, May, 2010.

[65] T. Sjostrand, S. Mrenna, and P. Skands, *PYTHIA 6.4 physics and manual*, JHEP **05** (2006) 026, hep-ph/0603175.

[66] A. Sherstnev and R. S. Thorne, *Different PDF approximations useful for LO Monte Carlo generators*, arXiv:0807.2132 [hep-ph].

[67] The ATLAS Collaboration, *Charged particle multiplicities in pp interactions at* $\sqrt{s}$ *= 0.9 and 7 TeV in a diffractive limited phase space measured with the ATLAS detector at the LHC and a new pythia 6 tune*, ATLAS-CONF-2010-031, 2010.

[68] The ATLAS Collaboration, G. Aad et al., *The ATLAS Simulation Infrastructure*, arXiv:1005.4568 [hep-ex].

[69] S. Agostinelli et al., *G4–a simulation toolkit*, Nuclear Instruments and Methods in Physics Research Section A: Accelerators, Spectrometers, Detectors and Associated Equipment **506** (2003) no. 3, 250 – 303.

[70] The CMS Collaboration, *Inclusive b-jet production in pp collisions at* $\sqrt{s}$*=7 TeV*, JHEP **04** (2012) 084.

[71] S. Leone et al., *The Good, the Bad and the Ugly*, Produzioni Europee Associati

(1966) .

[72] The ATLAS Collaboration, *ATLAS tunes of PYTHIA6 and Pythia8 for MC11*, ATL-PHYS-PUB-2011-009 (2011) .

[73] A. Sherstnev and R. S. Thorne, *Parton distributions for LO generators*, Eur. Phys. J. **C55** (2008) 553–575, arXiv:0711.2473 [hep-ph].

[74] A. Sherstnev and R. Thorne, *Different PDF approximations useful for LO Monte Carlo generators*, arXiv:0807.2132 [hep-ph].

[75] H.-L. Lai, J. Huston, S. Mrenna, P. Nadolsky, D. Stump, W.-K. Tung, and C.-P. Yuan, *Parton distributions for event generators*, JHEP **04** (2010) 035, arXiv:0910.4183 [hep-ph].

[76] Corcella, G. and others, *HERWIG 6.5: an event generator for hadron emission reactions with interfering gluons (including supersymmetric processes)*, JHEP **01** (2001) 010, arXiv:hep-ph/0011363.

[77] The ATLAS Collaboration, *New ATLAS event generator tunes to 2010 data*, ATL-PHYS-PUB-2011-008, 2011. ATL-PHYS-PUB-2011-009 (2011) .

[78] B. Malaescu, *An Iterative, dynamically stabilized method of data unfolding*, arXiv:0907.3791 [physics.data-an].

[79] D. Casadei, *Estimating the selection efficiency*, July, 2012. arXiv:0908.0130 [physics.data-an].

[80] J. Alwall, A. Ballestrero, P. Bartalini, S. Belov, E. Boos, et al., *A Standard format for Les Houches event files*, Comput.Phys.Commun. **176** (2007) 300–304, arXiv:hep-ph/0609017 [hep-ph].

[81] The ATLAS Collaboration, *Jet energy measurement and systematic uncertainties using tracks for jets and for b-quark jets produced in proton-proton collisions at* $\sqrt{s} = 7$ *TeV in the ATLAS detector*, ATLAS-CONF-2013-002, Jan, 2013.

[82] ATLAS Collaboration, *Improved luminosity determination in pp collisions at* $\sqrt{s} = 7$ *TeV using the ATLAS detector at the LHC*, arXiv:1302.4393 [hep-ex].